Stony Brook University

A Light-Sharing Approach to High-Resolution 3D Gamma-Ray Detection for Positron Emission Tomography

A Dissertation Presented

by

Srilalan Krishnamoorthy

to

The Graduate School

in Partial Fulfillment of the

Requirements

for the degree of

Doctor of Philosophy

in

Biomedical Engineering

(Medical Physics)

Stony Brook University

May 2011

Stony Brook University

The Graduate School

Srilalan Krishnamoorthy

We, the dissertation committee for the above candidate for the
Doctor of Philosophy degree, hereby recommend
acceptance of this dissertation.

Paul Vaska, Ph.D. – Dissertation Advisor
Scientist, Brookhaven National Laboratory
Adjunct Professor, Biomedical Engineering, Stony Brook University

Terry Button, Ph.D. – Chairperson of Defense
Associate Professor, Biomedical Engineering, Stony Brook University
Director, Medical Physics, Stony Brook University

Avraham Dilmanian, Ph.D.
Scientist, Brookhaven National Laboratory
Associate Professor, Radiation Oncology, Stony Brook University

Paul O'Connor, Ph.D.
Senior Scientist, Brookhaven National Laboratory

Craig L. Woody, Ph.D.
Senior Physicist, Brookhaven National Laboratory

This dissertation is accepted by the Graduate School

Lawrence Martin
Dean of the Graduate School

Abstract of the Dissertation

A Light-Sharing Approach to High-Resolution 3D Gamma-Ray Detection for Positron Emission Tomography

by

Srilalan Krishnamoorthy

Doctor of Philosophy

in

Biomedical Engineering
(Medical Physics)

Stony Brook University
2011

Positron emission tomography (PET), on account of its non-invasiveness, exquisite sensitivity, and ability to perform longitudinal studies is becoming a very popular tool in both clinical and preclinical imaging. The increasing role of PET however, has placed increased demands on both spatial resolution and gamma-ray detection efficiency (sensitivity). Developing an efficient, yet high-resolution PET detector has been a fundamental challenge and most attempts to improve resolution make use of smaller scintillation crystals that sacrifice sensitivity.

This dissertation aims to study and investigate in detail, the potential of a novel gamma-ray detector in providing a cost-effective alternative for high performance PET. The detector design comprises a single, continuous

scintillator read out by large-area solid-state photosensors on both sides. In addition to possibly providing high spatial resolution and sensitivity, the detector has fewer readout elements (reduced costs) and could also help reduce parallax errors by measuring the depth-of-interaction (DOI) of the gamma-ray within the scintillator. Moreover the design is expected to be compatible with MRI and would enable simultaneous imaging with both PET and MRI techniques.

An initial prototype detector was built with a 10 mm thick lutetium oxyorthosilicate (LSO) scintillator and large-area avalanche photodiodes (APDs). Due to the use of ready-made electronics, only two channels on the detector were initially instrumented; early promise was demonstrated. Subsequent efforts were devoted towards developing a fully working prototype detector. The efforts ranged from developing a thorough understanding and reduction of electronic noise, to a detailed evaluation and optimization of each detector component. In parallel, a detailed Monte Carlo model of the detector was also built. The model was used to first predict detector performance, and later, to understand in detail the influence of various detector components. To utilize the full potential of the detector, a novel Maximum Likelihood based, 3D event-positioning algorithm was also developed.

Proof-of-concept is demonstrated with an improved version of the prototype detector. Thorough experimental characterization reveals an isotropic resolution of ~3 mm, in excellent agreement with predictions from Monte Carlo simulations. The validated Monte Carlo model was also used to optimize detector design and demonstrate that the above methods, when combined together could realize a high-performance PET detector with spatial resolution better than 1 mm.

To my family,

in loving memory of my grandparents…

Table of Contents

List of Tables

List of Figures

List of Abbreviations

ADC	-	analog-to-digital convertor
APD	-	avalanche photodiode
BNL	-	Brookhaven National Laboratory
Ci	-	curie
^{137}Cs	-	caesium-137
DOI	-	depth-of-interaction
e-	-	electrons
ENC	-	equivalent noise charge
FWHM	-	full width at half maximum
GATE	-	Geant4 Application for Emission Tomography
^{68}Ge	-	germanium-68
keV	-	kilo-electronvolt
LSO	-	lutetium oxyorthosilicate
MRI	-	magnetic resonance imaging
ML	-	maximum likelihood
MeV	-	mega-electronvolt
μA	-	microamperes
^{22}Na	-	sodium-22
nA	-	nanoamperes
ns	-	nanosecond
NIM	-	Nuclear Instrumentation Module
PCB	-	printed circuit board
PET	-	positron emission tomography
PMT	-	photomultiplier tube

RMD	-	Radiation Monitoring Devices Inc.
SiPM	-	silicon photomultiplier
SNR	-	signal-to-noise ratio
3-D	-	three-dimensional
TDC	-	time to digital converter
VME	-	Versa Module Europa

Acknowledgements

First and foremost I thank my advisor Dr. Paul Vaska for providing me the opportunity to work on an exciting project in an area of my interest. During the course of the project there were innumerable hurdles, and his guidance and advice have been instrumental in the outcome. I thank him for his patience, unwavering support, faith and encouragement. Needless to say, this would not have been possible without any of the above. I also thank him for giving me the freedom to seek and explore many other learning opportunities in the lab. I am sure these experiences would stand me in good stead over the years to come.

Thanks to Drs. Terry Button, Craig Woody, Paul O'Connor and Avraham Dilmanian for their time and for agreeing to serve on my thesis committee.

I also take this opportunity to thank members from the RatCAP and CZT-PET team. It was truly gratifying working in such a diverse group and I am sure I learnt from one and all. In particular, I thank Dr. Craig Woody for the guidance, as well as providing an excellent lab to work in; Dr. Schlyer for his support and providing the opportunity to visit the lab when I first arrived at Stony Brook; Sean Stoll for his ever willingness to lend a helping hand; Dr. Martin Purschke who despite being occupied found the time to help with the DAQ; Drs Jean-Francois Pratte and Sachin Junnarkar for the initial help (while I grappled with electronic noise), encouragement and fun they brought to work; Steve Boose for helping with the layout of the detector PCBs; Mike and Bill Lenz for their graciousness in providing full access to their shops. I also take this opportunity to thank the numerous people from

the Instrumentation Division and PET Imaging group with whom I had the pleasure of interacting and working.

Thank you Dr. Button for teaching the many Medical Physics courses and also arranging the annual Medical Physics gatherings. I also thank Drs. Michael Hadjiargyrou and Clinton Rubin for the excellent teachers they were.

Thank you Harsha, Do Hyun, Bosky, Sudeepti and Aarti for enduring me both in and out of the lab; Bob for being the friendly next-door neighbor. I thank the numerous friends and roommates I made over my years (in particular Prakash, Mayuresh and Prakhar) in Stony Brook. Special thanks also to my childhood friend Kuldeep, who while not physically being here, has helped me on numerous fronts.

Finally this list would not be complete without recognizing the support from those closest to me. My parents and sister have always provided the understanding, patience, support and encouragement throughout the course of my studies. Last and by no means least, I also thank the rest of my family and all of those near-and-dear ones who have always been there with their good wishes.

1. Introduction

Ever since the discovery of X-rays by Roentgen, rapid advances in medical imaging technologies have increased the ability to diagnose and treat a variety of conditions. Positron emission tomography (PET) is one such noninvasive imaging technology that provides three-dimensional images of the radioactivity distributions within the subject. Due to its exceptional quantitative powers, PET is gaining popularity not only in helping diagnose disease, but also enabling a fundamental understanding of normal and pathological conditions. Consequently, interests in PET have considerably increased, and its applications range from being used as a research tool in brain imaging [1], pharmacology and drug development [2, 3], to being used as a whole-body imaging modality with applications in neurology [4], and oncology [5, 6]. Genetically modified mice are 'the' animals of interest in biomedical research [7], and the ability of PET to help perform longitudinal studies is of profound importance.

1.1 PET Fundamentals

PET imaging relies on the detection of the annihilation photons arising from the administration of a positron emitting radionuclide. A suitably labeled positron emitter is injected into the subject. After a brief waiting period (i.e. for bioaccumulation), the patient is scanned inside a PET scanner. PET

radionuclides are typically proton rich, and undergo positron decay, resulting in the emission of a positron (equation 1.1). The positron travels a short distance before annihilating with an electron from the surrounding matter to generate two nearly back-to-back 511 keV gamma rays (Figure 1.1).

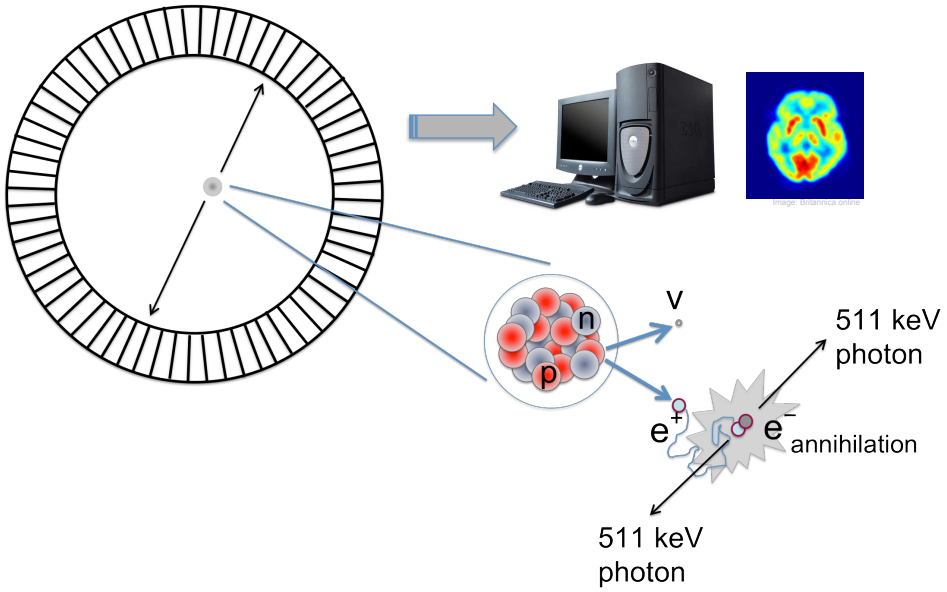

Figure 1.1. An overview of PET imaging. Figure illustrates: Process of positron emission, its subsequent annihilation with an electron in the surrounding media, and detection of the resulting two 511 keV gamma rays by a ring of detectors surrounding the body. The coincidence locations of the 511 keV gammas are fed to a reconstruction algorithm that produces a 3D representation of the radiotracer distribution within the body.

$$ {}^{A}_{Z}X \rightarrow {}_{Z-1}{}^{A}Y + {}^{0}_{1}\beta^{+} + \nu \qquad (1.1) $$

The PET scanner, which is typically a ring of detectors that surround the subject, detects the location of the two gamma rays in coincidence. Since the two gamma rays are emitted at ~180°, the event is localized along a line

joining the two detectors. This line in PET is called as the line-of-response (LOR). The PET scanner, by counting for a long time essentially collects many

Radionuclide	Half life	E_{max} (MeV)	E_{avg} (MeV)	Mode of decay	Applications
^{11}C	20.4 mins	0.96	0.39	β^+ (100%)	Brain imaging (Dopamine receptors)
^{13}N	10 mins	1.19	0.49	β^+ (100%)	Myocardial perfusion
^{15}O	2.04 mins	1.7	0.74	β^+ (100%)	Blood flow
^{18}F	110 mins	0.64	0.25	β^+ (97%) EC (3%)	Glucose metabolism, bone imaging
^{64}Cu	12.7 hrs	0.65	0.28	β^+ (18%) β^-,EC,IC (82%)	Hypoxia tumor imaging
^{68}Ga	68 mins	1.89	0.84	β^+ (89%) EC (11%)	Receptor binding
^{82}Rb	75 s	3.35	1.5 1.16	β^+ (96%) EC (4%)	Myocardial perfusion
^{94m}Tc	52 mins	2.47	1.07	β^+ (70%) EC (30%)	Perfusion imaging
^{124}I	4.2 days	2.13	0.82	β^+ (23%) EC (77%)	Thyroid imaging

Table 1-1: Properties of some frequently used radionuclides in PET imaging.

such gamma-pairs, LOR's. Further, in PET the LOR's are organized by plotting each LOR as a function of its angular orientation versus its distance from the center of the gantry. PET projection data is usually stored in this format, which is also called a "sinogram" [8]. The sinogram is further fed to a reconstruction algorithm, which generates the 3-D distribution of radioactivity concentration in the subject (i.e. image).

FDG (^{18}F-fluorodeoxyglucose), a radioactive fluorine atom attached to a sugar atom is the most common radiotracer. Being a sugar analog, it is used to study glucose metabolism (e.g. in oncology). Similarly, a variety of biological probes can be engineered keeping in mind the task at hand (Table

1-1). PET thus provides an invaluable tool to probe numerous molecular processes *in vivo*.

1.2 Interaction of Radiation with Matter

When high-energy photons pass through matter, they lose energy on account of interactions with atoms of the material. While numerous scenarios are possible, primarily dependent on the energy of the photon, there are three basic mechanisms by way of which the energy transfer occurs:

a. Photoelectric effect,
b. Compton effect, and
c. Pair production.

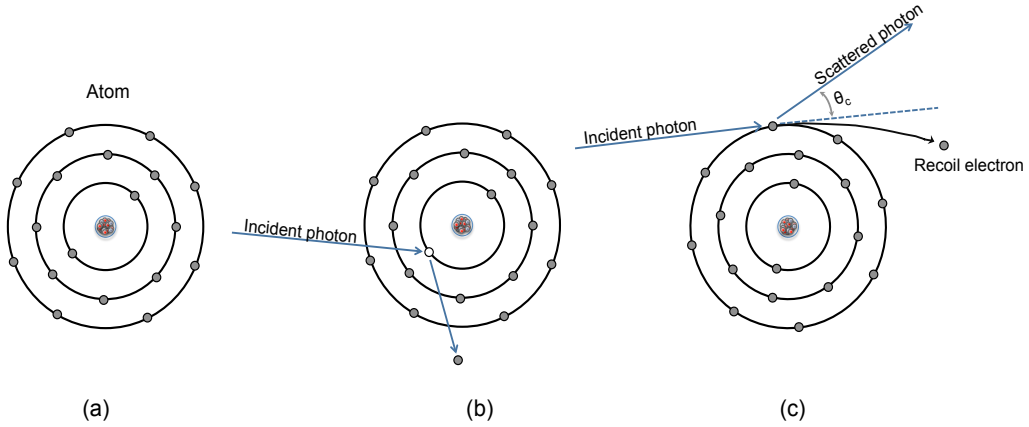

Figure 1.2. The interaction of photons with matter: (a) simplified model of an atom; (b) Photoelectric interaction: the incoming photon transfers all of its energy to a bound electron and in the process knocks it from the shell; (c) Compton scattering: part of the energy of the incoming photon is imparted to a bound electron (recoil electron). The scattering angle is related to the lost energy. Pair production, which occurs when energy of the photon is greater than 1.022 MeV is not depicted above.

At 511 keV, the two most probable interaction mechanisms are:

a. Photoelectric effect:

   In the photoelectric effect, the incident gamma ray transfers all of its energy (E_0) to an orbital electron of an atom in the matter. While part of the energy is used to overcome the binding energy of the electron (E_b), the residual energy is transferred to the electron (E_r).

$$E_r = E_0 - E_b \tag{1.2}$$

   The photoelectric effect primarily occurs with an electron from the innermost shells (highest probabilities for K-shell/L-shell electron), and is followed by the emission of a characteristic x-ray. The photoelectric effect dominates primarily in the low-energy range (<100 keV), and its probability decreases with increasing energies.

b. Compton effect:

   The Compton effect results from the interaction of the gamma ray with an electron from the outer-shell of the atom. The gamma ray only transfers part of its energy to the electron; ejecting it from its orbital (recoil electron), and itself changes direction. The energy of the scattered photon, depending on its energy may further interact. Immediately after its first interaction, its energy can be computed by equation 1.3.

$$E_r = E_0 \Big/ \left[1 + \left(E_0/511\right)\left(1 - \cos\theta_c\right)\right] \tag{1.3}$$

Compton scattering is not equally probable at all energies or scattering angles. The probability of scattering is given by the Klein-Nishina equation (equation 1.4).

$$\frac{d\sigma}{d\Omega} = Z r_0^2 \left[\frac{1}{1+\alpha(1-\cos\theta_c)}\right]^2 \left[\frac{1+\cos^2\theta}{2}\right] \left[1+\frac{\alpha^2(1-\cos\theta_c)^2}{(1+\cos^2\theta_c)(1+\alpha(1-\cos\theta_c))}\right] \quad (1.4)$$

where: '$\frac{d\sigma}{d\Omega}$' is the differential cross-section of the material, 'Z' is its atomic number, 'r_0' is the classical electron radius, and 'α' = $E_\gamma / m_0 c^2$

The Compton effect dominates primarily in the 100 to ~2000 keV range.

1.3 PET Instrumentation

As illustrated by Figure 1.1, a PET scanner typically consists of a series of detectors which surround the subject. The detectors are typically arranged as adjacent rings, and coincidences between various detector-pairs are used to decipher the radioactivity distributions within the subject. The key role of the detector is: to interact with and stop the incoming gamma ray, locate its position within the ring, determine when the event occurred, and finally measure the amount of energy deposited by the gamma ray. The following section reviews some of the important requirements for PET detectors, before briefly describing prevalent approaches for gamma-ray detection in PET.

1.3.1 Detector Requirements

1.3.1.1 Spatial resolution:

Spatial resolution of a scanner typically refers to the smallest distance that can be resolved by the scanner. Since the scanner should have the ability to resolve the finest detail in the image, a detector with the highest spatial resolution is desired. The higher spatial resolution of the scanner should also

help in limiting partial volume effects, thereby improving the quantitative accuracy of the scanner. While the physics of positron emission (i.e. positron range and acollinearity) place fundamental limits on the achievable spatial resolution in PET, current detectors have still not approached that limit. Spatial resolution of the PET scanner is dependent on numerous factors, and Ref. [9] reports empirical measurements to arrive at equation 1.5, which can be used to predict the reconstructed spatial resolution for any PET scanner:

$$R = 1.25\sqrt{(d/2)^2 + (0.0022D)^2 + b^2 + r^2} \tag{1.5}$$

where: 'R' is the reconstructed spatial resolution (FWHM), 'd' signifies the detector size, the '0.0022D' term signifies the contributions arising from photon-acollinearity in a scanner with diameter 'D', 'b' is an additional factor determined by the encoding technique used to readout the crystals, and 'r' is the effective positron range for the radiotracer [10]. Note that while the positron range and acollinearity impose fundamental uncertainties, advances in data processing, and statistical image reconstruction techniques [11, 12] offer the ability to account for and correct them.

1.3.1.2 Sensitivity:

The 511 keV gamma rays in PET are fairly energetic, and require detectors with sufficient stopping power to efficiently detect them. Since the PET camera is essentially a photon counter, the statistical noise (Poisson based) for each detector pair is inversely proportional to the square root of the total number of gamma rays detected. Needless to say, a larger number of detected gamma rays would decrease the statistical noise. For equal scan durations, a more efficient scanner should have lower statistical noise (e.g. Figure 1.3). The lower statistical noise should translate to an improvement in

the image signal-to-noise ratio. Also, the finite half-life of the radiotracer (Table 1-1), and the limit on administrable dose (specific activity and radio-toxicity) necessitate a scanner with the highest detection efficiency. Thus, improving sensitivity should help to:

a. Improve image signal-to-noise ratio, and image quality.
b. Decrease the scan duration.
c. Decrease injected dose per scan.
d. Permit dynamic scans with short-lived isotopes.

The sensitivity of the scanner is defined as the ratio of total annihilation events detected by the scanner to the total number of radioactive decays of the source. It is primarily determined by the detector thickness, and axial acceptance angle of the scanner.

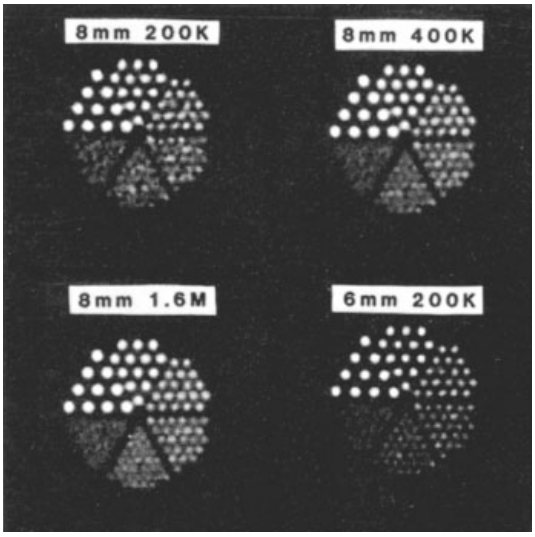

Figure 1.3. Importance of spatial resolution and sensitivity: Simulated Derenzo phantom images demonstrate that image quality can be improved either be improving spatial resolution and/ or sensitivity. Note: The data of top of each of the images represents spatial resolution and total number of counts for that particular image. Figure reproduced from [13].

1.3.1.3 Time resolution:

Timing refers to the ability of the detector to precisely measure the time of arrival of the gamma ray. Since PET relies on accurately detecting the two 511 keV photons arising from the annihilation of a single positron, it is essential that the uncertainties in resolving their individual times of arrival be as small as possible. A larger uncertainty necessitates the use of a larger coincidence window to associate the gamma-pairs. The amount of random coincidences is directly related to the size of the coincidence window. An increase in the random coincidences contributes to statistical noise in the PET image. Hence, the highest timing resolution is desired in a PET scanner.

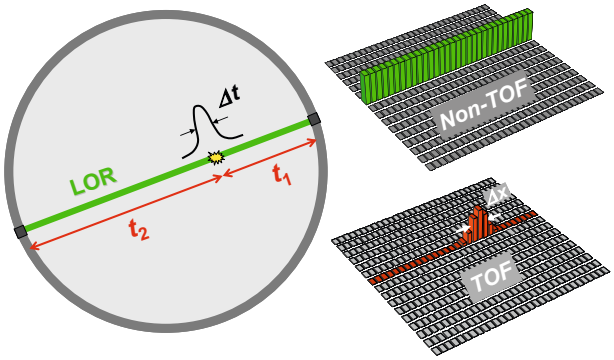

Figure 1.4. Time-of-Flight PET: An illustration of the how TOF-PET helps improve the signal-to-noise ratio in a PET scanner. Also, shown is how conventional PET scanners localize events. Figure reproduced from [14].

A special class of PET detectors, called time-of-flight (TOF) PET detectors possess exquisite timing resolution (< 1ns) [15, 16]. These detectors use the timing information to constrain the annihilation location to a point along the LOR based on the relative time differences of individual arrival times of the respective photons. This directly translates into a direct improvement in the image SNR.

1.3.1.4 Energy resolution:

As described earlier, it is important that the PET detector measure the energy of the incoming gamma-photon. The energy resolution indicates the ability of the scanner to reject scattered radiation. While not so critical for small animal imaging, it is imperative for whole body imaging which has a larger fraction of scattered events. Improving the energy resolution improves the ability to eliminate this source of statistical noise in PET images.

1.3.1.5 Depth-of-Interaction:

As described earlier, typical approaches to improve the sensitivity of a scanner include using a thicker detector material and increasing axial coverage of the scanner. But both the approaches can degrade the overall spatial resolution of the scanner.

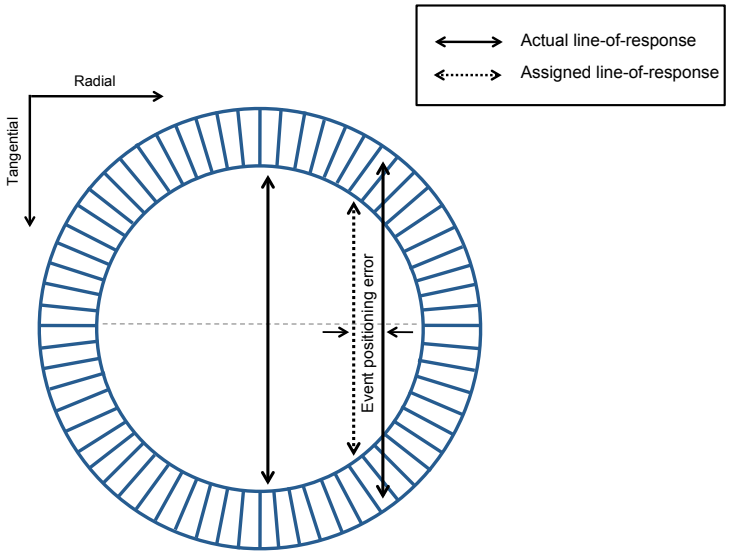

Figure 1.5. Parallax errors in a PET scanner: When the source is placed at off-center locations, the depth-of-interaction of the gamma ray causes an error in determining the correct line-of-response.

As shown by Figure 1.5, when the coincidence events occur at off-center locations, there is an apparent error in determining the correct LOR. The error varies with the depth-of-interaction of the gamma ray. The apparent mis-positioning degrades the overall spatial resolution of the scanner, especially near the edge of the field-of-view of the scanner. This is a serious impediment for building high-sensitivity scanners. A typically work-around is to increase the radius of the scanner.

1.3.1.6 Count-rate:

With all detectors there is a minimum amount of time necessary for the detector to process the event, before it is ready to accept another event. This minimum time is usually referred to as the "dead-time" for the detector, and defines the maximum rate at which the detector can be operated. Due to the fast decaying nature of PET radioisotopes (Table 1-1), the count-rates during a PET scan can vary significantly. While the scanner dead-time has contributions from both the detector and readout-electronics, typically, it is the conversion process within the detector that fundamentally limits the count-rate performance. For example, with a scintillator, it is its decay time; while for a semiconductor detector, it is the drift time of the electron-hole pairs generated from the gamma interaction. While a detailed description of the effects of dead-time on PET performance are not explained here, it is important to note that whatever the mechanism, a detector with the lowest dead time or the highest count-rate capability is desired.

1.3.1.7 Multimodality:

Multimodality PET-CT has already established itself as an invaluable imaging technique. The availability of complementary information from both

the scanners (quantitative information from the PET, and high-resolution anatomical information from the CT) has provided improved diagnostic power in the clinic. Similar efforts have already begun to combine PET and MRI [17-20]. Combining PET with MRI is far more challenging though, as the photodetectors have to work within the confines of static and varying magnetic fields. Developing a MRI compatible detector therefore has the added benefit of extending its use for combined PET-MR imaging.

1.3.1.8 Cost:

Current state-of-the-art small animal PET scanners cost upwards of $500,000, keeping it out of the reach of numerous researchers/facilities. A reduction in cost is definitely desirable to make its use more widespread.

1.3.2 Detection Approaches

While detecting the 511 keV photons in PET it is necessary not only to detect its location within the scanner, but also measure its energy, and its time of arrival. A variety of gamma-ray detection strategies exist. They can be broadly classified as scintillation detectors, semiconductor detectors, and proportional gas detectors. This section briefly describes these various approaches:

1.3.2.1 Scintillation Detectors

Scintillation detectors are by far the most popular, and widely used detectors in nuclear medicine imaging. While there are a variety of scintillation materials, only some have properties suitable for use in PET imaging (i.e. dense, fast and offer reasonably good energy resolution). The scintillation

detector consists of a scintillator coupled with a photodetector, which converts the optical photons into an electrical pulse that is further processed by the readout electronics.

1.3.2.1.1 Scintillators

A scintillator is a material which produces scintillation photons when excited by ionizing radiation. An important property of the scintillator is its ability to generate scintillation photons in proportion to the energy deposited by the gamma ray. The interaction of the gamma ray within the scintillator occurs via photoelectric and Compton interactions. This results in the generation of primary electron-hole pairs that generate secondary electron-hole pairs, which further transfer their energy to luminescent centers from which the final scintillation photons are emitted. A detailed description of the conversion process is described in [21], and outlined in Figure 1.6.

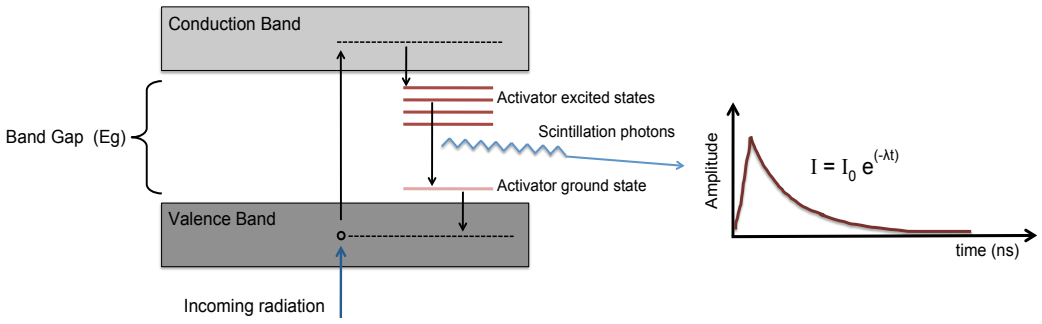

Figure 1.6. Scintillation light production mechanism in an inorganic scintillator.

Scintillator	Sodium Iodide	Barium Fluoride	Cesium Iodide	Bismuth Germanate	Lutetium Oxyorthosilicate*	Gadolinium Oxyorthosilicate*	Yttrium Oxyorthosilicate*	Lanthanum Bromide*	Lutetium Iodide*	Yttrium Aluminum Perovskite*
Composition	NaI:Tl	BaF_2	CsI (Na)	$Bi_4Ge_3O_{12}$	$Lu_2SiO_5:Ce$	$Gd_2SiO_5:Ce$	$Y_2SiO_5:Ce$	$LaBr_3:Ce$	$LuI_3:Ce$	YAP:Ce
Density (g/cc)	3.67	4.89	4.51	7.13	7.4	6.71	4.54	5.29	5.68	5.4
Effective atomic number	50	52	54	73	65	58	34	46	60	32
Linear attenuation coefficient, μ (cm^{-1}) ^	0.34	0.46	0.43	0.96	0.87	0.71	0.39	0.47	0.6	0.46
Light output (photons/MeV)	38,000	1500/9600 ‡	32,000	8200	30,000	9,000	46,000	61,000	75,000	18,000
Decay time (ns)	230	0.7/630 ‡	630	300	40	50	70	20	30	28
Emission Wavelength (nm)	415	220/310 ‡	420	480	420	430	420	380	472/535	350
Refractive index	1.85	1.55	1.84	2.15	1.82	1.85	1.8	1.9	-	1.95
Photofraction (%) per cm ^	5.87	8.51	9.02	39.6	28	17.5	1.92	6.14	16.2	1.99
Compton scatter (%) per cm ^	26.8	35.3	31.9	50.9	53.9	49.3	36	38.7	40	43
Hygroscopic	Yes	No	Yes	No	No	No	No	Yes	Yes	No
Background	No	No	No	No	Yes	No	No	Yes	Yes	No

* Light output and decay time of the scintillator would vary with cerium ion concentration
‡ Fast/slow component
^ at 511 keV

Table 1-2: Comparison of several commonly used, promising scintillation materials for PET. Part of the table calculated with data from National Institute of Standards and Technology, MD, USA.

Important scintillator properties include:

1. High density, stopping power
2. High light yield
3. Fast decay time
4. Appropriate emission wavelength
5. Scintillator transparency
6. Mechanically rugged, non-hygroscopic, and machinable
7. Cost, size, and availability

Table 1-2 presents the properties of several commonly used, promising scintillation materials for PET.

1.3.2.1.2 Photodetectors

The scintillator is coupled to a photodetector, whose main function is to convert the scintillation photons to an equivalent electrical signal. Since there are a variety of scintillators with useful properties, it is important that the photodetector is well matched (size, optical properties, and quantum efficiency) to the scintillator it is coupled with. This shall help preserve and carry over the maximum signal from scintillator. Other desirable properties include: fast response, low noise, rugged design, stable operation, and ability to operate in the presence of magnetic fields. While there are a variety of photodetectors, those most commonly used for PET include:

Photomultiplier Tubes

Photomultiplier tubes (PMTs) are very commonly used to readout scintillators, and have traditionally been the workhorse photodetector for nuclear medicine imaging. They are stable, mature, fast (sub nanosecond) devices, offering high gain (10^6 – 10^7), low noise, and are available in a

variety of sizes and shapes. While PMTs offer excellent signal-to-noise ratios and have low light detection capabilities, they suffer from poor quantum efficiency for blue-light scintillators (typically 20 – 25%). The PMT is a vacuum device, and typically consists of a light-transmitting window, a photocathode (semi transparent layer deposited on the inner-side of the window), followed by a series of electron multipliers, and finally an electron-collecting electrode (anode). The light photons pass the transmitting window, and are incident onto the photocathode surface, which produce electrons in response (photoelectric effect). The electrons are subsequently focused onto a series of electrodes (dynodes), which provides additional multiplication, by the process of secondary emission. The final gain of the signal is determined by the gain at each stage and the number of dynodes in total. Gains of 10^6 – 10^7 are very typical for PMTs. Based on the geometry of the entrance window and the electron multiplier, there are a variety of PMTs available e.g. Circular-cage, MCP, Venetian blind, etc. A major drawback of PMTs is their sensitivity to magnetic fields.

Solid-state photodetectors

Solid-state photodetectors are semiconductor devices, and have several advantages over traditional PMTs. They are compact, have low atomic mass, are rugged, have far superior quantum efficiency (> 70%), and are generally insensitive to magnetic fields. While solid-state technology is still maturing, it has the potential to be mass-produced, and possibly can be inexpensive. The “temperature dependence of gain” is an important concern with most solid-state devices. Silicon photodiodes are the simplest of solid-state devices, and offer unity gain. Their low SNR necessitates the need for ultra-low noise front-end electronics and makes then unattractive to readout

scintillators for PET. Avalanche photodiodes on the other hand are essentially p-n junctions operated under high reverse-bias voltages. The primary electron-hole pairs generated are accelerated through a high electric field region (multiplication region) where through the process of impact ionization they provide internal gain (Figure 1.7). Hence, the APD gain is typically dependent on the applied reverse voltage.

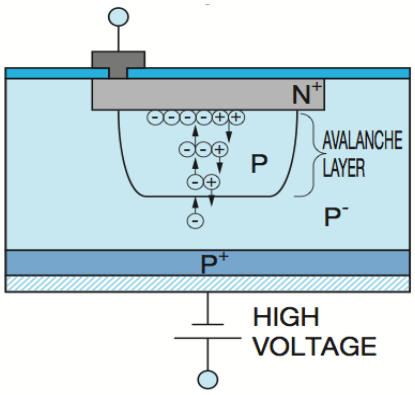

Figure 1.7. Cross-section of a typical Hamamatsu APD [22]. The primary electron-hole pairs generated are accelerated through the electric field and create additional electron-hole pairs via avalanche multiplication.

While the APD has an internal multiplication process, the avalanche mechanism itself has fluctuations, which creates an additional source of noise in APD-based detectors [23]. The statistical fluctuations in APD gain are called excess noise, and it depends on the APD gain and the ionization coefficient for the APD. Also, with APD-based detectors, one has to contend with the electronic noise arising from the leakage current and capacitance of the device. Table 1-3, compares many of the properties for PMTs and APDs.

A very recent development with solid-state devices is the emergence of silicon photomultipliers [24-26]. While still in its infancy, these devices in many ways merge the desirable properties of PMTs with APDs. They are

essentially an array of micro-APDs (micron-sized pixels) tied in parallel and operated in Geiger mode. Thus they are very high gain (10^6), very fast (sub-nanosecond timing), compact, magnetic-field insensitive, operate with low bias voltage, and offer excellent sensitivity to low-light levels. While these devices are still in the developmental stages, they suffer from relatively poor PDE (i.e. photodetection efficiency; SiPM equivalent for quantum efficiency; best ~25%) and are currently available in limited sizes.

Photosensor	PMT	APD
Technology	Vacuum tube	Semiconductor device
Active area	Upto 10" ⌀	Upto 0.6" ⌀
Gain	$10^5 - 10^7$	50 – 1000
Speed of response (ns)	0.1 – 3	2 – 5
Bias voltage (kV)	1 – 3	0.4 – 2.0
Quantum efficiency (% @ 420 nm)	20 – 40	50 – 75
Capacitance (pF)	-	10 – 200
Dark current (nA)	< 10	10 – 1000
Excess noise factor	1.2 – 1.5	2 – 4
Temperature coefficient (%/°C)	0.5 – 1	1.5 – 3
Magnetic field susceptibility	Sensitive	Insensitive
Technology	Mature	Maturing
Form factor	Small to very large	Small
Cost	$$	$$$

NOTE: Typical values quoted

Table 1-3: Comparing avalanche photodiodes with photomultiplier tubes.

1.3.2.1.3 Scintillation detector designs

Scintillation detectors can be broadly classified under two categories. Those that employ a group of segmented scintillation crystals (i.e. discrete

crystal detectors), and those employing a single continuous scintillator (i.e. continuous crystal designs). This section begins with a discussion of the generic scintillation detector designs, and is followed by a discussion of the strengths and weaknesses for both the detector designs.

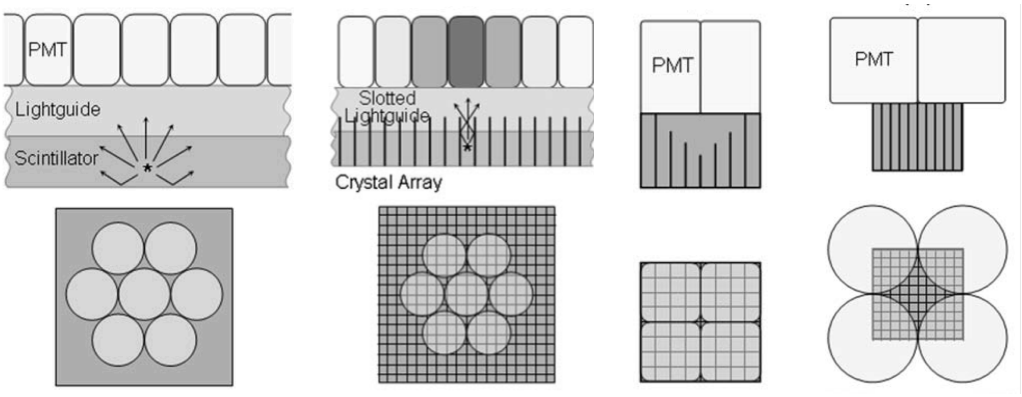

Figure 1.8. Various light-sharing configurations used in PET detectors: (a) classical gamma-ray detector consisting of a continuous crystal read by an array of PMTs; (b) array of scintillation crystals read by an array of PMTs; (c) standard "Block detector"; (d) quadrant-sharing block detector. Figure reproduced from [14].

The earliest PET detectors utilized a 1:1 coupling between the scintillation crystal and its PMT. The need for better resolution, and the simultaneous lack of appropriately sized PMT, resulted in the development of sodium iodide (NaI) based Anger-camera type detectors for PET (Figure 1.8a; [27]). The relatively long decay time of NaI limited the count-rate performance of those detectors. This led to the development of a quasi-Anger-type detector, where a similar light-guide and PMT were used to read segmented scintillators (Figure 1.8b; [28-30]). The use of discrete scintillators limited the light-spread function, and helped improve the count-rate performance of the scanner. A major change in detector design was established with the arrival of the block-detector concept (Figure 1.8c; [31, 32]). The block detector used a limited amount of light sharing to decrease the number of readout

channels. The first detector consisted of an 8 x 8 array of BGO crystals readout by a 2 x 2 array of PMTs. Over the last decade, a variation of the block detector design (quadrant-sharing block detector; Figure 1.8d), which efficiently reduced the total number of required PMTs (factor of 4), was developed. While there was significant reduction in the number of PMTs, clever modifications were necessary for a practical implementation [33-35].

Discrete Crystal Designs

Most of the current PET scanners are of this type [36-40]. The widely used MicroPET scanner is one such example that offers a spatial resolution of 1 – 2 mm [41-43]. Currently, most approaches towards improving resolution in detectors tend to lean towards using smaller crystal sizes [42, 44-46]. Despite providing sufficient improvement in the spatial resolution, the discrete-crystal architecture suffers from the following drawbacks:

1. If a crystal with a fixed thickness were to be progressively segmented, the sensitivity would drop on account of the increasing fraction of dead-space between the crystals. Typically, the space between the crystals is occupied by reflector material. Attempts to reduce the inter-crystal gaps to ~70 μm have been made [47], but the technique has not been furthered for machining small crystal arrays.
2. One way to maintain sensitivity with crystals of smaller cross-section is to make them sufficiently long. But, with longer crystals, it becomes increasingly difficult to efficiently pipe light out of the crystals. The lower light output impacts transverse positioning, energy and timing resolutions.
3. The sensitivity can also be increased by a reduction in the scanner diameter. If this were to be done in scanners employing the smaller

cross-section crystals, a correction for the depth-of-interaction (DOI) would need to be performed. Since most scanners do not account for DOI, this would result in performance degradation as the source is moved away from the center.

4. The number of readout channels is directly proportional to the number of crystal elements. Hence, the cost is linearly proportional to the number of crystals used in the system.
5. The spatial under-sampling near the center of a tomograph employing discrete detectors results in discontinuities in the spatial resolution near the center of the scanner. A mechanical wobble is sometimes used to improve the sampling rate in such cases [48], adding to the complexity of the system design, and also data processing.

Continuous Crystal Designs

As discussed earlier, continuous scintillator gamma-ray detectors have been around for a very long time, and they are still the most widely used detectors in nuclear medicine imaging (i.e. for SPECT – gamma cameras). While the concept has never been applied to small animal scanners, it has been developed and commercialized for human PET applications [49, 50] with encouraging results. Subsequently, [51, 52] investigated the use of a continuous scintillator for PET. But, mostly all groups used a position-sensitive PMT on only one side of the scintillator. Particularly, encouraging results were obtained by [53]. But, the demonstrations were achieved with a rather thin crystal (4 mm) and a position-sensitive PMT (PSPMT). Depth-of-interaction measurements were not investigated. A couple of groups [54-56] have successfully explored the read-out of a continuous scintillator with the S8550 APDs (Hamamatsu Photonics Inc., Japan). While [55] used a rather

thin scintillator and demonstrated the ability to stack these detectors, [56] used neural networks to decode the DOI for the gamma-ray. These approaches while promising still possessed a rather large number of readout channels (arrays of 1.6 x 1.6 mm^2 APDs used). Also, both [55, 56], coupled APDs onto only a single side of the scintillator. While encouraging, these approaches confirm the overall benefits of using continuous scintillators for PET:

1. Improved spatial resolution.
2. Improved sensitivity: The elimination of the dead spaces usually occupied by the reflector material directly provides an increase in sensitivity. The MicroPET-II for example has a 14x14 array of 0.975 x 0.975 x 12.5 mm^3 crystals interspersed with a reflector measuring 0.175 mm. This translates to a packing fraction of approximately 72%. For a similar geometry, the use of a continuous scintillator would provide a two-fold increase in coincidence sensitivity.
3. Improved light collection: The light collection should be considerably better than that possible with long, narrow crystals. This should directly improve the energy resolution, and possibly even timing resolution.
4. Cost-effective: Much reduced machining, polishing, and array fabrication costs involved.
5. A more uniform sampling is available at the center of the tomography, eliminating the need for wobble motion.

Over the last few years, there has been renewed interest in using continuous scintillators, and numerous groups are currently exploring its potential.

1.3.2.2 Semiconductor Detectors

Semiconductor detectors are one alternative to scintillation detectors. Unlike scintillation detectors, the incoming gamma-photon directly produces electron-hole pairs, which are subsequently collected by electrodes. Silicon (Si) and germanium (Ge) are the most commonly used semiconductor materials and have been explored for PET [57-61]. Their low band-gap, and superior conversion efficiency effectively produces a large number of electron-hole pairs; thereby providing excellent energy resolution (< 2 % FWHM). But, Ge cannot operate at room temperature and requires cooling, complicating detector design and increasing costs. Also, Si and Ge have low atomic numbers, yielding relatively poor detection efficiency. Mercuric iodide (HgI_2), cadmium telluride (CdTe), and cadmium zinc telluride (CdZnTe) are more recent semiconductors materials having moderate atomic numbers, and also a wider band gap. With semiconductor detectors, higher pixel granularity can simply be achieved by using appropriately sized readout electrodes (cost effective when compared to segmenting scintillators). Hence, on account of their high spatial, energy resolutions, and moderate detection efficiency, modern-day semiconductors have attracted considerable attention for PET [62-68]. Though they have shown great potential, they still have inferior timing performance. Also, manufacturing techniques have not yet matured, affecting the quality and cost of the materials.

1.3.2.3 Alternative detection strategies

Apart from the above two classes of gamma-ray detectors, there are a few other categories that have been explored and adapted for PET. The

HIDAC, a dedicated small animal scanner [69, 70] based on the multiwire proportional chamber technology (MWPC) is one such example. The HIDAC scanner consists of a MWPC, which incorporates conversion plates to convert the incoming gamma ray into electrons. The conversion plates are composed of laminated plates of interleaved lead and insulating sheets, with a matrix of small holes (0.4 mm) drilled through them. The scanner has DOI capabilities and an excellent spatial resolution of ~1 mm, but suffers from the lack of energy discrimination, poor timing, sensitivity and count rate capabilities. Another variant involves using either a lead convertor [71, 72], or a resistive plate chamber (RPC) to detect the incoming gamma photon [73, 74]. RPCs are low-cost, and exhibit excellent spatial, timing resolutions, but have poor detection efficiency, count rate performance, and lack energy discrimination. Liquid xenon based PET detectors are also being explored, particularly for TOF PET [75-77].

1.4 State-of-the-Art

Over the years PET scanner designs have improved considerably, with clinical scanners achieving best spatial resolutions of 4–5 mm [29, 78]. The current state-of-the-art small animal scanners have spatial resolution of the order of 1–2mm [40, 43, 69]. The ability to visualize finer structures, especially in mice, imposes serious requirements on the spatial resolution of small animal scanners. Further improvements in both spatial resolution and sensitivity need to be made to fully realize the potential offered by small animal models. Sustained developments in the design of PET detectors has meant that PET detectors have evolved from using a 1:1 coupling architecture to modern day light-sharing, and block detector concepts. While

technological developments in scintillator and photodetector technology have a definite role, cost considerations with building scanners have played an important part as well. Block detectors have found favor on account of their multiplexing capabilities.

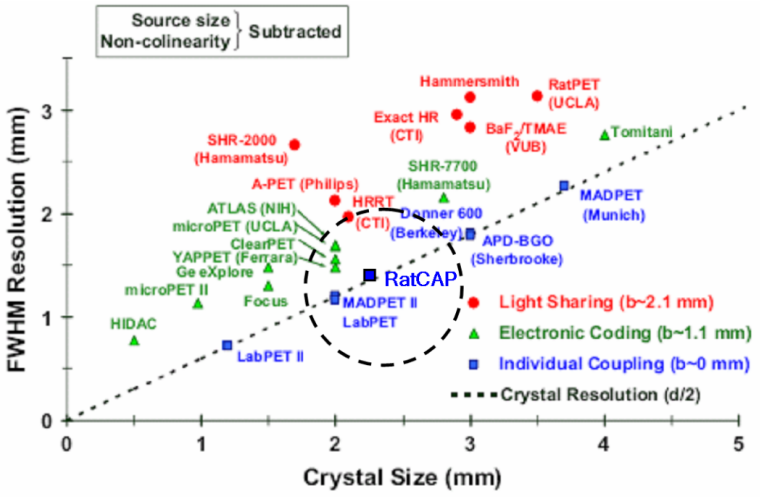

Figure 1.9. Comparison of spatial resolution and crystal sizes for state-of-the-art PET scanners. Figure reproduced from [79, 80]

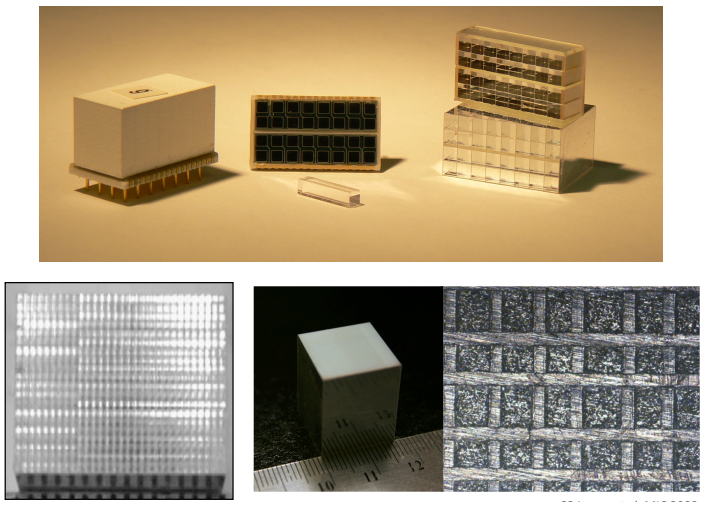

Figure 1.10. State-of-the-art discrete crystal approaches for high resolution PET: *Top row*: ~2 mm^2 crystal arrays used in our RatCAP scanner. *Bottom row:* 0.5 mm^2 and ~0.25 mm^2 arrays being explored by researchers at UC Davis [81, 82].

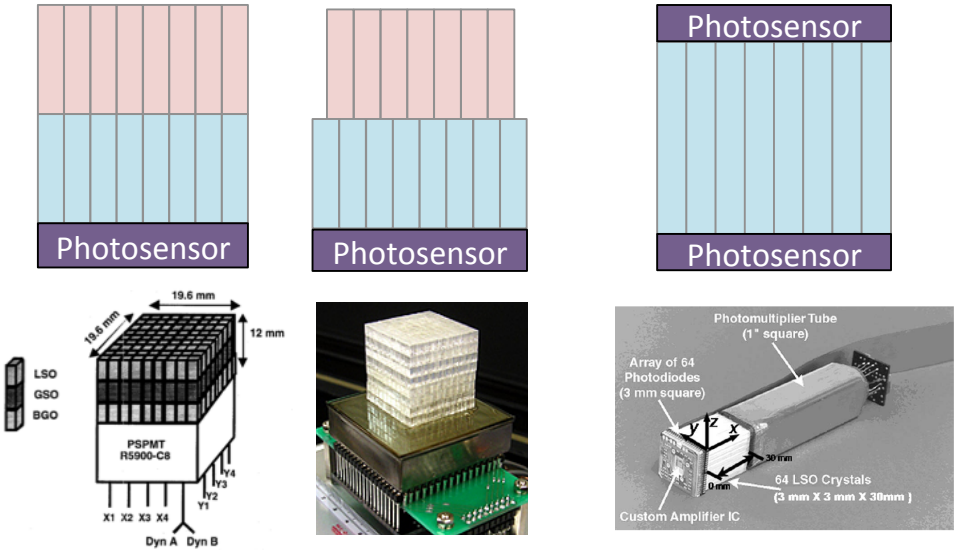

Multi-layered/Phoswich Dual-ended readout

Figure 1.11. Current approaches to determine depth-of-interaction in discrete scintillation detectors: *Top*: A generic representation of the common approaches for DOI determination in discrete scintillation detectors. *Bottom*: Real world examples for the above approaches [83-87].

With an increased emphasis on improving spatial resolution (especially in the preclinical regime), the above detector designs gravitate towards the use of crystals with smaller cross-sections (Figure 1.9, Figure 1.10). While successfully resolving crystals with tiny cross-sections is a challenge in itself (poor light collection; impaired position, energy, and timing resolution), the problem is exacerbated by the need to improve sensitivity. Sensitivity can be improved either by making crystals longer, or increasing the axial coverage. But both of these approaches are prone to suffer from parallax effects, affecting spatial resolution. Current strategies to resolve DOI either include using a phoswich design or a dual ended readout [88-90]. The phoswich design complicates the system design (different decay time scintillators required; possibly variable timing and energy resolutions). Multilayered

detectors (wherein the detectors are either offset, or have special reflectors) have also been proposed, but these designs are expensive to fabricate and also have poor light collection efficiency. Dual-ended readout detectors are other alternative, but this requires at least one solid-state detector. Note that most scanners (NIH-ATLAS and Siemens HRRT being limited exceptions [91, 92]) do not offer DOI.

2. Motivation and Scope of Thesis

Positron emission tomography (PET) is a noninvasive medical imaging technique that provides functional information by mapping the radioactivity distributions within the subject. On account of its exquisite quantitative information content, PET has found numerous diagnostic and therapeutic applications in the clinic. Its impact as a research tool is even more profound, as it allows one to exploit transgenic mouse models to understand the many biological questions at hand. However, current detector technologies do not allow one to visualize details at the spatial scale found in animals like mice. Also, there is a finite limit on the amount of radionuclide that can be injected, and improving sensitivity (to decrease statistical noise in the image; perform dynamic studies) is equally important. Current approaches to improve resolution tend to rely on the use of decreasing crystal sizes. The increase in spatial resolution is often accompanied by a decrease in sensitivity. Sensitivity can be improved, either by making use of longer crystals or by decreasing the scanner diameter. Both approaches however, result in an increased error due to parallax (depth-of-interaction). In summary, many of the current approaches to maximize spatial resolution and sensitivity involve tradeoffs.

This thesis introduces a novel light-sharing, gamma-ray detection strategy. The detector comprises a monolithic scintillator readout by large-area solid-state photosensors coupled onto both sides of the scintillator. The detector is

essentially an evolved, miniaturized Anger-detector (optimized for PET) that utilizes solid-state photosensors. Apart from eliminating the costs associated with manufacturing the discrete scintillation arrays, the use of a single continuous scintillator improves sensitivity on account of the lack of reflector material used in discrete scintillator arrays. An important difference is the absence of a light-guide, traditionally present in light-sharing detectors. The presence of photosensors on both sides of the scintillator also helps in measuring the depth-of-interaction. The use of large-area photosensors, provides a reduced number of readout channels, further decreasing costs. Also, as solid-state devices can work in presence of high magnetic fields, the design in principle is an MRI-compatible design. In summary, this approach could provide a cost-effective solution to improve spatial resolution, sensitivity, and measure depth-of-interaction.

This thesis studies and investigates in detail, the potential of this novel detector as a cost-effective strategy for high performance PET. More specifically: feasibility of the approach is demonstrated with a prototype detector and its future potential is demonstrated via Monte Carlo simulations that have been validated with experimental data from the prototype detector. The specific contributions of this thesis includes:

1. Designing, developing, and characterizing an initial prototype detector.
2. Performing detailed detector optimizations.
3. Implementing and fully evaluating an improved version of the prototype detector.

4. Developing an accurate fully Monte Carlo model for the detector. Validating the model with experimental results from the prototype detector.
5. Developing a novel, Maximum Likelihood based three-dimensional event-positioning algorithm.

3. Detector Design and First Results

Developing an efficient and high-resolution PET detector is an ongoing challenge, and this thesis aims to demonstrate a novel PET detector design that could achieve both. This chapter introduces and describes in detail, the proposed approach. Preliminary studies to design the initial prototype detector, its realization and early results from the same are also discussed in this chapter.

3.1 Detector Concept

The proposed detector comprises a single, continuous scintillator coupled with large-area solid-state photosensors onto both sides (Figure 3.1). The detector is essentially an evolved, miniaturized Anger detector [93], which makes use of improvements in scintillator and photosensor technology to build an improved light-sharing detector.

While traditional gamma cameras have an intrinsic spatial resolution worse than 5 mm, improved spatial resolution in this design is achieved by using a thinner, more appropriate scintillator read-out by suitably sized solid-state photosensors. The narrow cross-section and minimal atomic number of the solid-state sensors allows placing them on both the front and the back faces of the scintillator. Sensitivity is improved on account of using a continuous scintillator. Another significant difference is the absence of a light-guide

traditionally employed by Anger cameras to maintain a uniform spatial resolution throughout the scintillator. Despite the lack of a light-guide, the presence of photosensors on both sides of the scintillator helps maintain overall spatial resolution. Also, placing photosensors on both sides provides the ability to measure depth-of-interaction (DOI) by comparing the signal-distributions from the top and bottom sides. The ability to measure DOI should help in building scanners with smaller diameters, further increasing sensitivity. The use of large-area sensors reduces the number of readout channels, which decreases cost for the scanner. Solid-state photosensors also work well in the presence of high-strength magnetic fields, making this a MRI-compatible design.

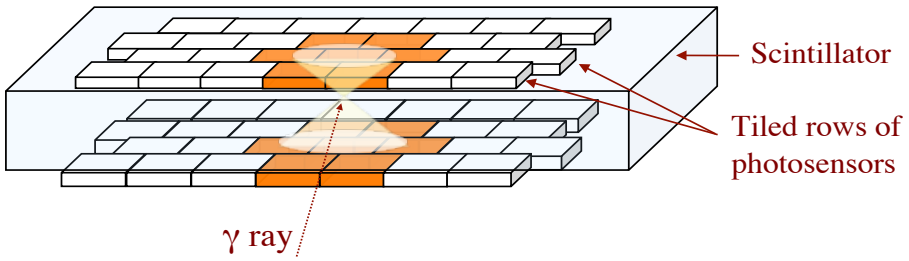

Figure 3.1. A schematic of the proposed detector. Large-area semiconductor photosensors are coupled onto both sides of a single continuous scintillator. Colored APDs indicate APDs that receive scintillation light when a gamma-ray interacts in its vicinity.

To summarize: In keeping with the advantages offered by continuous scintillators, the proposed detector design could possibly provide the following advantages:

1. Improved spatial resolution.

2. Higher sensitivity: For a fixed scintillator thickness, a continuous scintillator provides higher sensitivity by eliminating the dead-spaces found in discrete scintillator arrays (Figure 3.2).
3. Improved light collection; i.e. better energy and timing resolution.

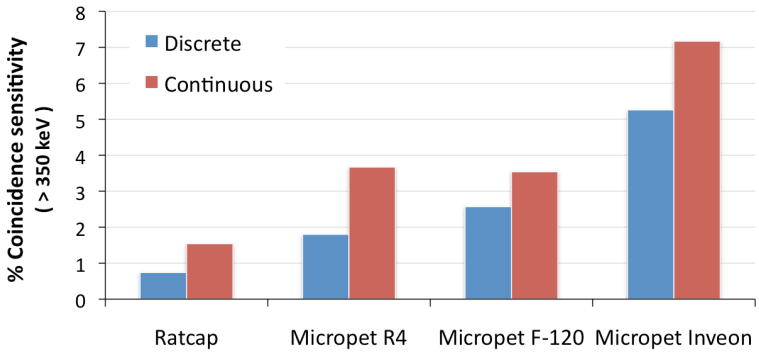

Figure 3.2. An illustration of the sensitivity gains in designing a PET scanner with continuous scintillator. Shown above is expected sensitivity (at the center of the scanner) for a few, "state-of-the-art discrete crystal PET scanners" [38, 41-43] designed with a continuous scintillator. Their existing sensitivity is also shown for comparison. (Data obtained from performing Monte Carlo simulations with the GATE package)

4. The ability to measure depth-of-interaction by comparing signal distributions from the top and bottom sides.
5. A low cost detector, as it eliminates the cost involved in machining, polishing, and assembling the scintillation arrays.
6. The use of large-area photosensors reduces the number of readout channels and cost.
7. A simple, scalable design: The spatial resolution in this design is strongly dependent on the light-spread function. Consequently, a higher spatial resolution can be achieved by simply reducing the scintillator thickness.

8. Since semiconductor photosensors are compact and offer low gamma-ray attenuation, the detectors could be stacked/layered to further enhance sensitivity.
9. As semiconductor photosensors perform well even in the presence of magnetic fields, this design in principle could also be used to build a multimodality PET-MRI detector, scanner.
10. Due to a more uniform sampling obtained at the center of the detector, the need for wobble motion is eliminated.

3.1.1 Decoding Depth-of-Interaction for the Gamma-Ray

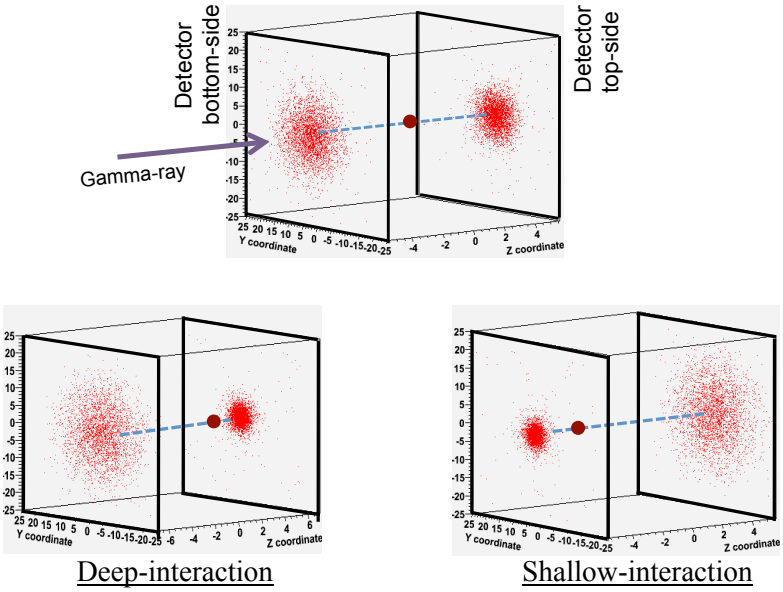

Figure 3.3. Decoding depth-of-interaction for the gamma-ray: Monte Carlo illustration of the signal dispersion for a single gamma-ray interaction (•) inside the scintillator. The signal dispersions on both sides of the scintillator provides a measure of the depth-of-interaction of the gamma-ray.

The proposed detector lacks a light-guide traditionally present in Anger-cameras. This absence is compensated by the availability of photosensors on both sides of the scintillator. The lack of a light-guide and the presence of photosensors on both sides should help in measuring the depth-of-interaction (DOI) for the gamma ray.

For any gamma-ray interaction inside the scintillator, the scintillation light spreads-out isotropically. When the light reaches another surface, its reflection/refraction is dependent on the surface finish and the critical angle (θ_c) for the media. In-effect, the light distributions seen on the top and bottom sides of the scintillator depend on the depth at which the gamma ray interacts (Figure 3.3). DOI for the gamma ray is computed by making use of this light distribution information seen on both sides of the scintillator.

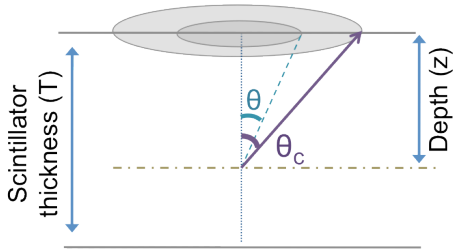

Figure 3.4. Analytically quantifying the depth-of-interaction. Illustration of a gamma-ray interacting at a depth 'z' from the top-side of the scintillator with a thickness 'T'. θ_c represents the angle at which total internal reflection occurs.

The light-distribution measurement can be analytically computed as follows: If a gamma-ray interacts at a depth 'z' from the top-surface of the scintillator with thickness 'T' (Figure 3.4), the solid angle subtended at the top-surface can easily be calculated by equation 3.1. Given the solid angle, the variance of the light-distribution (i.e. its second moment) can be computed by integrating the total flux incident over the surface-area. Mathematically, it

turns out that the variance of the signal distribution is directly proportional to the square of its distance from the interaction location (equation 3.2).

$$Solid\ angle = \int_{0}^{\theta_c} \int \sin\theta\ \partial\theta\ \partial\phi \tag{3.1}$$

$$\text{var}iance\ (\sigma^2)\ \alpha\ z^2 \tag{3.2}$$

$$\sigma_{top} = k_1(z) \tag{3.3}$$

$$\sigma_{bottom} = k_2(T - z) \tag{3.4}$$

$$\sigma_{top} - \sigma_{bottom} = k(z) \tag{3.5}$$

$$dp = \sqrt{\left(\sum_{i=1}^{7} s_i (x_i - \bar{x})^2 \Big/ \sum_{i=1}^{7} s_i\right)} - \sqrt{\left(\sum_{i=8}^{14} s_i (x_i - \bar{x})^2 \Big/ \sum_{i=8}^{14} s_i\right)} \tag{3.6}$$

The signal distributions from both sides can be elegantly combined to obtain a depth-parameter (dp), which is linearly related to the depth-of-interaction for the gamma ray (assuming continuous sampling of the scintillation light). The depth-parameter (equation 3.6) is a continuous function and is representative of the various depths at which the gamma ray interacts. Thus, computing the depth-parameter should help to quantify DOI for the gamma ray. Another way to use the available signal-dispersion information is to use a ratio of "variances of signals from both sides". This depth-parameter (equation 3.7) also varies monotonically with depth, albeit in a more nonlinear fashion.

$$dp = \frac{\sum_{i=1}^{7} s_i (x_i - \bar{x})^2 \Big/ \sum_{i=1}^{7} s_i}{\sum_{i=8}^{14} s_i (x_i - \bar{x})^2 \Big/ \sum_{i=8}^{14} s_i} \tag{3.7}$$

3.2 Proposed Design

The scintillator and photosensor are at the heart of any scintillation detector. This is particularly true in a light-sharing detector where the scintillation-light produced from a single event is shared by multiple photosensors. The light sharing places a special emphasis on the light-output of the scintillator, which directly influences photostatistics. A higher light-output scintillator should improve spatial resolution. Traditional Anger-cameras use thallium-doped sodium iodide (NaI) scintillator (~38,000 photons/MeV; [94]). While NaI has superior light output and good detection efficiency for detecting SPECT gammas (typically 140 keV), it would have to be made quite thick (Figure 3.5) to achieve reasonable sensitivity for PET [50, 95].

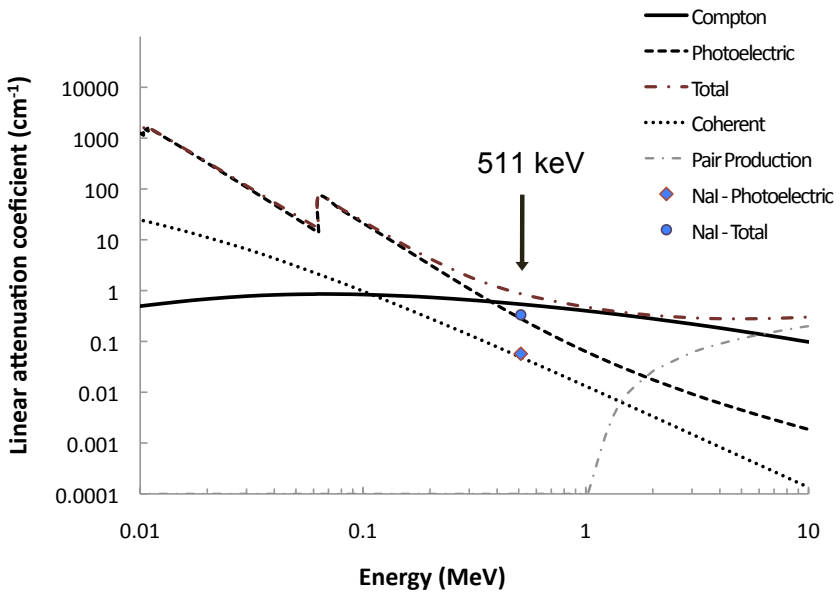

Figure 3.5. Linear attenuation coefficients for LSO as a function of photon energy. Also shown for sake of comparison are corresponding coefficients for sodium iodide (NaI) at 511 keV. Data taken from National Institute of Standards and Technology, MD, USA.

The spatial resolution in this design is also strongly dependent on the scintillator thickness (light-spread function), with a thinner scintillator providing better spatial resolution (admittedly at the cost of sensitivity). Also, NaI has an appreciably long decay time (~250 ns) making it unsuitable for fast timing. The long decay time also affects deadtime and count-rate capability of the scanner. In comparison, cerium doped lutetium oxyorthosilicate (LSO) [96]; with its high stopping power, reasonable light-output (~75% of NaI), and fast decay time (~40 ns) is an excellent choice for PET. A drawback of using LSO is the intrinsic background activity arising due to the presence of naturally radioactive ^{176}Lu [97]. ^{176}Lu has a very long half-life (>10^{10} years) and emits a beta particle and multiple gamma rays in coincidence (Figure 3.6). Thus, the intrinsic background generates a minor increase in the true coincidence rate of scanners using LSO.

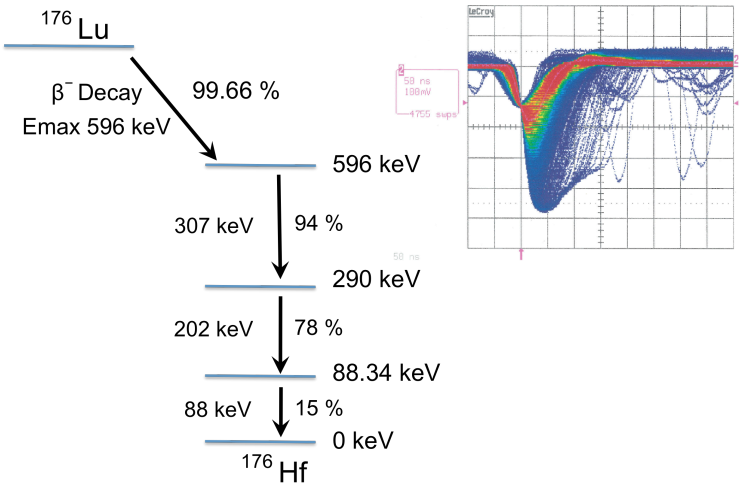

Figure 3.6. ^{176}Lu decay scheme. *Inset:* Scope snapshot from an LSO-APD detector demonstrating how the LSO background signal overlaps signal from a 511 keV source.

More recently, lanthanum bromide ($LaBr_3$), a brighter and faster scintillator than LSO has also been discovered [98-100]. But like NaI it is also hygroscopic and requires much care and packaging while handling. Hence, despite the slightly lower light output and background, it was decided to use an LSO scintillator for building the first prototype detector. In keeping with commercially available small animal scanners, a 10 mm thick LSO scintillator appeared a reasonable first choice. A 10 mm thick continuous scintillator though, should provide improved sensitivity when compared to commercial scanners that use a 10 mm segmented scintillator (e.g. Figure 3.2).

Vendor	Advanced Photonix Inc.	Radiation Monitoring Devices	Hamamatsu Photonics
Device	SD 630-70-74-500	S0814	S8550
Size	30 mm ⌀	11 x 11 mm^2	19.5 x 11.2 mm^2
Active area	16 mm ⌀	8 x 8 mm^2	8 x 4 array of 1.6 x 1.6 mm^2
Gain	200	1000	50
Capacitance (pF)	130	50	10
Leakage current (nA)	280	1000	10
Quantum efficiency (%)	80	50	70
Operating voltage (V)	1700-2000	1700-1800	350-450

NOTE: Typical values quoted

Table 3-1: Comparison of various commercially available APDs for building a first experimental demonstrator [22, 101, 102].

The photosensors in a light-sharing detector must also receive careful consideration. Solid-state photosensors have steadily progressed over the years. Their compact size, package allows them to be placed on both the front and the back side of the scintillator. On account of their ruggedness, compact size, cost, low bias voltage and high quantum efficiency, silicon photodiodes were the earliest devices explored for PET [103, 104]. But, their unity gain

necessitates the use of ultra-low noise front-end electronics. Avalanche photodiodes (APDs) in contrast can achieve higher signal-to-noise ratio (internal gain of 10^2 – 10^3) and are becoming increasingly popular for PET [36-38, 105-107]. The limited gain of the APD though, entails a careful design of the readout electronics.

On account of their compact size, higher signal-to-noise ratio, and availability in appropriate sizes, APDs were chosen for building an early prototype detector. Table 3-1 lists some of the commercially obtainable APDs available for building a first prototype detector. Important considerations in choosing an appropriate APD included: gain, quantum efficiency, total area, fractional active-area, capacitance, leakage current, and excess noise factor.

A major concern for using APDs in this design is the lower signal-to-noise ratio, on account of the lower gain and added electronic noise with using an APD when compared to a PMT. APDs typically have gains in the 100 – 200 range. The electronic noise with an APD roughly scales with the device capacitance and leakage current. Recently, Radiation Monitoring Devices (RMD; Radiation Monitoring Devices, Watertown, MA) had developed a new planar process for manufacturing APDs [108, 109]. These APDs operate at a fairly high bias voltage, but also achieve high gain in comparison with other APDs (order of 10^3). They also have a fairly low capacitance (~0.7 pF/mm^2), and modest quantum efficiency (~50% for LSO). A major concern with the RMD APD though is their large leakage current (>1 μA at the recommended bias voltage). The RMD APDs were available in two different sizes – a version with 13 x 13 mm^2 active area (model S1315), and another with 8 x 8 mm^2 active area (model S0814).

In summary, despite their large leakage current, the S0814 offered a high gain, low capacitance, and modest quantum efficiency in comparison to its contemporaries. Additionally, RMD agreed to customize the APD-packaging to increase the active-area of the APD. The customized S0814 had a total area of ~11.1 x 11.1 mm^2 (i.e. ~50% active area, among the highest). The customized S0814 also was also appropriately sized for a 10 mm thick scintillator. Hence, the S0814 APDs were chosen for building a first prototype detector.

3.3 Preliminary Studies

Important reasons for choosing the S0814 APDs included; a large gain, reasonable quantum efficiency, low excess noise, and an attractive packing fraction. Since the S0814 APDs were somewhat new to the market, it was important for their performance to be verified. While confirming each of its specifications was not a first choice, we decided to examine gain, leakage current, and typical PET performance measures influenced by the above parameters. Specifically, APD gain, leakage current, energy resolution, and coincidence timing resolution were characterized.

The gain of an APD can be characterized in numerous ways: with a pulsed light source, a continuous light source, or with a monoenergetic X-ray (e.g. Fe-55). While all of the above methods were examined, and would not be discussed here, it should be noted that the choice of method has a significant effect on the result. The best method would be the one with the closest match to the application intended. Since the S0814 would be used to detect optical photons we decided to use a pulsed light source to characterize its gain.

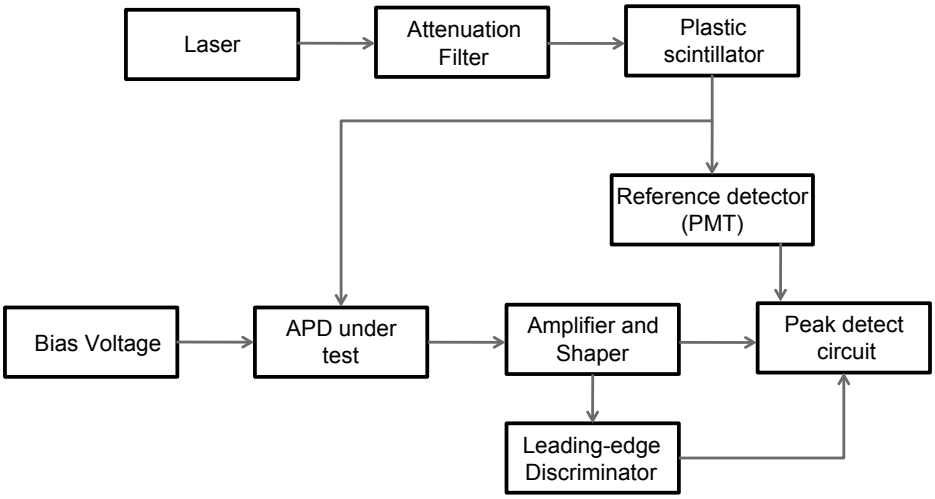

Figure 3.7. APD gain measurement setup.

The gain measurement process is outlined in Figure 3.7. To measure gain with a pulsed-light source, it is important that the source have a stable light output. While the use of an LED is quite common, we decided to use a laser to mimic a pulsed-light source. A nitrogen laser (337 nm) was pulsed at approximately 15 Hz and used to excite a plastic scintillator (BC-420; Saint-Gobain crystals, OH) that emitted fixed light pulses at 420 nm. Light from the plastic-scintillator was coupled to the APD (under bias) via an optical fiber. The output of the APD is fed to a preamplifier-shaper, and further to a peak detecting circuit. A second reference detector was also installed to monitor and correct for possible drifts in the laser output during the measurement process. The entire process was repeated over a range of bias voltages. As the avalanche process is uninitiated at low bias voltages (100 – 200 V for the S0814), the APD is assumed to have unity gain. The gain at any bias voltage is computed by normalizing the APD output at that bias voltage to the corresponding output at unity gain. Gain measured with a single APD is shown in Figure 3.8.

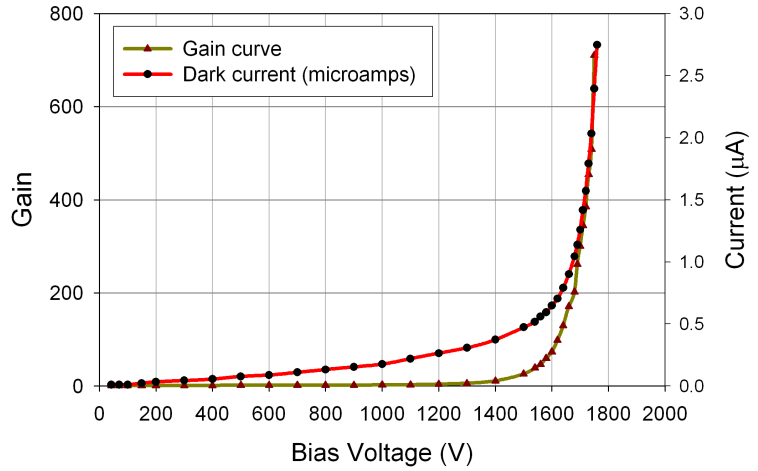

Figure 3.8. Gain and dark current for a single RMD APD measured as a function of its bias voltage.

To measure the dark current, a Keithley picoammeter was connected in series with the bias circuit. All measurements were performed inside a light-tight box and at room temperature. Figure 3.8 shows the gain and dark current measured for a single S0814 APD. As expected, the S0814 had a large leakage current (> 1 μA) and high gain (~500) at bias voltage of 1700 V.

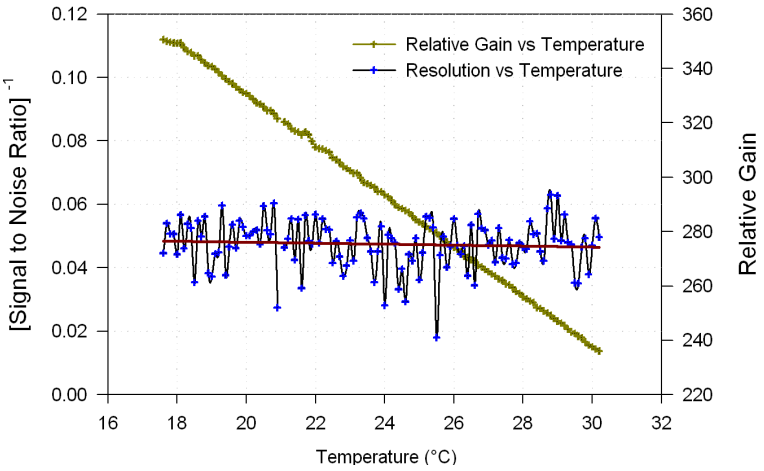

Figure 3.9. Characterizing the temperature dependence of the gain for the RMD APD. The gain was measured to decrease by 2.5% for every degree Celsius rise in temperature.

Given the temperature dependence of the gain of the APD, gain variations for the APD were also characterized over a wide temperature range. The above setup was placed inside a light-tight, insulated box. A heater-coil (Minco, Minneapolis, MN) and ice pack were used to vary the temperature from 17.5 to 30.2 °C. A resistive thermal device (model S651; Minco, Minneapolis, MN) placed in direct contact with the APD surface monitored the temperature. The pulsed-light setup used to measure gain was used to deliver a fixed light pulse over the entire temperature range. By monitoring the APD output relative to its temperature, a dependence of -2.5%/°C was measured (Figure 3.9).

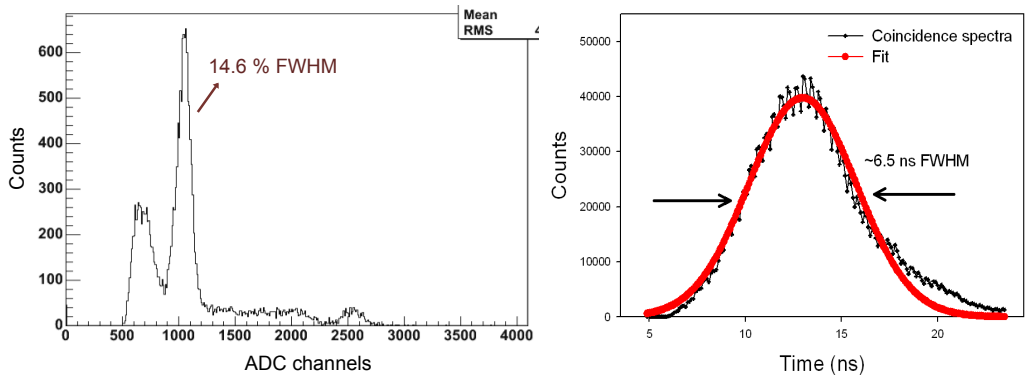

Figure 3.10. *Left*: Energy spectra acquired from a Na^{22} point source with a single, Teflon wrapped 2 x 2 x 18 mm^3 LSO crystal on the RMD APD. *Right*: Coincidence time spectra measured with the same setup and a fast preamplifier in coincidence with a fast BaF_2-PMT detector. An energy resolution of 14.6% FWHM, and time resolution of about 6.5 ns FWHM was measured.

Energy and timing resolution measurements were also carried out with the S0814 APD coupled to a single 2 x 2 x 18 mm^3 Teflon wrapped LSO crystal. A single APD was biased (1680 V) and readout with a BNL designed, fast, 70 ns preamplifier-shaper combination. For the energy measurement, the amplified and shaped APD output was fed to a standard fan-out module, and

subsequently to a charge integrating analog-to-digital converter (ADC). Timing resolution was also measured with the above setup in coincidence with a fast BaF_2-PMT (PMT Model 5023; Hamamatsu Corp, Japan) combination. A standard Lecroy leading edge discriminator (model 621L; Lecroy Corporation, NY) was used to generate a logic-pulse for both the detectors. Both the logic pulses were further fed to an 11-bit time-to-digital converter offering 100 ps resolution (model 2228A; Lecroy Corporation, NY). While the measurements were not fully optimized, an energy resolution of 14.7% full width at half maximum (FWHM) and coincidence time resolution of 6.9 ns FWHM was measured at 511 keV (Figure 3.10).

During the characterization process, it was found that the customized packaging (to decrease the dead-area of the APD) made the APDs susceptible to moisture/humidity. Hence, to protect them, the APDs were initially baked and care was taken to place them in a dry environment (dessicator). Later, a moisture sealant was applied at the edges to eliminate the problem.

3.4 Initial Simulation Studies

Simulation studies provide an efficient and economical technique to develop, assess, and validate detector performance. While a variety of simulation tools are available, they broadly fall under two categories: Analytical simulations and Monte Carlo simulations. The former, albeit simpler, uses approximations to facilitate and speed simulations. Monte Carlo simulations on the other hand are more sophisticated, thorough, and computationally intensive. A more detailed explanation of the theory of Monte Carlo simulations and its relevance in simulating medical imaging

systems can be found in [110-112]. In case of the proposed design, while improved spatial resolution was expected due to a decreased light spread function, performing simulations to predict detector performance was rational.

Due to its simplicity, a first evaluation of detector performance was performed with the help of an analytical model. The model assumed a relatively straightforward light transport mechanism, and the gamma ray depositing all of its energy at the interaction location. It accounted for, the scintillator light yield (conservative 15,000 photons/MeV) and non-proportionality (~10%), electronic noise (5000 e- rms), APD quantum efficiency (50%), APD gain (500), and APD excess noise (2.8). 511 keV gamma interactions were simulated at various locations inside the scintillator. For each event, the amount of light reaching an APD was calculated based on the solid angle subtended by the APD. Position and energy calculations were restricted to groups of seven APDs from both sides of the detector. Gamma-ray interactions were simulated at fixed depths and at various locations along the face of the detector. An average spatial resolution of ~1 mm FWHM and energy resolution of ~15% FWHM was estimated, suggesting that the approach could yield a high performance detector.

While the simplified analytical model was a good starting point, a more accurate and realistic model was necessary to evaluate detector performance under more demanding conditions. A detailed and validated simulation helps predict system performance, and also offers the flexibility to validate the effect of altering various design parameters. For this detector, the detailed simulations should particularly take into account gamma-ray interactions, their energy deposition and also accurately track the optical photons generated inside the scintillator.

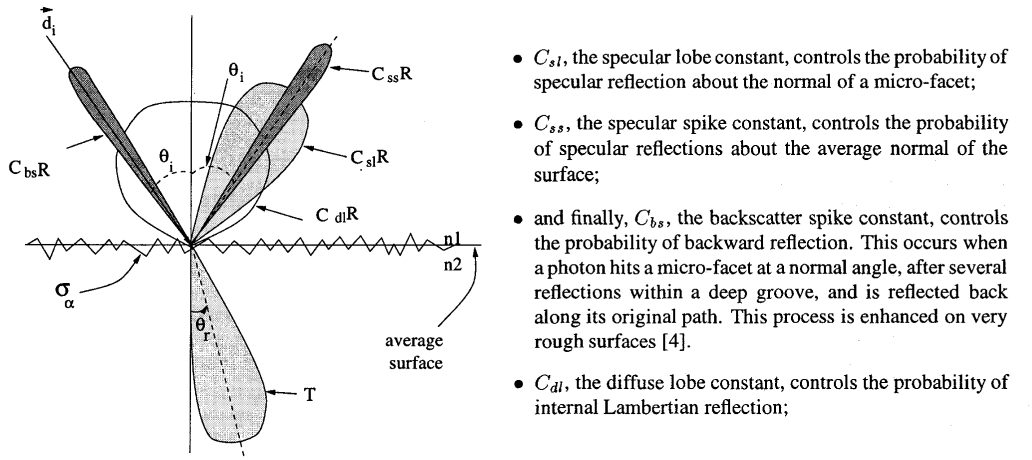

Figure 3.11. Depiction of how the DETECT2000 package allows incorporation of sophisticated surface models, allowing accurate tracking (reflection, refraction or transmission) of photons. Figure reproduced from [113].

There are numerous open-source Monte Carlo simulation codes [114] that have been extensively used to simulate nuclear medicine imaging systems, e.g. SimSET [115], GEANT4 [116, 117], DETECT2000 [118, 119], MCNP [120], GATE [121, 122]. Also, there are specialized, proprietary packages like OptiCAD [123, 124] and ZEMAX [25, 125, 126] that lack gamma-ray transport, but specialize in modeling and optimizing complex optical systems. DETECT2000 is a popular Monte Carlo package [127-129], which models in detail the optics for scintillation detectors (Figure 3.11). Since the optical photon transport mechanism is an integral and critical part of this design, despite the minimal gamma-ray transport, we decided to choose the DETECT2000 package.

A separate program, BUILDER [130], included with the DETECT2000 package was used to build the detector model. Since the goal was to build an accurate detector model, realistic values were assumed while generating the model. The detector was modeled as a single LSO disk (10 mm thick and 6 cm

in diameter) with seven APDs, each measuring 11 x 11 mm^2 (8 x 8 mm^2 in active area) coupled onto both sides of the scintillator. The two flat surfaces of the scintillator were modeled to have a polished finish ("POLISH"). The shorter edges were modeled as "GROUND" and had a reflection coefficient of 0.1 to model a non-ideal, light absorbing black-paint that was applied to eliminate reflections at the edges. The scintillator was modeled to have a refractive index of 1.82, and a peak emission wavelength of 420 nm [131]. The scintillator was assumed to have a light yield of 20,000 photons/MeV. To make it more realistic, an appropriate amount of noise representing the ~10% FWHM intrinsic resolution for LSO [132] was added. The APD was modeled to have a quantum efficiency of 52% at the peak emission wavelength of the scintillator [102].

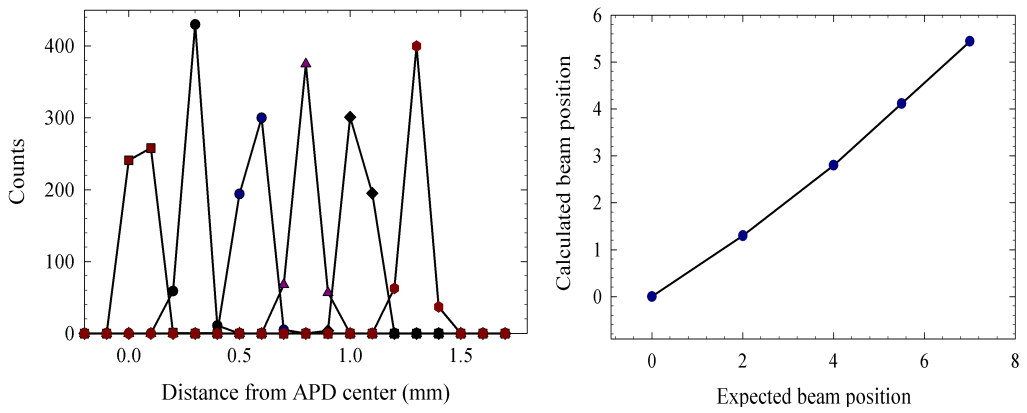

Figure 3.12. (*Left*) Position histograms and (*Right*) linearity of the detector for fixed point, photoelectric interactions, occurring at a depth of 5 mm. Data simulated using the DETECT2000 Monte Carlo package.

To estimate the spatial resolution of the detector, ~500, 511 keV photos were made to deposit their entire energy at a depth of 5 mm inside the scintillator. The entire process was repeated for various locations along the face of the scintillator. For each gamma-interaction, the DETECT2000

package generates a proportional number (~10,000) of scintillation photons isotropically. It then individually tracks each photon to account for their surface interactions (reflection, refraction, and transmission) through various components of the detector. Optical tracking is performed until the photon is: absorbed inside the scintillator, detected by a photosensor, or escapes the detector volume. For the simulation to accurately perform these tasks, the mean free path lengths for absorption (300 mm) and scatter (256 mm) in LSO were also included [133]. To provide a measure of the signal from each APD, the number of photons reaching each APD is factored with the APD gain (450). To make it more realistic, an electronic noise of 5000 electrons rms and an accurately known excess noise factor for the APDs [134] were also included.

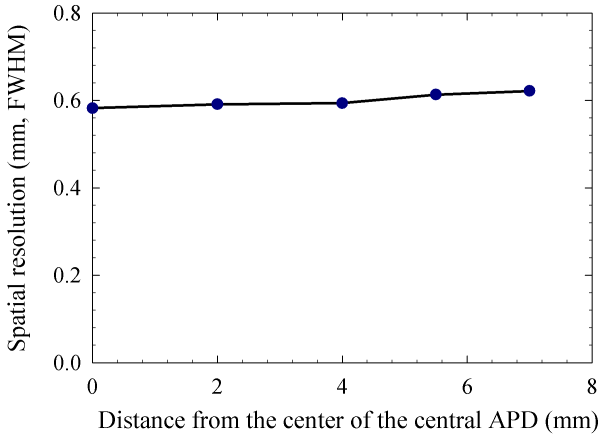

Figure 3.13. Spatial resolution simulated (DETECT2000 package) across the face of the detector for photoelectric interactions occurring 5 mm deep into the scintillator.

For each interaction location, the transverse position was computed with traditional Anger-logic (equation 3.8) using all 14 APDs. Figure 3.12 shows the position histogram for multiple beam positions along the face of the detector. Since the position response is expected to be non-linear (Figure

3.12), a position dependent calibration was used to correct, and also characterize the transverse spatial resolution (Figure 3.13). An excellent spatial resolution of ~0.6 mm FWHM was observed, further supporting the potential of this approach.

$$position = \sum_{i=1}^{14} x_i s_i \Big/ \sum_{i=1}^{14} s_i \tag{3.8}$$

3.5 Design of a First Prototype Detector

Based on our earlier simulations, it was expected that a 10 mm thick LSO scintillator should provide good resolution and sensitivity when compared to prevailing systems. Also, the S0814 APDs seemed to be appropriately sized to provide a minimal number of readout channels. Hence, we decided to construct a first prototype with a 10 mm thick LSO scintillator and the S0814 APDs from RMD.

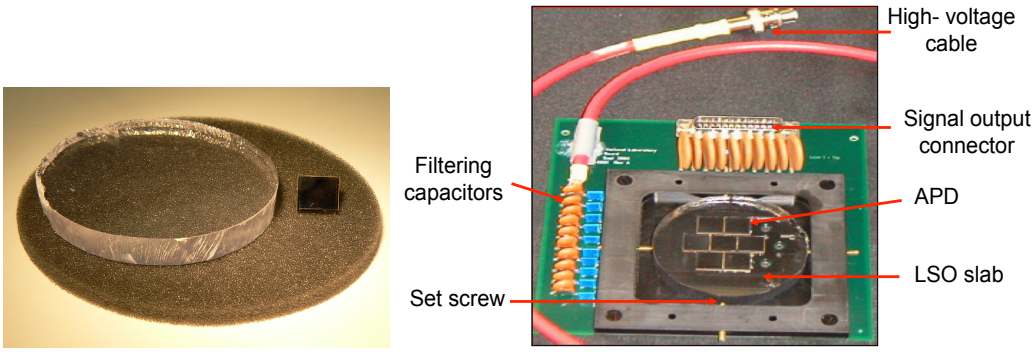

Figure 3.14. A first prototype detector: *Left*: The scintillator (6 cm diameter, 10 mm thick LSO slab) and a single RMD avalanche photodiode (total size of 11 x 11 mm^2) used in the first prototype. *Right*: Assembled first prototype detector showing the LSO slab and APDs tiled on one side of the crystal. A similar arrangement of APDs (not shown for sake of clarity) is used to readout the other side of the crystal.

Specifically, a 10 mm thick, 6 cm diameter LSO scintillator was purchased from CTI (formerly CTI PET systems, now part of Siemens Medical Solutions, Knoxville, TN). Custom printed circuit boards (PCBs) were designed to mount the APDs. Each board distributed the bias voltage, and routed the output signals for up to 10 APDs. For the initial design, we decided to limit ourselves to using a hexagonal arrangement of seven APDs on each board (Figure 3.14). The board also included current limiting resistors and capacitors to filter the bias voltage. Though each APD has a separate bias voltage feed line, for the sake of convenience, all the APDs were operated with a common bias voltage. The detector output was capacitively coupled to the input of a 12-channel preamplifier-shaper unit through a standard DB-25 connector. A black Delrin block was machined and mounted on the PCB to, provide a mounting area, and to ensure accurate alignment for the APDs and crystal.

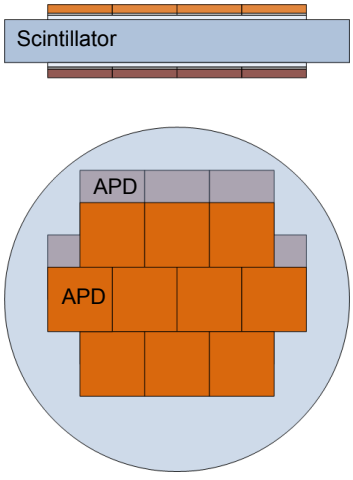

Figure 3.15. Layout of APDs used in the prototype detector. To maintain detector sampling over the useful area of the detector, APDs on either side were offset relative to each other.

To easily adjust the position of the scintillator set screws were also included. The boards were designed with a low profile because two boards had to be used, one on each side to enable APD readout from both sides of the crystal. The board also had a provision to align and maintain the positions of the boards relative to each other. The flat surface of the crystal was polished, and the edges were covered with a black light absorbing paint to eliminate edge reflections. Since the packing fraction of each APD is only about 50%, to maintain detector-sampling and resolution, the detector boards on both the sides were offset relative to each other in one direction by one-half of the APD pitch (Figure 3.15). To ensure good optical coupling between the scintillator and the APDs, a thin layer of silicone (Sylgard-527; Dow Corning Corporation, Midland, MI) was used.

3.5.1 Readout Electronics

The limited gain of the APD necessitates the use of a preamplifier to read-out the detector. The initial goal was to develop a proof-of-concept demonstrator. Hence, to expedite instrumentation of the detector it was decided to make use of readily available electronics. The detector output was capacitively coupled to a 12-channel hybrid preamplifier-shaper box (housing a fast, 70 ns preamplifier-shaper combination) made for an unrelated nuclear physics application. Preliminary use of the electronics to read-out a single APD (coupled with a single 2 x 2 x 18 mm^3 LSO crystal) indicated reasonable signal-to-noise ratio. But when coupled to the prototype detector, the electronic noise was excessive. While a thorough evaluation and optimization of various noise sources in our setup was

definitely in order, we initially limited ourselves to quantifying electronic noise arising from the front-end electronics alone.

The noise performance of an amplifier is typically stated in terms of an equivalent noise charge (ENC). The ENC represents the noise level at the input of the amplifier and provides a measure of the signal (needed at the input of the preamplifier) that would provide a signal-to-noise ratio of one. To measure ENC, a single APD was biased and connected to the fast preamplifier-shaper combination. Electronic gain for the preamplifier was measured by injecting a fixed amount of charge (model DG-535; Stanford Research system, Sunnyvale, CA) onto a test capacitor provided at the preamplifier input. The total noise at the output of the shaping amplifier was measured with a true-RMS meter (Rhode and Schwarz, Munich, Germany). Since the ENC is strongly dependent on the APD bias voltage and shaping time of the amplifier, their effects were also characterized (Figure 3.16).

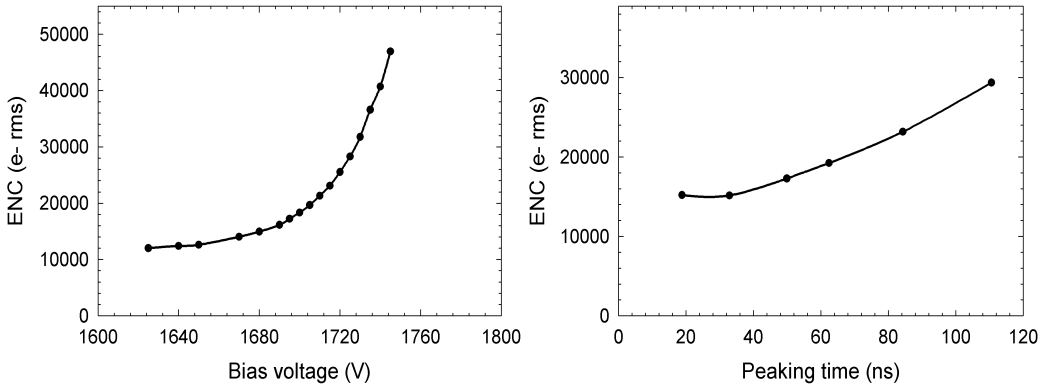

Figure 3.16. Electronic noise measurements for a single RMD APD readout with a BNL designed fast preamplifier-shaper combination. Since the electronic noise is related to both, the bias voltage (*left*) and shaping time (*right*) their effects were investigated on the above combination.

While a redesign of the preamplifier was beyond the scope of this work, to expedite construction of a first working prototype detector, we decided to explore a slower preamplifier (also BNL designed; IO-446) that was immediately available. Similar noise measurements were performed (Figure 3.17) with a single RMD APD biased and connected at its front-end. Though still not fully optimized, the slower preamplifier offered a significant reduction in the ENC (~10,000 e- rms). The slower preamplifier was though incompatible with the 12-channel preamplifier-shaper unit that housed the fast preamplifier-shaper combination. Hence, in order to build a working prototype, only two APDs on the detector were instrumented with the slower preamplifier-shaper combination.

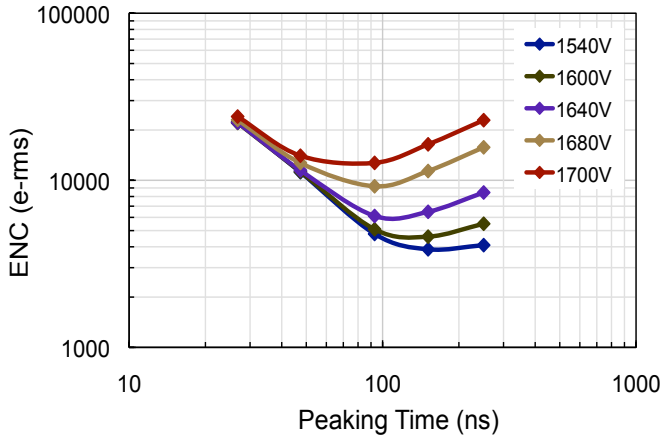

Figure 3.17. Electronic noise measured with the RMD APD connected to a BNL designed slow preamplifier and an Ortec shaping amplifier offering variable shaping time. Though sub-optimal, the above combination offered significantly lower electronic noise than the fast preamplifier-shaper combination (see Figure 3.16).

Overall, the detector readout electronics consisted of the BNL designed slow preamplifier-shaper combination, followed by standard NIM electronics (Figure 3.18). The signal from each APD, after being capacitively coupled to a preamplifier, was followed by a 200 ns shaping amplifier (BNL designed) and

finally to a VME charge integrating ADC (model V792; CAEN S.p.A, Italy). An analog sum from both the APDs (model 428F; Lecroy Corporation, NY), and a leading edge discriminator (model 708; Phillips Scientific, Mahwah, NJ) was used to generate the trigger. PDAQ [135], a general-purpose data acquisition software, written and developed at BNL was used to acquire data. The ADC data was written to a Linux machine, and later analyzed using the ROOT package [136, 137].

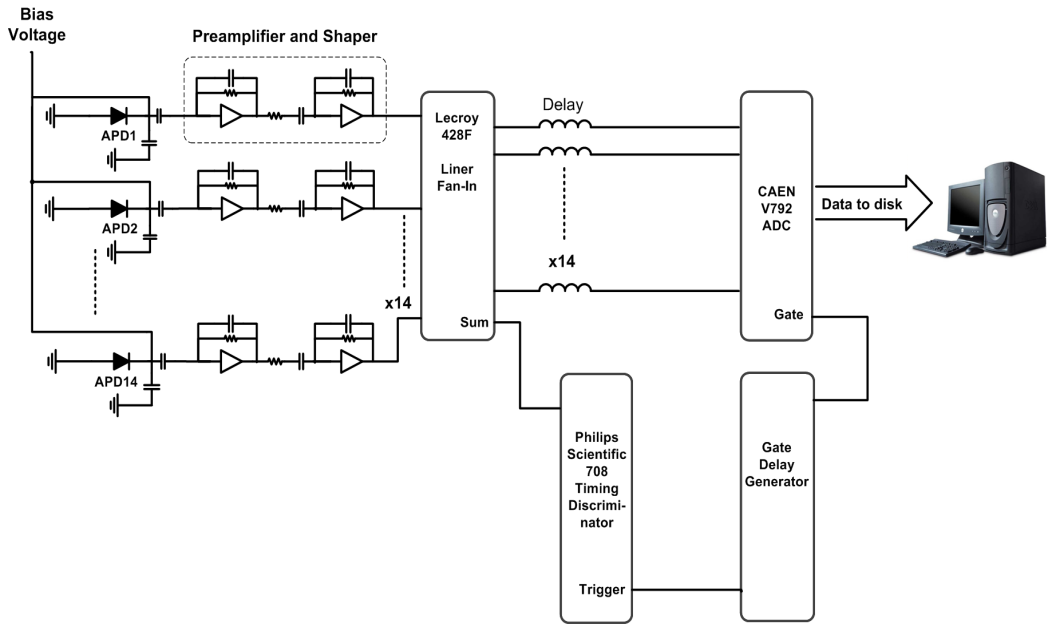

Figure 3.18. Schematic of electronics used to read the first prototype detector.

3.6 Initial Characterization

Since a collimated source is required to characterize the spatial resolution of a light-sharing detector, an experimental setup containing a collimated source was assembled. The source consisted of a ~4 mCi, ^{137}Cs disk housed inside an ~4.5" diameter x 5.5" long lead collimator having an

aperture ~2 mm in diameter. The collimated source was mounted onto a computer controlled X-Y translational stage (Velmex Inc, Bloomfield, NY) that could be stepped in 100-micron steps across the face of the detector. The assembled detector and associated front-end readout electronics was housed inside a light-tight box and the collimated beam assembly was directed onto the under-side of the light-box (Figure 3.19).

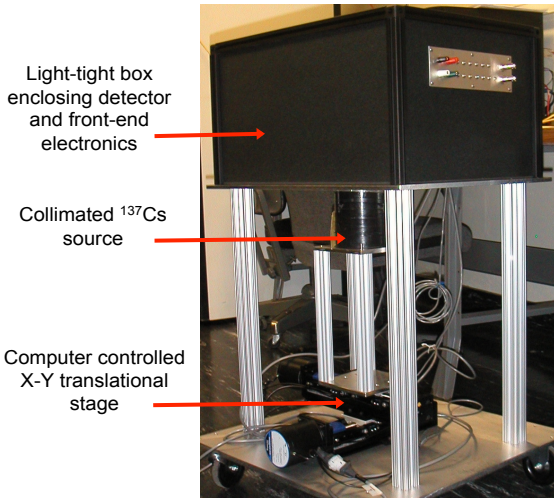

Figure 3.19. Mechanical setup for characterizing detector performance.

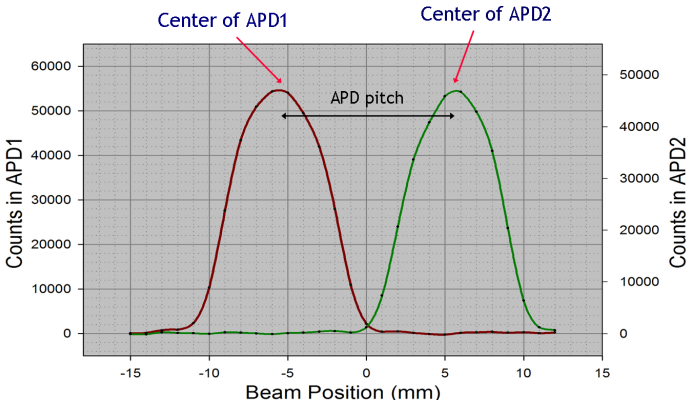

Figure 3.20. Detector response with the collimated source scanned across the face of the APDs. The response was used to locate the position of the beam relative to the detector.

Before assessing the performance of the detector, it was necessary to establish the relative positions of the detector and the collimated source. This was accomplished by stepping the collimated source across the beam across the face of the detector in 1 mm steps. Figure 3.20 shows a scan profile for two adjacent APDs on the bottom board. Besides providing their relative positions, the profile also accurately indicated the pitch of the APDs (~11 mm).

After determining the relative position of the beam and the detector, spatial resolution was measured by stepping the collimated source in 1 mm increments along the face of the APDs on the bottom board. Energy for the event was measured by an analog sum of the APD channels and transverse position was determined by using traditional Anger-logic (equation 3.8).

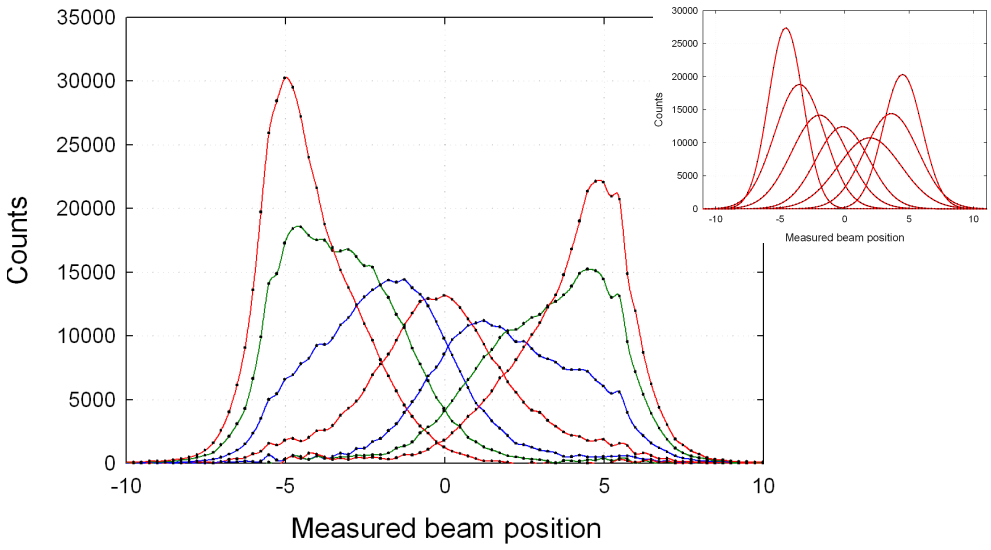

Figure 3.21. Position histogram (prototype detector) obtained for various beam positions across the face of the detector. *Inset*: Gaussian fit to the position histograms.

For each beam position, the centroids were computed and later histogrammed. Then a Gaussian fit was used to compute the spatial resolution for that beam position. Figure 3.21 shows the computed centroids (as well as the Gaussian fit) for each beam position. To account for the nonlinear response of the Anger positioning algorithm (Figure 3.22), a local calibration (i.e. calibration dependent on the beam position) was used for each beam position. Without accounting for the size of the beam, a spatial resolution of ~2.5 mm FWHM was measured between the centers of the two APDS (Figure 3.22).

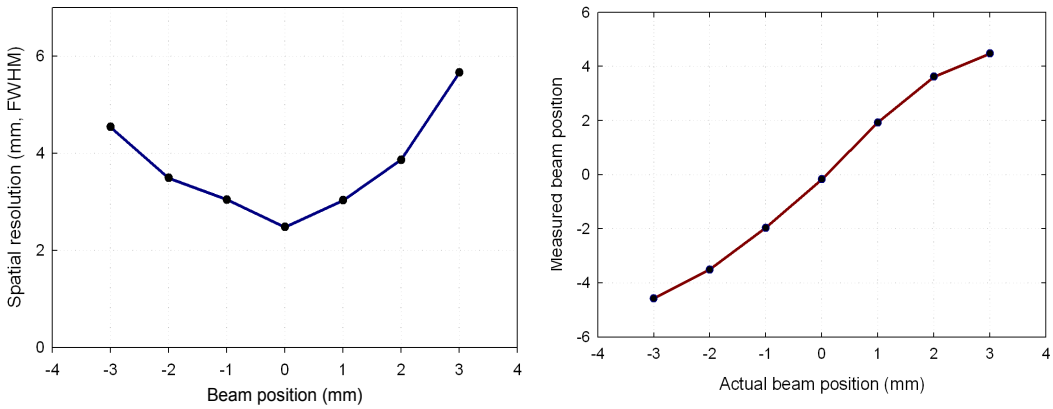

Figure 3.22. *Left*: Spatial resolution of the prototype detector for beam positions across the face of the detector. To correct for the nonlinear response of the detector (*right)*, a position dependent calibration was used to characterize spatial resolution.

4. Detector Optimization Studies

Chapter 3 discussed the design, implementation and characterization of an initial prototype detector, built using a 10 mm thick LSO scintillator and large-area APDs from RMD. Due to the excessive electronic noise in the setup, only two channels on the detector were populated and a spatial resolution of ~2 mm FWHM was measured between the centers of those two APDs.

This chapter discusses the various optimization procedures employed to improve performance of the initial prototype. The efforts ranged from developing a thorough understanding and reduction of electronic noise, to a detailed evaluation and optimization of each detector component. The development of an improved, fully Monte Carlo model for the detector is also discussed. Overall, the goal of this chapter is to help design a fully instrumented prototype detector.

4.1 Electronic Noise Optimization

Early characterizations of the initial prototype were corrupted by the excessive noise present in the experimental setup. Preliminary studies pointed to the noise arising from the read-out electronics as being the most dominant source. The next generation prototype clearly required a reduction in the electronic noise. While a complete redesign of the front-end electronics was beyond the scope of this work, the primary purpose was:

a. To analyze in detail various noise sources, and optimize them to decrease the total ENC.
b. To find suitable, affordable, ready-made electronics that would provide sufficiently low-noise, so as to instrument a fully working prototype detector.

4.1.1 Noise Sources in a Detector-Amplifier Circuit

Typically, the gamma-ray interaction in any detector produces a pulse, the area of which is proportional to the energy deposited by the gamma ray. A preamplifier, whose main purpose is to amplify and faithfully reproduce the pulse, immediately follows the detector. The preamplifier could either be a voltage-sensitive, current-sensitive, or charge-sensitive preamplifier. A voltage amplifier simply amplifies the voltage appearing at the output of the detector. Since, in this case, the intrinsic impedance of the detector (capacitance) manifests the detected pulse as a voltage; the amplifier output is sensitive to changes in detector impedance (capacitance). A charge-sensitive preamplifier on the other hand integrates the detector pulse with the help of a dedicated capacitor, and is insensitive to the variations in detector capacitance. Both of the above preamplifiers types are commonly used in gamma-ray spectroscopy, but discussions here shall be limited to the use of a charge-sensitive preamplifier. The amplified signal is followed by a shaping amplifier, which (as the name suggests) provides the amplified signal with a well-defined shape. Apart from providing additional gain, the shaping amplifier decreases the resolving time for the pulse, and also improves SNR by band-limiting the signal. So to summarize, the signal detection & processing chain in a scintillation detector typically consists of

the detector, followed by a preamplifier, a shaping amplifier, and finally the analog-to-digital convertor (ADC), which digitizes and stores the pulse information.

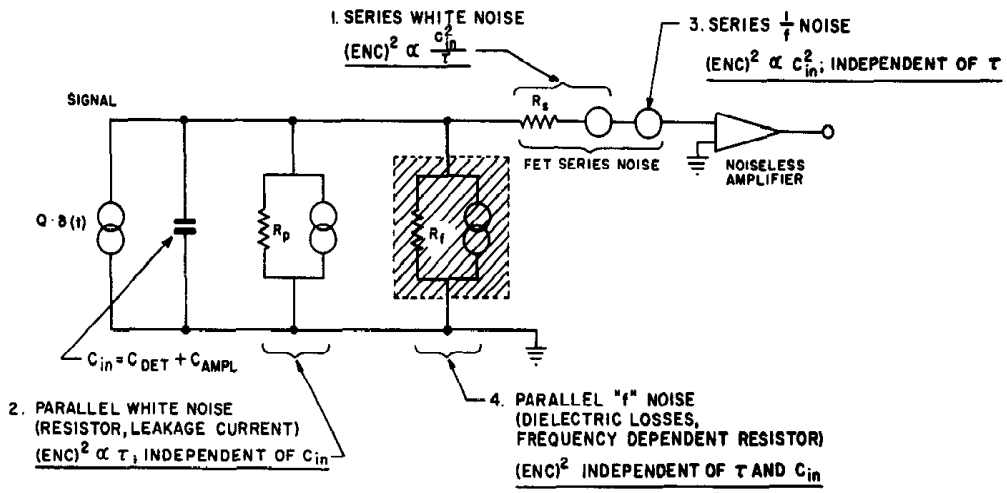

Figure 4.1. Basic noise sources in a detector-amplifier circuit. Figure reproduced from [138].

Ideally, the preamplifier-shaper should introduce very little noise, but in reality, the detector-amplifier combination has definite noise-contributions arising from various sources (Figure 4.1). As described in [138], the total noise in a detector-preamplifier circuit (as an equivalent noise charge) can be expressed by:

$$ENC^2 = A_1 \frac{1}{\tau_p} \frac{4kT}{g_m} (C_g + C_{DET})^2 + A_3 \frac{K_F}{C_G} (C_G + C_{DET})^2 + A_2 \tau_p 2q(I_{DET} + I_{RST}) \quad (4.1)$$

where:

C_{DET} represents the detector capacitance; A_1, A_2, and A_3 are coefficients, which depend on the type of the shaping amplifier [139]; τ_p is the output

pulse peaking time (0 – 100% rise time); g_m represents the transconductance for the input device; and K_F is the 1/f noise coefficient.

The total electronic noise can be decomposed to consist of:

a. Series noise - the first term on the right hand side of equation 4.1,
b. 1/f noise – the middle term on the right hand side of equation 4.1 and,
c. Parallel noise – the last term on the right hand side of equation 4.1.

The total ENC being expressed as the quadratic sum of the series, parallel, and 1/f contributions.

4.1.2 Improving ENC from front-end electronics

As discussed above, the total equivalent noise charge in the circuit is dependent on the relative contributions arising from the series noise, the parallel noise, and the 1/f noise. Also, the total ENC is said to depend on the following factors:

1. Noise parameters of the front-end device (specifically, g_m and C_{GS} for a JFET).
2. Shot noise arising from detector leakage current.
3. Parallel noise arising from the feedback resistor and any other resistor in series with the detector.
4. Series noise arising from the total capacitance seen at the input.
5. Peaking time of the shaping amplifier.
6. 1/f noise contributions (FET, dielectric).
7. Temperature.

Contributions from some of the above factors were carefully investigated, with an emphasis on achieving a lower overall ENC by minimizing the series and parallel noise contributions.

4.1.2.1 Careful evaluation of the test capacitance

To measure ENC, a calibrated charge is injected via a test capacitor located at the input of the preamplifier. The IO-446 was designed to have a dedicated test capacitor having a nominal value of either, 1 or 5 pF. But, since the capacitance is directly integrated onto the substrate (for both BNL designed preamplifiers, IO-446 and IO-354), process variations produce deviations from the intended design value. A careful evaluation is therefore necessary to accurately quantify the ENC.

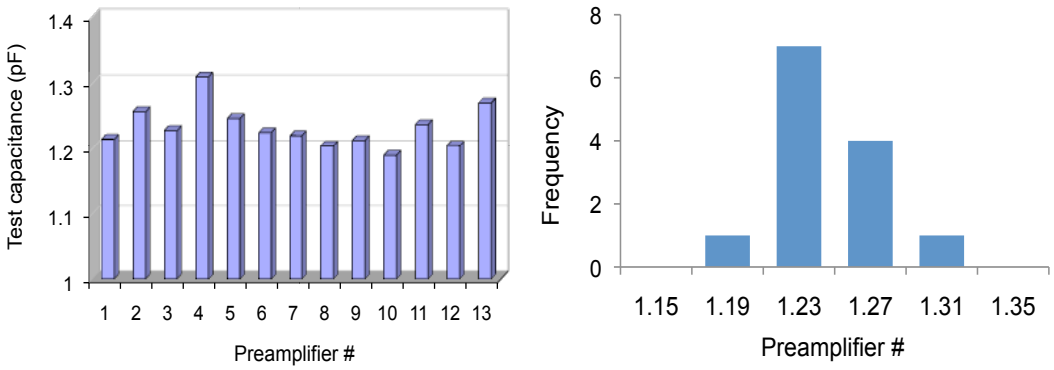

Figure 4.2. Evaluating the test capacitance on the BNL-slow preamplifier: *Left*: A precision LCR meter was used to measure the test capacitor on numerous BNL-slow preamplifiers (nominally 1 pF). *Right*: A histogram of the measured capacitance.

An accurate measurement of the test capacitor on the IO-446 preamplifier was performed with the help of an Agilent-4275A multi-frequency LCR meter (Agilent Technologies, Santa Clara, CA). The test capacitors on thirteen individual IO-446 preamplifiers were evaluated, and measurements revealed a test capacitance of ~1.2 pF (Figure 4.2).

4.1.2.2 Detector-preamplifier matching

Any capacitance at the input of the preamplifier directly affects series noise. As explained by [138], a minimum series noise is attained when the

capacitance of the detector and the front-end device are matched. Given the large capacitance of the RMD APD (~50 pF), the existing input device (SNJ-132L06) did not match well to provide the theoretical minimum. Hence, to better match the device, the input device on the BNL-slow preamplifier (IO-446) was replaced with two Sanyo 2394 transistors (Rescia, S., personal communication).

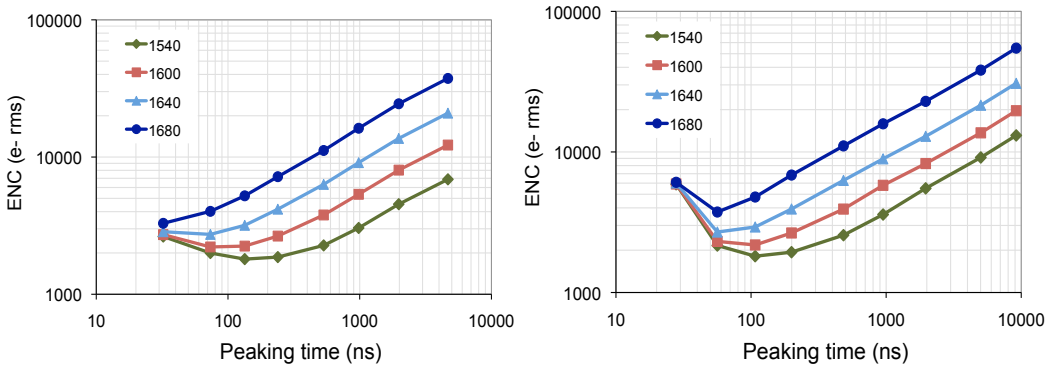

Figure 4.3. Detector-preamplifier matching: In order to provide a better match between the detector and preamplifier, the input transistor on the slow-BNL preamplifier was modified. *Left*: Original BNL-slow preamplifier. *Right*: Modified BNL-slow preamplifier. Note: As expected, no improvements in the parallel noise contributions were seen.

As shown (Figure 4.3), a better matching between the detector and preamplifier reduced the series noise. Also, only a marginal reduction in the overall noise was observed, confirming the overall dominance arising from the parallel noise contributions.

4.1.2.3 Determining the Optimal shaping time

Various factors determining the shaping time of the detector include:

a. Charge collection time (decay time incase of a scintillation detector).
b. Desired gamma-ray timing.
c. Count rate specification.

d. Signal bandwidth.

From an ENC perspective (equation 4.1), the following observations can be made:

- Series noise decreases monotonically with the shaping time,
- 1/f noise is independent of the shaping time, and
- Parallel noise increases monotonically with the shaping time.

Since the total ENC is a quadratic sum of the series, parallel, and 1/f contributions, there must exist an optimal shaping time, which provides the lowest total electronic noise (Figure 4.4).

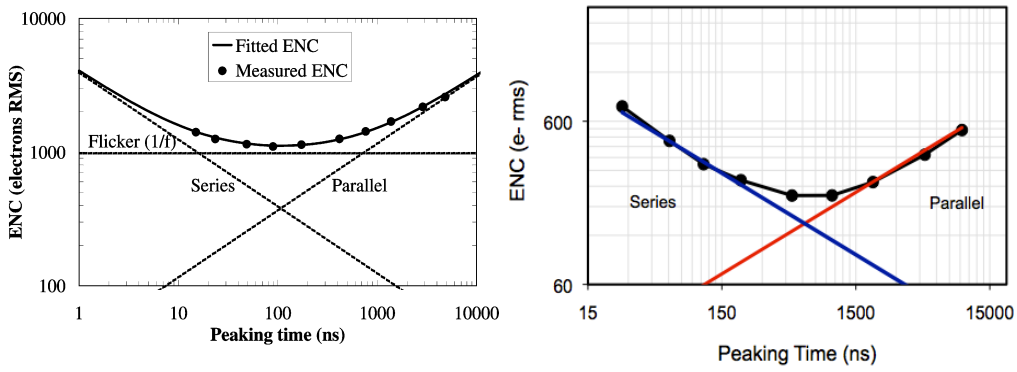

Figure 4.4. Equivalent noise charge (ENC) as a function of the shaping time: *Left*: Demonstration of how the total ENC is linked to the shaping time constant [140]. *Right*: Attestation with a single RMD APD, and a shaping amplifier offering selectable shaping time.

To experimentally determine the optimal shaping time for the RMD APD, a single APD was biased and connected to the preamplifier. The amplified output was then fed onto a second-order semi-Gaussian shaper offering variable shaping time. Since the parallel noise is very much dependent on the leakage current, the measurements were performed for a range of bias voltages (Figure 4.5).

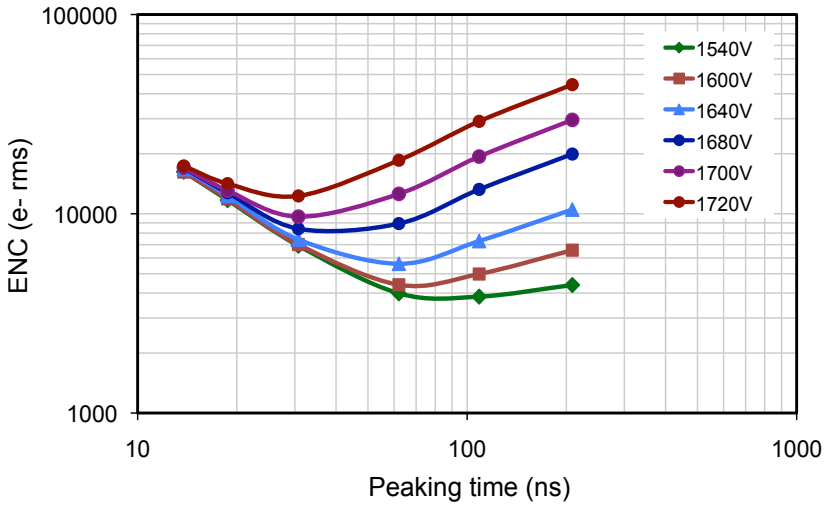

Figure 4.5. Measuring the optimal shaping time for the RMD APD: Total ENC measured for a single RMD APD readout with a shaping amplifier offering variable shaping time.

The measurements were fairly consistent with a theoretical calculation of the "noise corner time constant" [138], which predicted an optimal shaping time of ~100 ns (for a leakage current of ~1 μA). Considering both, the detector requirements (LSO decay time of ~40 ns) and minimizing electronic noise, a ~70 ns shaping-amplifier was a reasonable choice.

4.1.2.4 Optimizing the series resistance

In addition to shot noise from the detector, the front-end also sees parallel noise contributions arising from: the feedback resistor (10 MΩ in this case), and any other resistance connected in series with the APD. In order to reduce the parallel noise contributions, the equivalent parallel resistance should be as high as possible.

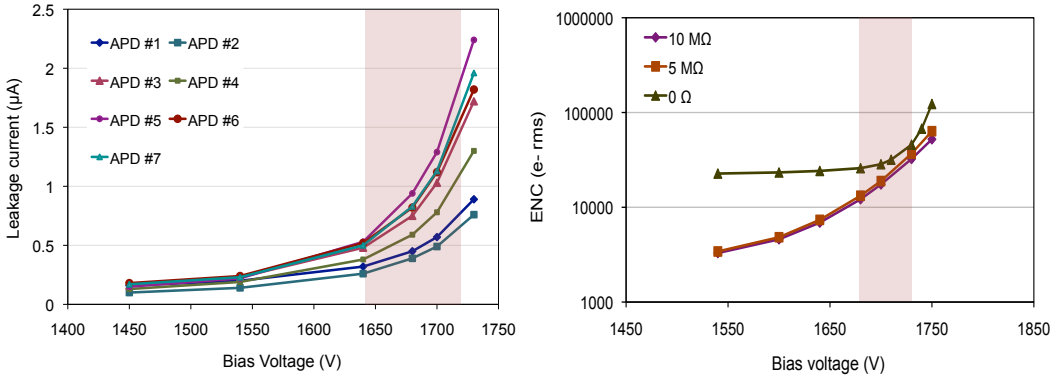

Figure 4.6. *Left*: Leakage current variation among RMD APDs. *Right*: An appropriate current limiting resistor was needed to limit the voltage drop and electronic noise arising from the series resistor. Shaded region indicates the range over which detector normally operates.

There were significant variations in leakage current among the APDs (Figure 4.6). While a large series resistor could possibly be used, its use exaggerated the gain-variations among the APDs (increased series voltage drop; affecting bias voltage). This was important considering all APDs on the initial prototype were operated with a single bias voltage. Hence, a careful evaluation of the trade-off in electronic noise, and series voltage drop was performed (Figure 4.6). Since, the total noise contribution depends on both the feedback, and series resistors, a 5 MΩ resistor was deemed to be a reasonable compromise between minimizing the series voltage drop and maintaining a low ENC.

4.1.2.5 Improving electromagnetic shielding

As stated earlier, electronic noise from the front-ends was found to be the most dominant source of noise in the experimental setup. Additional noise, in the form of electromagnetic/radio frequency interference was also found to be present. Thus various sources of pick-up noise were carefully investigated and eliminated by following good practices for shielding,

grounding, filtering and making use of coaxial cables. While none of the above is discussed here, a detailed explanation for reducing electromagnetic interference can be found in [141]. Subsequently, instead of only the multichannel preamplifier-shaper box residing inside an aluminum box, the entire detector was placed inside a metal box, which acted as a light-tight box, cum faraday shield (see Figure 5.10).

4.1.3 Determining the Optimal Readout Electronics

The main motivation for performing the electronic noise optimizations was to seek affordable, ready-made front-end electronics with reasonable ENC, for building a fully working prototype detector. The detailed noise optimizations performed in the preceding section (Chapter 4.1.2) revealed several necessary modifications, and a redesign of the multichannel preamplifier-shaper box. Since a redesign was necessary, it was decided to thoroughly evaluate the suitability of various, BNL designed as well as other commercially available hybrid preamplifier-shaper combinations. Subsequently, the following preamplifiers were tested:

a. BNL - fast preamplifier (IO-354).
b. BNL - slow preamplifiers (IO446, and its modified version).
c. Commercial – Cremat preamplifier (CR – 110).
d. Commercial – eV preamplifier (eV – 5093).

For performing the noise measurements, a single RMD APD was individually biased and connected to the front-end of each of the above listed preamplifiers. Custom test-boards to house, power-on, and readout the preamplifier-shaper combinations were made. Since the optimal shaping time was determined previously, each preamplifier was followed by a BNL

designed, ~70 ns shaping-amplifier (IO-708). As discussed earlier, ENC was measured by injecting a fixed amount of charge (model DG-535; pulse generator from Stanford Research system, Sunnyvale, CA) onto a test input on the preamplifier. The total rms noise was measured with the help of a fast digital sampling oscilloscope (TDS7254B; Tektronix, Beaverton, OR;). If the preamplifier did not have a dedicated calibration capacitor, an accurately characterized capacitor (~1 pF) was fixed onto the test circuit. Since the ENC varies with the leakage current, the measurements (Figure 4.7) were performed for a range of bias voltages (1540 – 1730 V). For a fair comparison, the same APD was used for all the measurements.

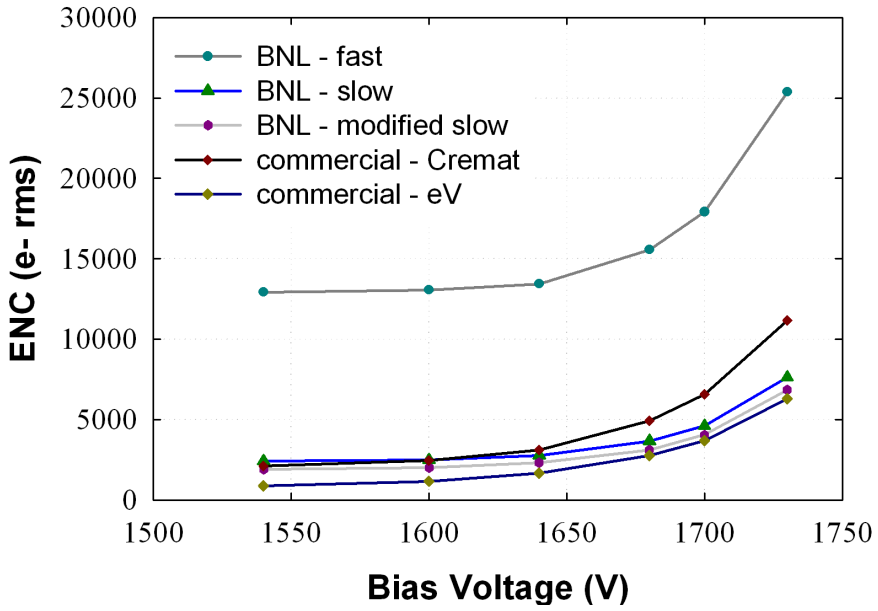

Figure 4.7. Summary of total equivalent noise charge measured with a single RMD APD and several readymade preamplifier-shaper combinations. The measurements were performed at room temperature and at near optimal shaping times.

4.2 Signal-to-Noise Ratio Optimization

Font-end electronics with the lowest possible electronic noise is desirable in a light-sharing detector because, electronic noise directly affects spatial resolution. However, in addition to the electronic noise, there are other factors affecting spatial resolution, and overall performance of the detector. Estimating a measure of the signal-to-noise ratio is an efficient way to evaluate the impact of the various noise sources in the detector. Apart from electronic noise, other noise sources in an APD-based scintillation detector include:

1. The statistical fluctuation in the total number of photons (i.e. photostatistics) measured by the photosensor: Typically, the number of photons reaching a photosensor depends on scintillator non-proportionality and decay time, detector light collection efficiency, and shaping time of the front-end electronics. Additionally, in case of a continuous scintillator, the number of photons reaching a photosensor strongly varies, depending on the depth at which the gamma ray interacts. Figure 4.8 shows one such light-spread function for a normally incident 662 keV ^{137}Cs beam interacting at depths of 1, 4, 7, and 10 mm respectively.

$$excess\ noise = gain \times k_{eff} + \left(2 - \frac{1}{gain}\right)\left(1 - k_{eff}\right) \tag{4.2}$$

2. As opposed to a PIN diode, which has unity gain, an APD provides intrinsic gain through an internal avalanche mechanism. The avalanche mechanism in itself has fluctuations, and poses an additional noise

source. The statistical fluctuations in APD gain is called the excess noise, and it depends on both the APD gain and ionization coefficient (k_{eff}) for the APD (equation 4.2). Note that temperature variations (if any) are a separate cause for gain variations and also need to be considered.

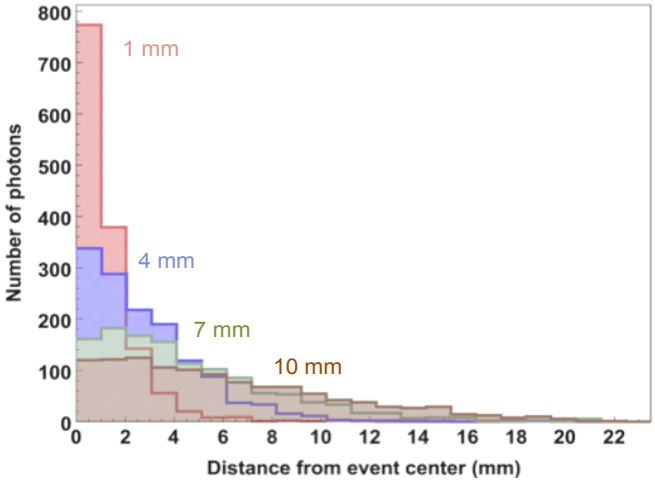

Figure 4.8. Light spread function for a ^{137}Cs beam incident at the center of the 10 mm thick continuous scintillator detector. The number of photons reaching each APD varies significantly, and depends on how far and deep the gamma ray interacts in the scintillator. (Data obtained by performing Monte Carlo simulations using GATE software)

If the peaking time of the shaping amplifier were sufficiently large compared to the decay time of the scintillator, the final signal would purely depend on the number of photoelectrons (N_{pe}) and APD gain. The total noise can be expressed as a quadratic sum of the electronic noise and the APD excess noise (equation 4.3). The signal-to-noise ratio can then be computed by equation 4.4.

$$Total\ noise = \sqrt{ENC^2 + gain^2 \times N_{pe} \times excess\ noise} \tag{4.3}$$

$$signal\ to\ noise\ ratio = \frac{(gain \times N_{pe})}{\sqrt{ENC^2 + gain^2 \times N_{pe} \times excess\ noise}} \tag{4.4}$$

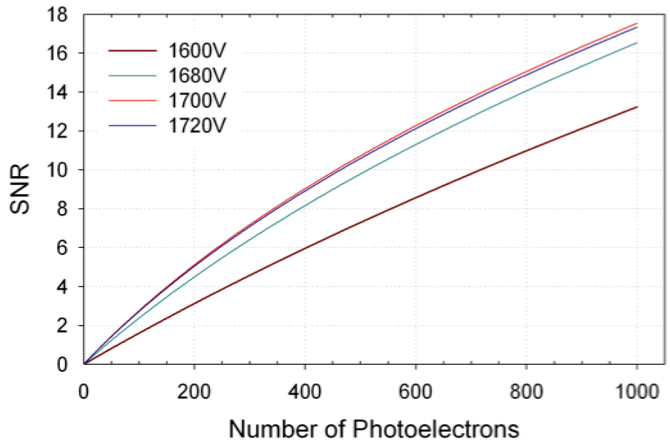

Figure 4.9. Estimating the optimal bias voltage, and signal-to-noise ratio for the RMD APD: Measured estimates for electronic noise, and APD gain were included in the SNR calculation. Since the number of optical photons reaching each APD varies appreciably, the SNR was estimated for a range of photons.

Figure 4.9 shows the estimated SNR for a single RMD APD. Since the SNR varies with bias voltage, it was estimated for various operating bias voltages. An accurate knowledge of the ionization coefficient (k_{eff} = 0.0004) was combined with measured estimates for the APD gain, and electronic noise. Since the number of photons reaching the APD covers a broad dynamic range, the SNR was computed over the range of expected photons.

A theoretical expression to estimate SNR for the APD had been devised above. If validated, it would be a useful tool to determine the optimal bias voltage for various detector configurations. To experimentally measure and validate the SNR expression, a single, Teflon wrapped 2 x 2 x 18 mm^3 LSO crystal was coupled and mounted onto a single RMD APD. The single crystal

was expected to serve as a calibrated light source. Based on previous experiences with the RatCAP crystals, a 2 x 2 x 18 mm^3 LSO crystal provides ~2000 photons/MeV. The APD was read-out with the help of a charge-sensitive preamplifier, and an Ortec shaping amplifier (Model 454; Advanced Measurement Technologies, Oak Ridge, TN). The amplified, and shaped signal was finally digitized with a peak-sensing ADC (model V785, CAEN Technologies, Italy). The trigger and delay signals were generated with the help of standard NIM electronics. To help estimate SNR, a 511 keV ^{68}Ge source was placed on the detector and its energy resolution was measured. To determine the optimal bias point, the measurement was performed over the 1540 – 1800 V range. The energy resolution (indicative of SNR) appeared to plateau at a bias voltage of ~1700V (Figure 4.10), very similar to what the calculations had predicted earlier (Figure 4.9).

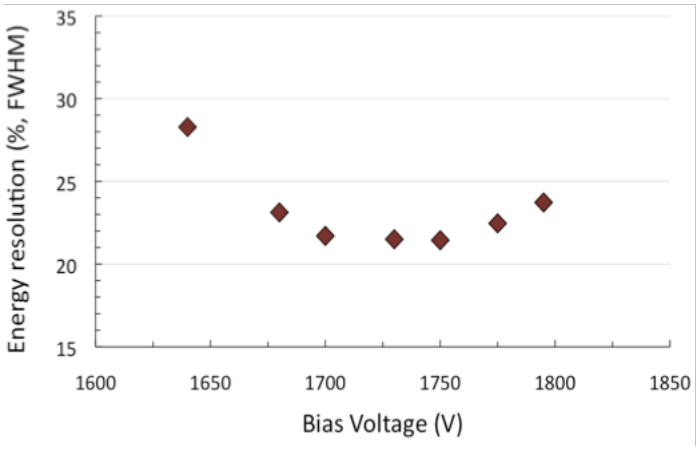

Figure 4.10. Experimentally optimizing signal-to-noise ratio for the RMD APD: Energy resolution was measured with a single Teflon wrapped 2 x 2 x 18 mm^3 LSO crystal mounted on the APD. As expected (see Figure 4.9), the signal-to-noise starts to plateau at a bias voltage of ~1700 V.

4.2.1 Detector Cooling

The optimizations (ENC and SNR) discussed in the above sections were implemented on the two-APD version of the initial prototype detector (discussed in Chapter 3). Since no major gains were observed upon characterization, it was not clear if further improvements were necessary before proceeding with implementing a fully instrumented detector. Hence, alternative-ways to increase APD SNR were also explored.

While choosing an optimal bias voltage is one method to optimize the APD SNR, another common technique to improve SNR is by cooling the detector. Cooling the APD decreases the thermal energy of the electrons, thereby decreasing the dark current and the corresponding shot noise arising from it. Further, a lower temperature increases the avalanche efficiency [142, 143], increasing the APD gain. While detector cooling is common and has been used by numerous researchers [86, 144, 145], it brings with it the added complexity of designing and maintaining a dedicated cooling system. Besides, it also makes the detector less compact. Nevertheless, it is an attractive option in detectors where the electronic noise is dominated by shot noise. While optimizing the electronic noise is a more elegant solution (performed first, and discussed in section 4.1), the large dark current in the existing detector prompted to evaluate the benefits of cooling the detector.

A single RMD APD was individually biased and readout with an optimized BNL-slow preamplifier-shaper combination. Initially, the detector was placed inside a customized, small-volume, polystyrene box and was surrounded with dry ice. Dry nitrogen gas was pumped to eliminate humidity and condensation related issues. While the above setup successfully cooled the APD down to ~10 °C, it became increasingly difficult to eliminate

condensation related issues without complicating the setup. Also, a more systematic study of the benefits of cooling seemed more valuable.

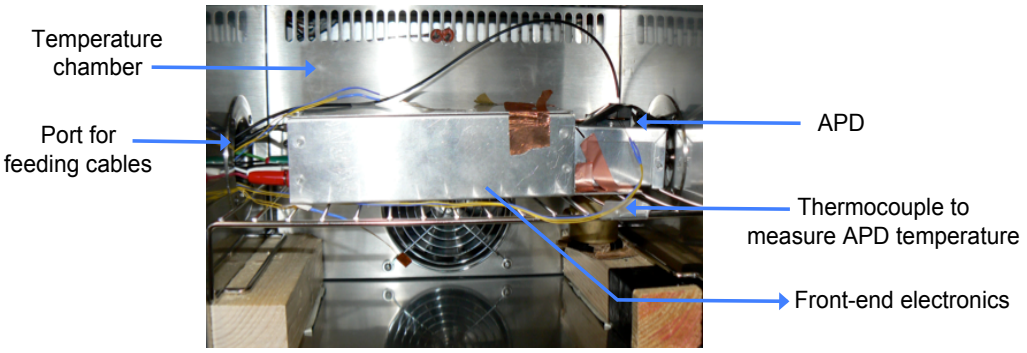

Figure 4.11. Setup used to measure the benefits of cooling the RMD APDs. A single APD and its associated front-end electronics were placed inside the TestEquity temperature chamber.

Further studies were performed with a TestEquity temperature chamber (model 105A; TestEquity, Moorpark, CA). The temperature chamber is compact (volume of ~0.5 ft^3), light-tight, and conveniently allows accurate control of temperature over a wide range (-40 °C to 130 °C). The chamber also has 3" access ports to feed the necessary power and readout cables with minimal fuss. Detector temperature was determined with the help of multiple resistive thermal devices (i.e. RTDs; Minco, Minneapolis, MN) placed inside the chamber volume, and read-out by a single temperature monitor (model 218; Lake Shore Cryotronics Inc., Westerville, OH). Dry nitrogen gas was pumped through the chamber volume to eliminate any possible condensation. As before, a single RMD APD was biased and read-out with the optimized BNL-slow preamplifier-shaper combination. Dark current, gain, and electronic noise were measured for a range of temperatures (-2.5 °C to 27.5 °C). Dark current was measured (Figure 4.12) by measuring the current drawn by a 10 MΩ resistor connected in series with the APD. The APD gain

was measured by piping light from a 400 nm LED (operated in pulsed mode) onto the APD surface. The equivalent noise charge was measured (Figure 4.13) by injecting a fixed amount of charge via a test capacitor located on the preamplifier input.

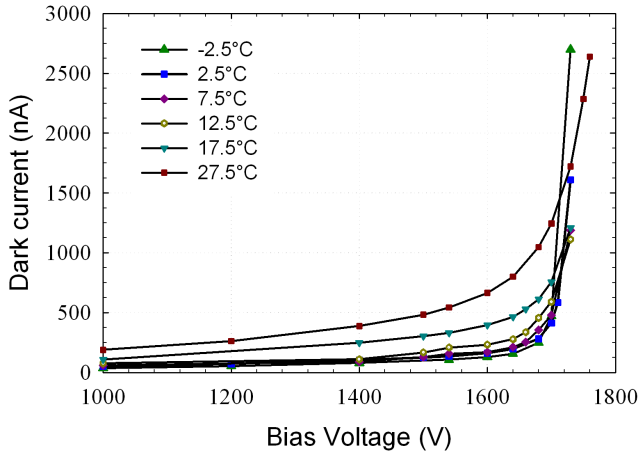

Figure 4.12. Dark current for a single RMD APD, measured as a function of its bias voltage and detector temperature (-2.5 to 27.5 °C range). As expected, the leakage current at 1680 V dropped from ~1 μA at room temperature to ~300 nA at 2.5 °C.

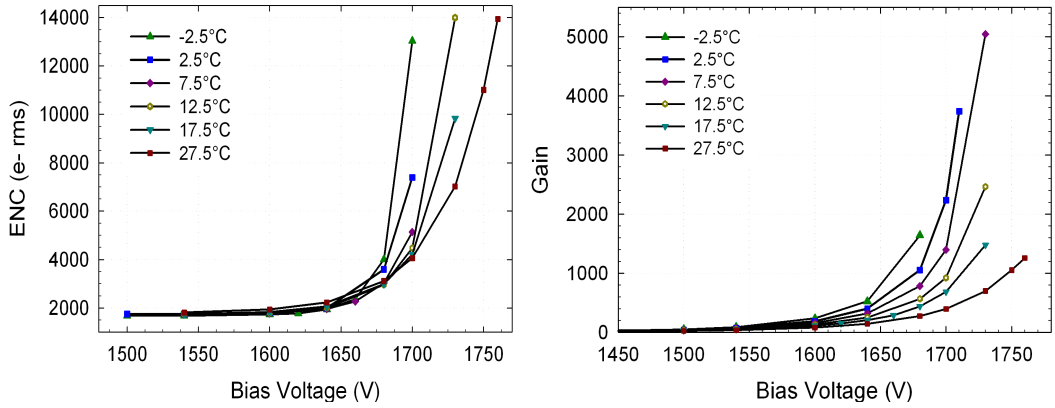

Figure 4.13. Equivalent noise charge (*left*) and gain (*right*) measured for a single RMD readout with an optimized BNL preamplifier-shaper combination. The measurements were carried over the -2.5 to 27.5 °C temperature range.

The benefits of cooling the detector can be analyzed as follows: At room temperature (27.5 °C), a gain of ~1000 is achieved at 1750 V. For a similar gain at 2.5 °C, the APD is biased at 1680 V. As expected, the electronic noise at 2.5 °C is considerably lower than that at room temperature (~4000 e- rms versus ~14000 e- rms).

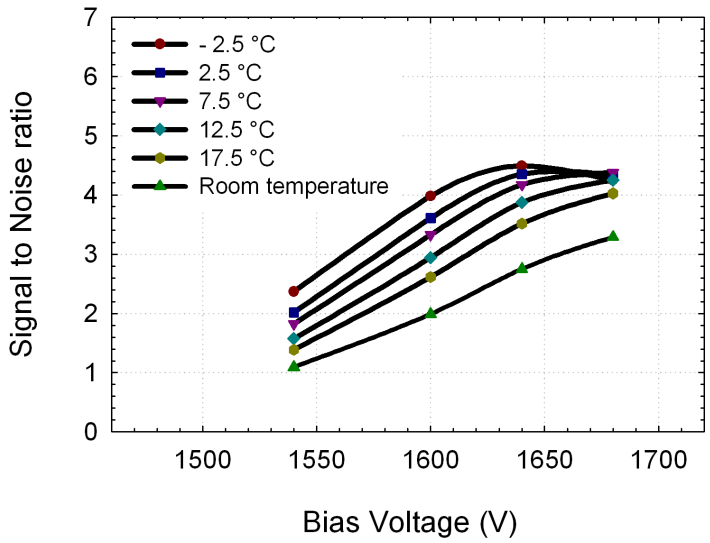

Figure 4.14. Signal-to-noise ratio for the RMD APD as a function of temperature: Cooling the detector to -2.5 °C doubles the signal-to-noise ratio at 1600 V.

The SNR (as a function of temperature) better summarizes the benefits of cooling the detector (cumulative effect of measuring dark current, gain and equivalent noise charge). As demonstrated by Figure 4.14, at a bias voltage of 1600 V, cooling the detector to -2.5 °C doubled the SNR.

4.3 Newly Developed solid-state Photosensors

Slowly but surely, solid-state photosensors are gaining popularity, and the technology is maturing. During this project, a few more large-area APDs

became commercially available. While these APDs could not provide high gains, they offered low leakage current and improved quantum efficiency, equally important to the success of this design. With limited number of APDs to choose from, the RMD APD seemed appealing due to its gain, size and was used to build the initial prototype. Now, with more options to choose from, it was logical that they be carefully studied in terms of their appropriateness for this design. More specifically, studies examined in detail, gain, quantum efficiency, and electronic noise properties for the following APDs:

1. S8664 series of APDs from Hamamatsu
2. Large-area APDs from PerkinElmer (specifically, C30739ECERH)

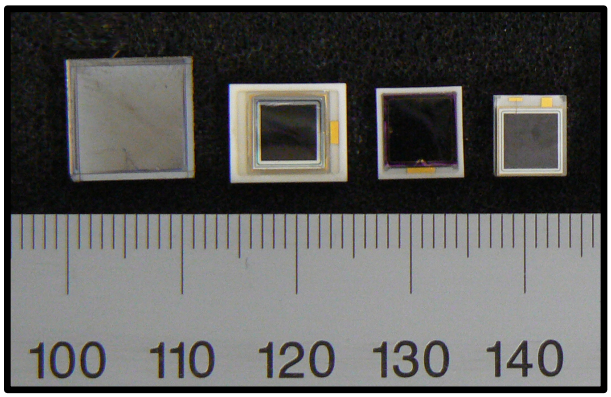

Figure 4.15. Newer, large-area APDs: Pictured are some of the newer large-area APDs from Hamamatsu and Perkin Elmer. While the newer APDs could not achieve the high gains achieved by the RMD APD, they had significantly lower dark current and better quantum efficiency. For sake of comparison, the RMD APD (extreme left) is also shown.

While quantum efficiency and gain measurements were also performed, they agreed very well with quoted specifications. Hence only the noise measurements and optimizations performed with these APDs are discussed below.

4.3.1 S8664 series APDs

The S8664 series APDs from Hamamatsu APDs are "reverse-type" APDs, optimized for use in the UV – visible light spectrum. They are available in two different sizes i.e. with active-areas of 5 x 5 mm^2 and 10 x 10 mm^2. They have very good quantum efficiency (~75% at 420 nm), very low leakage current (< 10 nA), and moderate capacitance (80 pF for the 25 mm^2 device and 270 pF for the 100 mm^2 device). On the downside, they have moderate gain (<250) and poor packing fraction (~25 % for the 25 mm^2 device, and ~50% for the 100 mm^2 device).

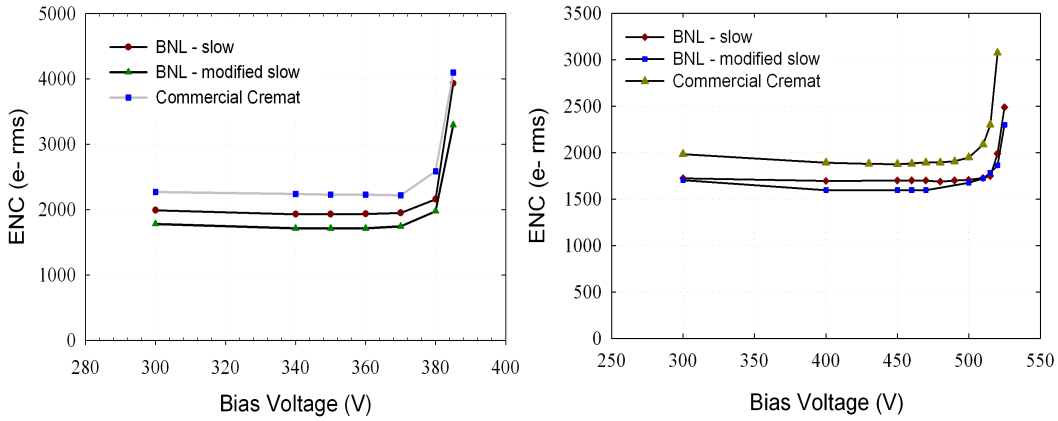

Figure 4.16. Optimizing total electronic noise for a 5 x 5 mm^2 active-area APD from Hamamatsu (*left*). Electronic noise was also optimized for an improved specimen of the 5 x 5 mm^2 Hamamatsu APD (*right*). The improved version had ~30% lower capacitance when compared with the original APD.

To measure the noise performance, a single device was seated on a custom circuit board, biased, and readout by various preamplifiers (BNL designed and commercially available). The BNL designed IO-708 shaping-amplifier was used for all the measurements. As before, ENC was measured by injecting a fixed amount of charge via a calibration input on the amplifier (Figure 4.16).

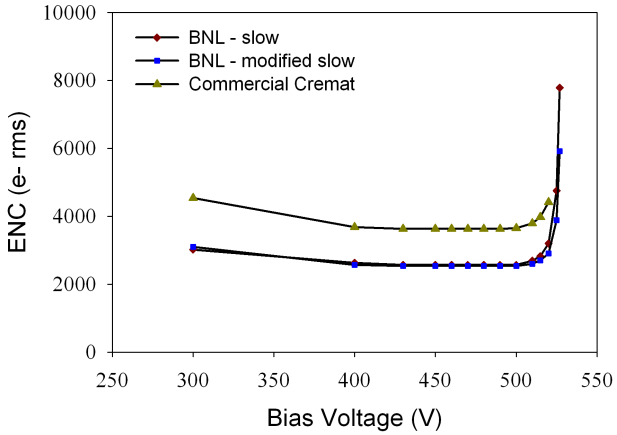

Figure 4.17. Optimizing total electronic noise for an improved specimen of a 10 x 10 mm^2 active-area APD from Hamamatsu.

More recently, Hamamatsu had developed improved versions (not yet commercially available) for both, the 25 mm^2 and the 100 mm^2 APDs. These improved APDs had higher breakdown voltages, and lower capacitance. The noise performances of the improved version were also characterized (Figure 4.16 for the 25 mm^2, and Figure 4.17 for the 100 mm^2). As expected, the lower capacitance APDs provided slightly better noise performance.

4.3.2 S8550 APDs

The Hamamatsu S8550 is a 4 x 8 array of 1.6 x 1.6 mm^2 APDs. They are designed to operate in the UV – visible light region, and have an internal structure similar to the S8664 family. On account of their small size, they have a pixel capacitance of ~10 pF, and leakage current < 10 nA. While a few groups have successfully tried the S8550 to read a continuous scintillator, the small active area necessitates an increase in the number of readout channels (added costs and complexity). But, based on the positive experiences with

using the S8550 for the RatCAP detector, it was decided to evaluate their noise performance when readout by the above hybrid preamplifiers.

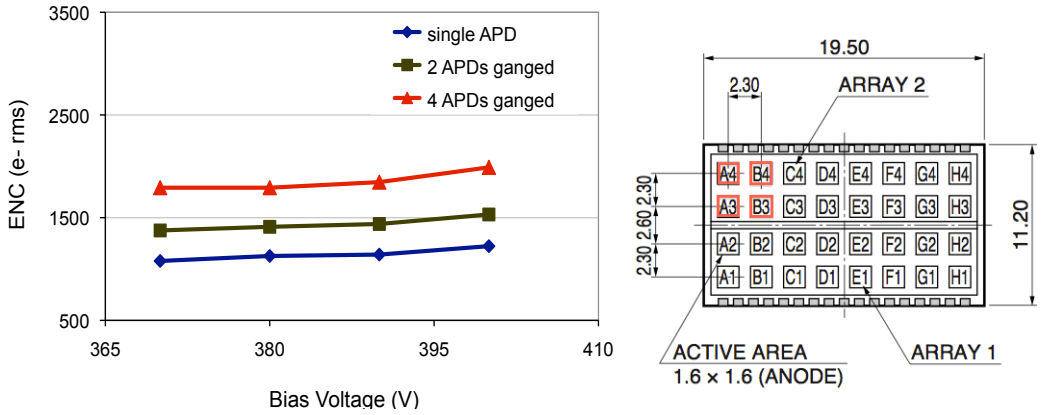

Figure 4.18. *Left*: Electronic noise measured with the RatCAP APD array readout by a BNL designed slow preamplifier. Since the individual pixels on the array measured 1.6 mm^2, we also investigated ganging multiple pixels (1, 2 or 4) to increase SNR while maintaining a lower number of readout channels. *Right*: APD array, with an illustration of how individual pixels on the array were ganged (red).

A single S8550 was plugged into the IO-1043 board (APD-preamplifier readout board), previously designed for the RatCAP scanner. One single APD pixel on the array was readout by a BNL slow preamplifier-shaper combination. The shaping time for the APD was not optimized. As explained earlier, ENC was measured by injecting a calibrated charge into the preamplifier input.

Since the spatial resolution in this design is primarily dependent on the light-spread function, one could potentially couple the S8550 with a thinner scintillator, and get much better resolution. The detector could then be layered to compensate for the decrease in sensitivity. Alternatively, multiple pixels on a single device could be ganged together, to create a pseudo-large-area APD (Figure 4.18, right). To test this effectiveness, 2 and 4 individual

pixels were grouped together and read out with the same preamplifier-shaper combination used to readout a single APD pixel. Since the noise is directly related to the bias voltage, all the above measurements were performed for a range of bias voltages (Figure 4.18, left).

4.3.3 PerkinElmer APDs

PerkinElmer has recently made excellent progress in the development of new, fast, low noise APDs [146, 147]. One among them, the C30739ECERH, is a large-area APD (active area of 5.6 x 5.6 mm^2; ~50% active area) optimized for use in the 400 – 700 nm range (~75% quantum efficiency at 420 nm). While the manufacturer is still optimizing the APD design, it has been specifically intended for low-noise applications. It has low capacitance (~60 pF), and also low leakage current (< 10 nA).

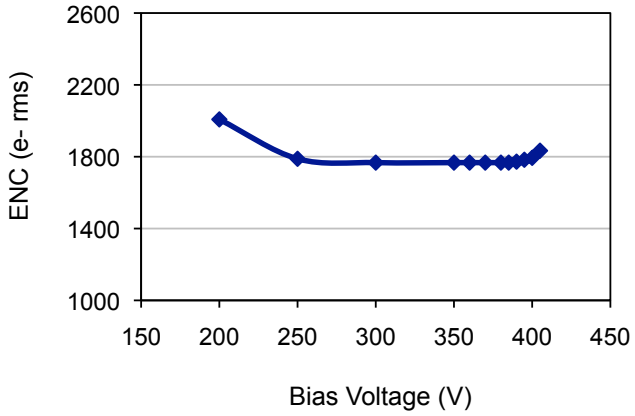

Figure 4.19. Equivalent noise charge measurement with a 5.6 x 5.6 mm^2 PerkinElmer APD readout by a BNL designed slow preamplifier.

While the APD offers low-noise (Figure 4.19), good packing fraction, and high quantum efficiency, the APD can only achieve a limited gain of ~100. That being said, the manufacturer is actively working on improving gain for these

APDs (while maintaining low noise). The C30739ECERH could be an excellent choice for building an improved detector.

4.3.4 Silicon Photomultiplier

The Silicon Photomultiplier (SiPM, aka MPPC) is a new type of photosensor consisting of multiple tiny APDs operating in Geiger mode. The output of the SiPM consists of a sum of all the individual APD pixels. While retaining the benefits of a solid-state device, SiPMs also possess some of the excellent characteristics of photomultiplier tubes (i.e. high gain, reasonable quantum efficiency, and very fast timing). Their high intrinsic gain relaxes the need to have low-noise readout electronics, and at the same time also permits resolving very low light levels; both of which are very attractive for this design. Possible drawbacks for the device are the associated dark count rate and the low photon detection efficiency (PDE).

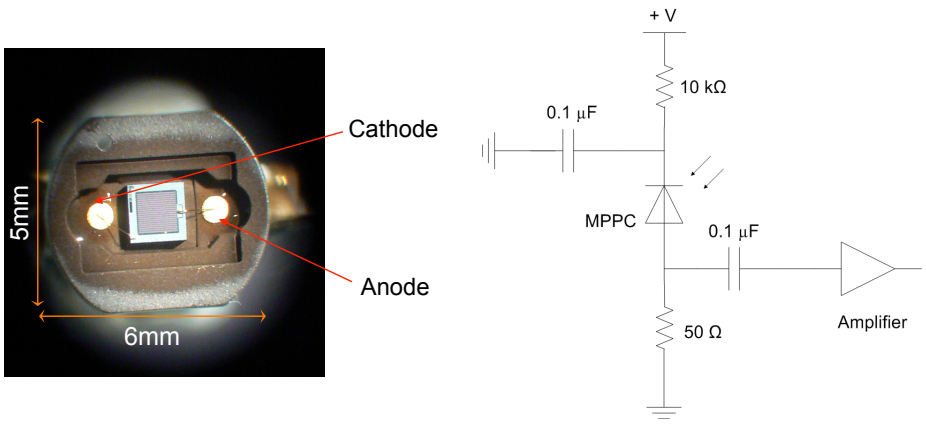

Figure 4.20. Hamamatsu MPPC: *Left*: Photograph of a 1 x 1 mm^2 silicon photomultiplier (aka MPPC) from Hamamatsu. *Right*: Experimental setup to evaluate the Hamamatsu MPPC.

As a starting point, a Hamamatsu 1 x 1 mm^2 SiPM (S10362-11-025C; Hamamatsu Photonics, Japan [148]) was procured. The device (Figure 4.20)

had 1600 APD pixels, each 25 μm^2 in size; gain of 2.75 x 10^5, capacitance of 35 pF, and a peak PDE of 25%. To evaluate its capabilities, the device was biased (~70 V; close to the recommended bias voltage) and read out by a BNL hybrid preamplifier-shaper combination (BNL IO-535 and IO-708). Figure 4.20 illustrates the readout circuit used to evaluate the device. Under completely dark conditions, the intrinsic dark counts can be clearly resolved. Later, the SiPM was illuminated with very low light levels with the help of a 400 nm pulsed-LED (piped onto the SiPM surface via an optical fibre, ~200 μm diameter). A high gain (~10^7) photomultiplier tube (R2059; Hamamatsu Photonics, Japan) was used to calibrate the light-source. As shown (Figure 4.21), the device has an excellent capability in detecting weak light pulses, demonstrating their appropriateness for this design (or even for PET in general).

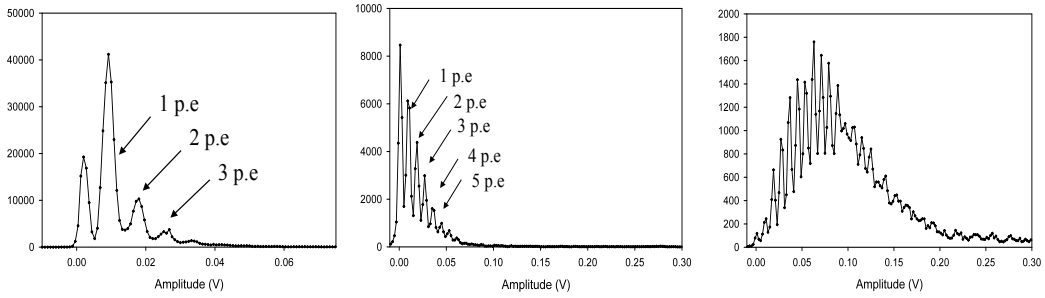

Figure 4.21. Single photoelectron spectra measured with a pulsed low-light-level LED on the 1 x 1 mm^2 Hamamatsu MPPC.

4.4 Fully Monte Carlo Simulations using GATE

First an analytical model, and later a Monte Carlo model using DETECT2000, provided initial estimations for the detector performance. While both the models predicted good detector performance, they were

limited by their inability to model complicated detector geometries. Also, the DETECT2000 package lacked the ability to easily track gamma rays, constraining early evaluations to simplified beam geometries. For the model to be able to simulate and predict performance under realistic experimental conditions, it is important that both of the above (i.e. ability to model actual detector and beam geometries) be addressed.

GATE (Geant4 Application for Emission Tomography; [121, 122]) is a Monte Carlo simulation platform designed by a collaborative effort between numerous research groups from the medical imaging community. It is based on GEANT4 [116, 117, 149], and has been specifically designed to help model, evaluate PET and SPECT systems. The package is very modular (in architecture), and allows the user to simulate and evaluate complex source, detector, and scanner geometries [78, 150, 151] with relative ease. While the package previously lacked the ability to generate and track optical photons, recently, a newer version (v.3.0.0) that included these capabilities has been released. Beyond building and evaluating the detector model, GATE lends itself to evaluating the potential in building a full scanner. Also, the package is well supported, documented, validated, and freely available. On account of all the above reasons, GATE v.3.0.0, was chosen to develop a fully Monte Carlo model for the detector. The GATE model for this detector would account for all the real-world effects, which included:

- Gamma-ray interaction physics
- Scintillator light output
- Scintillator intrinsic resolution
- Surface modeling
- Absorption, reflections and refractions are various material interfaces

To make the model fully Monte Carlo, customized code was written to also account for:

- APD quantum efficiency
- APD gain
- APD excess noise factor
- Front-end electronic noise

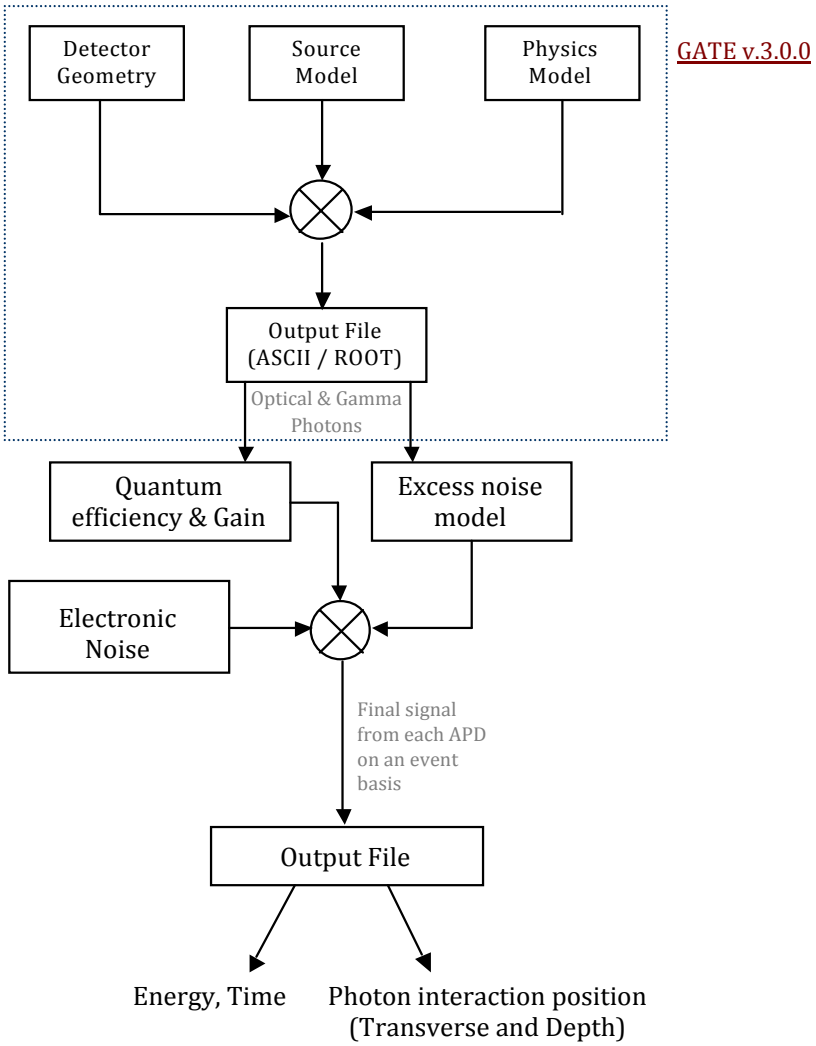

Figure 4.22. Schema of the fully Monte Carlo model built using GATE.

4.4.1 Performance Estimation of a Fully Instrumented Detector

Previously, simplified simulations (analytical, and DETECT2000 models) predicted ~1 mm spatial resolution for fixed-depth photoelectric interactions within the crystal. Experimental characterization of a partially instrumented prototype was encouraging, but far from the 1 mm resolution predicted earlier. Since the immediate goal was to develop a fully instrumented prototype detector, it was logical to evaluate the expected performance with the help of a fully Monte Carlo model. A schematic of the simulation development process (using Gate v3.0.0) is outlined in Figure 4.22.

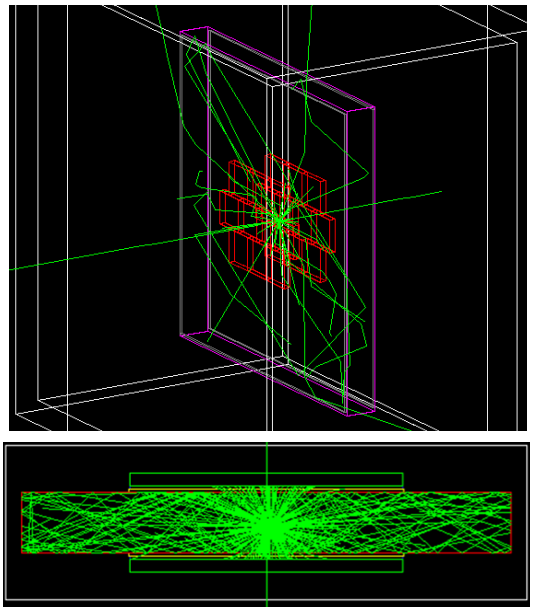

Figure 4.23. Detector model using GATE. *Above*: Snapshot of the detector showing the scintillator and array of APDs on the top and bottom sides. *Below*: Side view of the detector showing the gamma-ray (vertical green ray) and optical photons reflecting through material interfaces (green rays within the scintillator).

The preliminary stage of the simulation involved generating an accurate

model for the prototype detector (Figure 4.23). The scintillator was modeled as a single LSO disk, 1 cm thick and 6 cm in diameter, and coupled to seven large-area APDs (each with an active area of 8 x 8 mm^2) on either side. The long edges of the scintillator were modeled as flat and polished ("POLISH") surfaces, and the short edges were modeled to mimic a black paint applied ("GROUND") to reduce the reflections occurring near the edge of the scintillator. The scintillator was assumed to have a refractive index of 1.82 [131], light yield of 25,000 photons/MeV, and an intrinsic resolution of ~10% FWHM [132]. The crystal-APD interface was modeled as a 0.5 mm thick layer of optical coupling (Sylgard-527, refractive index = 1.41; Dow Corning Corporation, Midland, MI). A 0.001 mm thick layer of glass (refractive index of 1.50; personal communication, RMD) was used to model the surface of the APD. The standard electromagnetic package, which accounts for Compton and photoelectric interactions down to 10 keV was used.

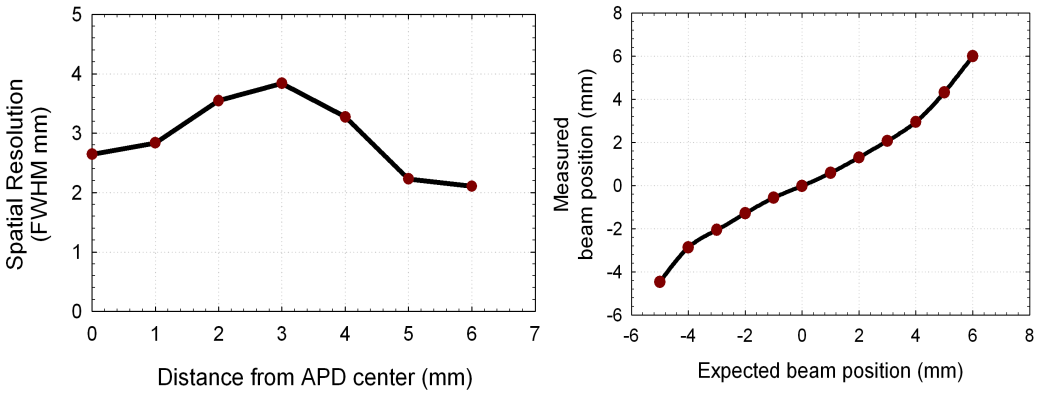

Figure 4.24. *Left*: Transverse spatial resolution for a fully instrumented prototype detector using RMD APDs, estimated using a detailed Monte Carlo model built with the GATE package. *Right*: Expected linearity for the fully instrumented prototype detector.

To estimate the spatial resolution of the detector, a 662 keV, ^{137}Cs gamma-

ray beam was scanned in 1 mm increments along the face of the detector. At each position, ~10,000 gamma rays were generated. Armed with an accurate detector model, GATE tracks each gamma ray as well as each optical photon resulting from the gamma-ray interaction inside the scintillator. The optical photons are tracked until they are either absorbed, escape, or reach the APD surface. The final GATE output consists of the total number of photons arriving at each of the APDs, after taking into account the reflections and refractions occurring both within the scintillator and at the scintillator-APD interface.

The remainder of the simulation was processed with software custom-designed for this project. The number of photons reaching each APD is factored with APD quantum efficiency (52% at 420 nm), APD gain (450), electronic noise (5000 e- rms), and APD excess noise factor (2.8) to obtain an estimate of the final signal from each APD. Traditional Anger logic using all 14 APDs from both sides of the scintillator is used to compute the interaction position. Since the response of the detector is somewhat non-linear (Figure 4.24), a position dependent calibration is used to correct and calculate the spatial resolution (Figure 4.24). Since the output of the simulation is available either as a ROOT or ASCII file, all the data was processed using code written in C/C++. For the above simulations, considering all events (i.e. interacting at different depths and energies i.e. photoelectric and Compton), an average spatial resolution of about 2.9 mm FWHM was estimated.

4.4.2 Verifying Model Parameters

A detailed Monte Carlo model for the detector was built using GATE as described above. Since the first goal was to predict the performance of a fully

instrumented detector, reasonable values were assumed for most detector components. While a Monte Carlo model is a powerful tool to predict detector performance, its real power lies in its ability to perform rapid (and economical) prototyping, and design optimizations. However, for this, a validated model is essential. While validating the model with results from the prototype detector would be ideal (note that a complete detector was yet to be instrumented), a reasonable first step towards developing an accurate model would be to use measured estimates for the various detector parameters. Accurately measuring the detector parameters could also potentially unearth discrepancies between assumptions and reality.

4.4.2.1 Scintillator

Measurements to ascertain the light yield and the optical transparency of the scintillator were performed.

To measure the light output; the entire LSO slab (6 cm diameter) was centered on a 2" PMT (model R2059; Hamamatsu Photonics, Japan) with the help of an optical couplant (Q2-3067; Dow Corning Corporation, Midland, MI). A collimated, 662 keV, ^{137}Cs source was aimed at the center of the scintillator. The PMT output after amplification was sent to a charge integrating ADC, which generated a pulse-height spectrum. To minimize collection of light reflected-off the scintillator surfaces (flat and edge), all other faces of the crystal were covered with an absorbent black paint. An accurate knowledge of the PMT gain, ADC resolution and full-scale range helped calculate the total number of measured photoelectrons. Factoring in the PMT quantum efficiency and the light collection efficiency (arising from the critical angle) provided a measure of the intrinsic light output for the

scintillator. A light output of ~17,500 photons/ MeV was measured for the above LSO scintillator slab.

4.4.2.2 Optical coupling

A thin layer of optical-coupling is applied to effectively channel the light photons from the scintillator to the photosensor. Important properties of the optical coupling include its refractive index and transmittance.

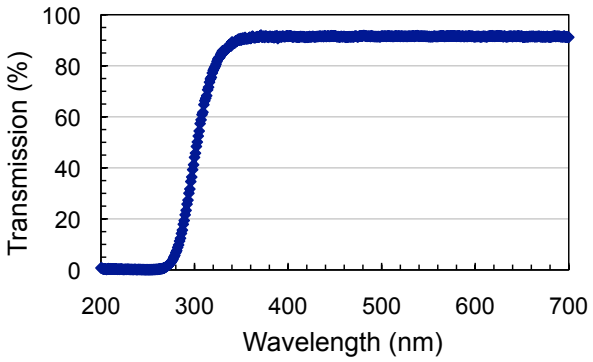

Figure 4.25. Evaluating the optical transmittance for Sylgard-527. Note: The cut-off in the UV region (lower end) is on account of the glass-slide on which the media was mounted.

The transmittance of the optical-couplant was measured with the help of a spectrophotometer (model U-3210; Hitachi High Technologies America Inc, Schaumburg, IL). The U-3210 is a double beam spectrophotometer, capable of accommodating a large sample size, and is equipped with an integrating sphere to maximize collection of the diffuse-reflected light, to accurately measure reflectivity and transmission. It also has tungsten and deuterium lamps to help perform measurements over a range of wavelengths (UV, to beyond visible light). A ~0.2 mm thick sample of Sylgard-527 was cured on a glass-slide and placed in the path of the sample beam. The

spectrophotometer calculates the transmittance by measuring the relative intensity of light from the sample and reference beams. To help normalize their relative intensities, a blank scan is performed before the actual measurement process. As shown in Figure 4.25, Sylgard-527 has excellent transmittance for blue light. The low transmission seen in the UV region is on account of the media (i.e. glass slide) on which Sylgard-527 was mounted.

The same spectrophotometer was also used to measure the transmittance properties of the scintillator slab. For the above slab (10 mm thick, 6 cm diameter), a transmittance slightly better than 90% was measured, and no degradations were observed over the surface area.

4.4.2.3 Photosensor

Important properties for the APD include gain, quantum efficiency, and excess noise. While the gain for the RMD APD had been characterized previously, its quantum efficiency was never measured.

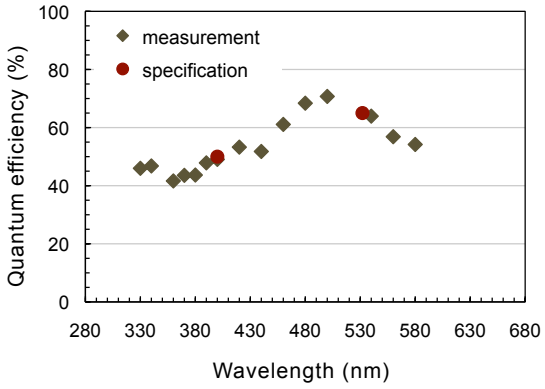

Figure 4.26. Quantum efficiency for the RMD APD.

Quantum efficiency was determined by measuring the APD photocurrent with a well-defined, light-source illuminating the APD. A Xenon arc lamp, and

monochromator (Newport Corporation, Irvine, CA) were used to generate the light source. The filtered light from the lamp was focused into an optical fiber and subsequently radiated onto the surface of the RMD APD. The APD was biased at a low enough voltage (model 487; Keithley Instruments Inc., Cleveland, OH) to ensure minimal or no gain. The Keithley 487 was also used to accurately measure photocurrent from the APD under illumination. To calculate the absolute quantum efficiency, a factory calibrated PIN diode (S1337-1010; Hamamatsu Photonics, Japan) having known quantum efficiency was used as a reference. The quantum efficiency measurement was performed over the 300 – 600 nm range. Quantum efficiency measurements for the RMD APD agree very well with the specifications (~50% at 420 nm; Figure 4.26).

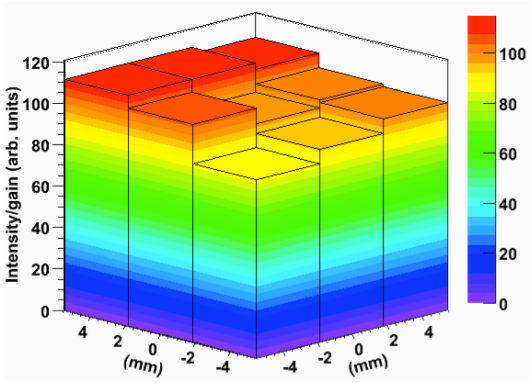

Figure 4.27. Gain variation over the surface of a single RMD APD.

The gain for the RMD APD had been characterized previously. While inter-APD gain variations are very common, with a large active-area, intra-APD gain variations (i.e. gain variation over the surface area of a single APD) were a possible concern, and had not been quantified. A similar setup used to measure gain was used to measure this. A nitrogen laser (337 nm) was

pulsed at approximately 15 Hz and used to excite a plastic scintillator (BC-420; Saint-Gobain Crystals, OH) that emitted fixed light pulses at 420 nm. Light from the plastic-scintillator was coupled to the APD (under bias) via an optical fiber. Instead of fixing the fiber at a single location on the APD surface, the fiber was placed a small distance away and scanned across the face of the APD. To monitor and correct for any possible drifts in the laser output, a second reference detector was also installed. Figure 4.27 shows the gain variation over the surface of the RMD APD.

4.4.2.4 Front-end electronics:

The electronic noise (5000 e- rms) used in the simulations was carried over from the detailed electronic noise optimizations performed previously (Chapter 4.1).

4.4.3 Optimizing Model Parameters

A thorough evaluation of the initial prototype detector helped clarify the shortcomings of the existing detector components. Since the immediate goal was to build a fully instrumented detector, it was important to ascertain if these shortcomings could be addressed. While the noise performance of select newly available photosensors were already evaluated (Chapter 4.3), a detailed study for the remaining detector components was also performed.

4.4.3.1 Scintillator

The scintillation yield for an LSO scintillator should ideally be close to 30,000 photons/MeV [152, 153]. The measured yield was significantly lower. To address this, the original scintillation crystal (i.e. slab) could be replaced with a new crystal having a yield closer to the expected 30,000 photons/MeV.

Alternatively, a newer scintillator like $LaBr_3$ (even faster and brighter than LSO) could be used. In addition to choosing the correct scintillator type, selecting an appropriate scintillator thickness is another important criterion, which determines the spatial resolution of the detector (see chapter 7 for more details).

4.4.3.2 Optical coupling

The performance of a light-sharing detector is intrinsically related to its light spread function. While minimizing and maintaining the light-spread is very important; equally important is the light collection efficiency for the detector. To this end, reflectors (diffuse, specular) and various surface finishes are very commonly used in scintillation detectors. In this design though, the use of a reflector on the flat surfaces of the scintillator was not feasible due to the presence of photosensors on both sides.

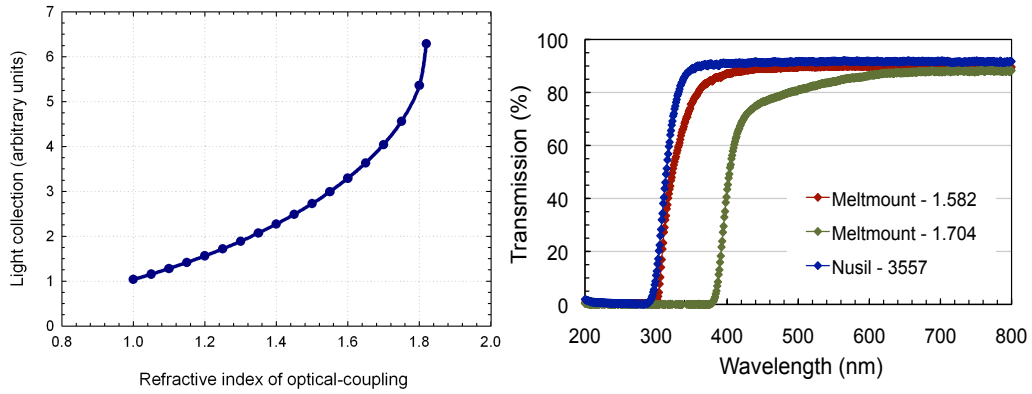

Figure 4.28. Optimizing optical coupling. *Left*: Theoretical benefit of optimizing the optical coupling. *Right*: Examining transmittance for select optical glues offering improved coupling.

The scintillation photons generated from the gamma-ray interaction spread out isotropically. On encountering a material boundary, the optical photons

undergo either reflection or refraction. The phenomenon of reflection or refraction is dependent on the refractive indices of the materials at the interface. As scintillators typically have a refractive index higher than one, an optical coupling is used to help efficiently pipe the light from the scintillator. The efficiency of the optical-coupling depends on its refractive index and transmittance. Theoretically, the effectiveness of the optical-coupling (as a function of its refractive index) is shown in Figure 4.28 (calculated by using solid angle integrals, assuming a LSO scintillator). For optimal transmission, the couplant should have a refractive index, which is the geometric mean of the material it interfaces [154]. In the case of the prototype detector (refractive indices of 1.82 and ~1.5), this effectively translates to a refractive index of ~1.7. Improving the light collection efficiency should decrease noise arising due to photostatistics. This should potentially improve spatial resolution, energy resolution, and possibly even timing resolution. Since the transmittance of the optical coupling is an equally important parameter, this was measured for a few select optical coupling media possessing a higher refractive index (closer to 1.7). Specifically, the transmittance of Meltmount-24150 (refractive index = 1.582; Cargille Labs, Cedar Grove, NJ), Meltmount-24170 (refractive index = 1.704) and Nusil-3357 (refractive index = 1.57; Nusil Silicone Technology, Carpinteria, CA) were evaluated (Figure 4.28).

4.4.3.3 Photosensor

Numerous improved photosensors have already been investigated and discussed in the previous section (Chapter 4.3). Their gain and noise properties have also been thoroughly investigated. Additionally, quantum efficiency for the S8664 family of APDs was characterized (in a manner

similar to for the RMD APDs), and is shown in Figure 4.29. As expected, they offer higher quantum efficiency when compared with the RMD APDs.

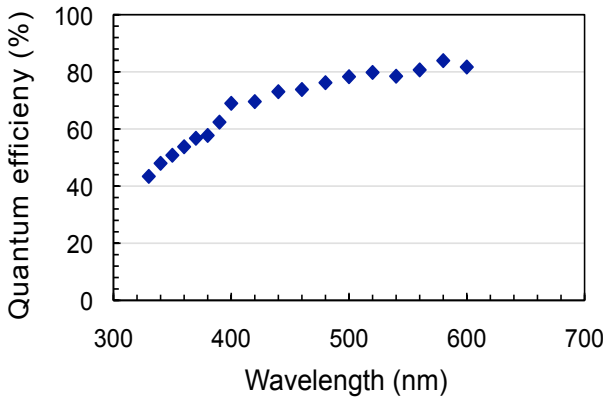

Figure 4.29. Measuring quantum efficiency of the Hamamatsu APD.

4.4.3.4 Front-end electronics:

A detailed evaluation of various preamplifier-shaper combinations (readily available or needing minimal modifications) had already been performed. They were performed for the RMD APD, and also for other available improved APDs (Chapter 4.3).

4.4.4 Optimizing Detector Design

As outlined at the beginning of this chapter, the immediate goal was to develop a fully instrumented prototype detector. Detailed electronic noise optimization studies had already indicated a redesign of the readout electronic boards. Subsequently, detailed investigations to assess, as well as improve and optimize each of the detector components in the existing prototype were performed. Since a detailed GATE Monte Carlo model had already been developed, it was meaningful to use it to methodically evaluate

the influence and role of each of the detector components on the final detector performance. Hence, the GATE Monte Carlo model was immediately used for the following purposes:

1. To help make an informed decision for expeditious building of a fully instrumented prototype detector.
2. Understand the influence of various detector parameters on detector performance.

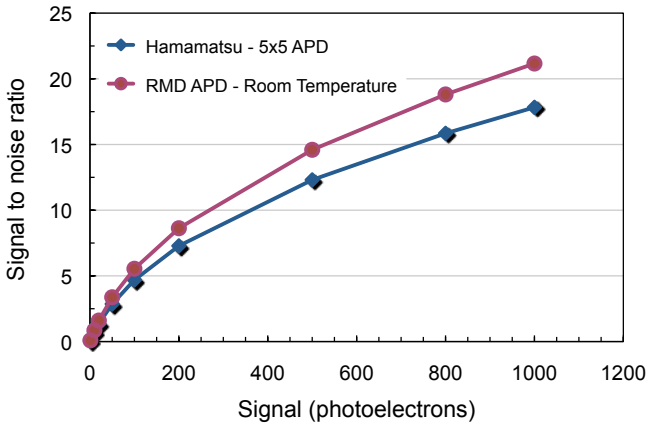

Figure 4.30. Comparison of the expected SNR for the RMD (8 x 8 mm^2), and Hamamatsu (5 x 5 mm^2) APDs: The minimum ENC achievable with readymade electronics was used to compute the data. As shown, for a given signal, the RMD APD offered better SNR.

Thorough investigation of the existing detector components had revealed several improvements to possibly improve the existing prototype detector. The PerkinElmer APDs seemed to be an excellent replacement for the RMD APDs, but were available in limited quantities and expensive. The S8664 APDs (i.e. Hamamatsu) on the other hand had good noise performance and quantum efficiency, but poor packing fraction. A comparison of the expected SNR revealed a lower SNR was expected from the Hamamatsu APDs (e.g. for a 400 photoelectron signal, ~15% lower SNR was predicted when compared

with the RMD APDs, Figure 4.30). The SNR though did not quantify the exact gains in detector performance. Hence, the previously developed fully Monte Carlo GATE model (Chapter 4.4) was used to estimate this.

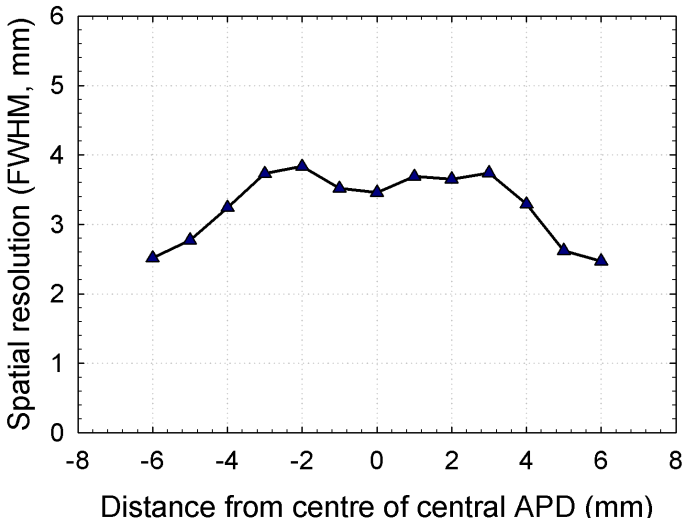

Figure 4.31. Estimating the transverse spatial resolution for an optimized detector design using the Hamamatsu APDs. Performance was estimated using a fully Monte Carlo model built using the GATE package.

To evaluate detector performance, the previously developed GATE model (Chapter 4.4.1) was adapted for a improved detector utilizing the Hamamatsu APDs (active area 5 x 5 mm^2). The model was updated to reflect, a 0.5 mm thick layer of Nusil-3357 and 0.5 mm thick layer of epoxy to model the APD surface (refractive index of 1.5; personal communication, Hamamatsu Photonics, Japan). The model was also updated with APG gain of 200, quantum efficiency of 70% (at 420 nm), electronic noise of 2500 e- rms and an excess noise factor of 2.2. The spatial resolution of the detector was estimated with a 662 keV source described in the earlier section. After correcting for the inherent non-linearity associated with using Anger

positioning, an average spatial resolution of ~3.4 mm FWHM was estimated. When compared with the expected performance of the RMD detector, the poorer predicted spatial resolution was consistent with the lower SNR expected from the Hamamatsu APDs (2.9 mm FWHM expected with the RMD detector).

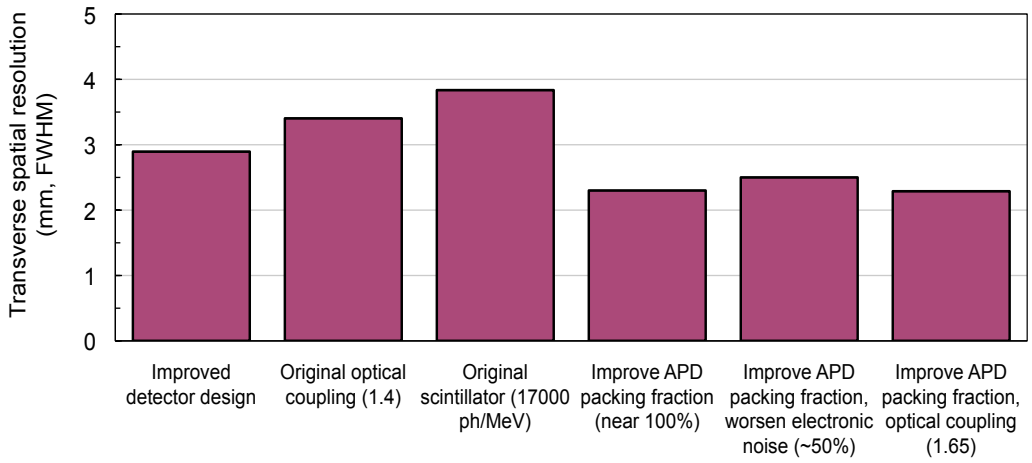

Figure 4.32. Optimizing detector design using the fully Monte Carlo GATE model: Determining effect of detector components on transverse spatial resolution.

The GATE model was also used to thoroughly investigate the influence of various detector parameters on detector performance. Specifically, their effects on spatial resolution and energy resolution of the detector were investigated. As shown below, among the various detector optimizations, the packing fraction of the APD and optical coupling significantly affected both the transverse spatial (Figure 4.32) and energy resolution (Figure 4.33) of the detector.

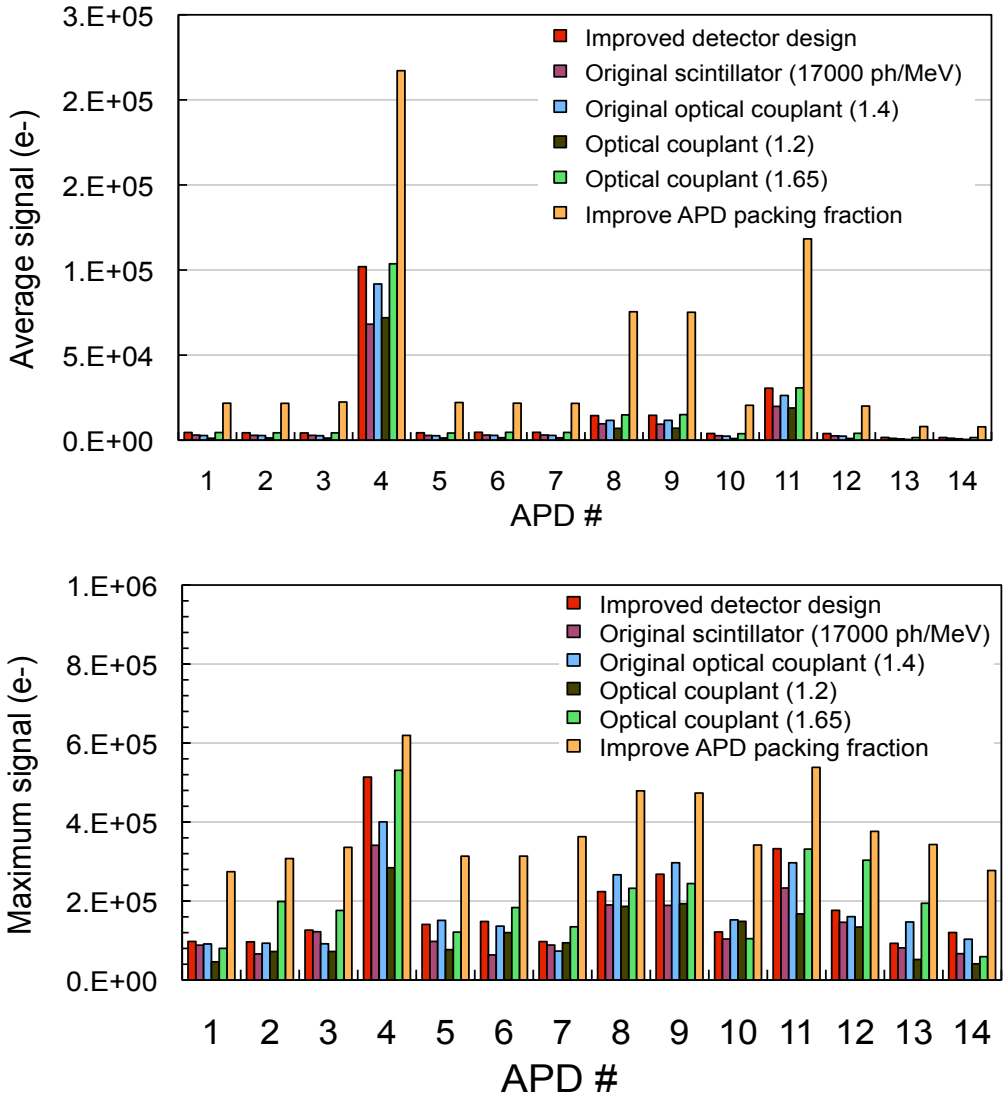

Figure 4.33. Optimizing detector design using the fully Monte Carlo GATE model: Determining effect of detector components on energy resolution. Plots show average signal (*top plot*) and maximum signal (*bottom plot*) for each APD, with a point source centered and normally incident on APD #4.

5. An Improved Light-Sharing Detector

Chapter 4 described various detector optimization studies performed to help develop a complete prototype detector. Those studies ranged from improving electronic noise, to understanding and improving each of the existing detector components.

This chapter discusses the implementation of an improved detector resulting from those detailed optimization studies. More specifically, it discusses the design, construction, and characterization of a fully instrumented prototype detector. The validation of a previously developed Monte Carlo model, using experimental results from the improved detector is also discussed herein.

5.1 APD Selection

Given the previously existing choices, the RMD APDs seemed a reasonable choice for building an initial prototype detector. While the detector demonstrated early promise, subsequent and extended assessments and experiences raised concerns over the reliability of these APDs. While it could be unwarranted to blame the APDs alone, the initial batches of APDs received were indeed fragile. With recent progress in the development of large-area devices, APDs from Hamamatsu and PerkinElmer were possible alternatives. While the PerkinElmer devices seemed the most attractive (low noise, good quantum efficiency, and active area), they were expensive, and

available only in limited quantities. On the other hand, Hamamatsu APDs despite their poor packing fraction, offered moderate gain, good quantum efficiency, and relatively low noise. A batch of the S8664 Hamamatsu APDs (5 x 5 mm^2) had already been procured for building a separate gamma-ray imager for locating illicit nuclear material [155]. Consequently, considerable experience and confidence had been gained with their working and reliability. Detailed detector optimizations (discussed in Chapter 4) had already suggested a redesign of the multichannel preamplifier-shaper module. Also, the Monte Carlo model suggested reasonable performance for an optimized prototype using Hamamatsu APDs. Since the initial objective was to demonstrate proof-of-concept, for sake of economy and speed, it was decided to make use of the Hamamatsu APDs to build an optimized prototype detector.

5.2 APD Performance Evaluation

Before assembling the detector, performance of these APDs (Hamamatsu S8664-55) was assessed. In particular, their gain, dark current, electronic noise, and typical PET performance measures were measured.

Gain for the APD was measured with a pulsed light source. Light from a 400 nm LED was piped through a ~0.5 mm optical fiber, and radiated onto the face of a single Hamamatsu APD. The APD was biased (model 6487; Keithley Instruments Inc, Cleveland, OH) and read out with a BNL designed preamplifier-shaper combination (IO-446 and IO-708). The amplified, shaped APD signal was further sent to an oscilloscope, which was used to measure the final amplitude.

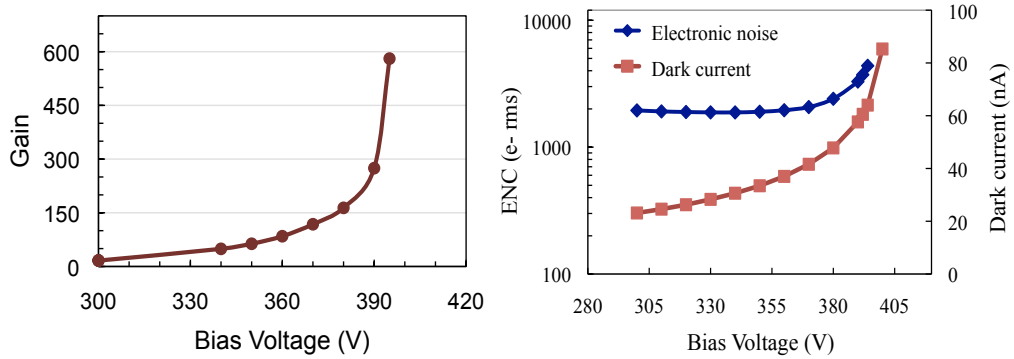

Figure 5.1. *Left*: Gain curve measured for a single Hamamatsu APD with a pulsed light source. *Right*: Leakage current and electronic noise measured with a single Hamamatsu APD biased and read out by a commercially available preamplifier followed by a second-order Gaussian shaper.

The entire process was repeated over the range of bias voltages for the APD (10 V – 400 V). The device was assumed to have unity gain at a low bias voltage (40 – 50 V) where the avalanche process is uninitiated. The gain at any bias voltage is then computed by normalizing the APD output at that bias voltage to its corresponding output at unity gain (Figure 5.1). To minimize errors caused by possible drifts in the LED output, care was taken to ensure that the measurement was completed in a relatively short period (minutes). The Keithley-6487 also doubled up as a picoammeter to help measure the leakage current for the APD (Figure 5.1). All measurements were performed inside a light-tight box, at room temperature. Electronic noise was also assessed with a CR-110 preamplifier (Cremat Inc., Watertown, MA), and a BNL designed second-order Gaussian shaping amplifier (Figure 5.1). Detailed noise measurements were performed previously, and the above measurements confirmed the relatively low-noise capability of these APDs.

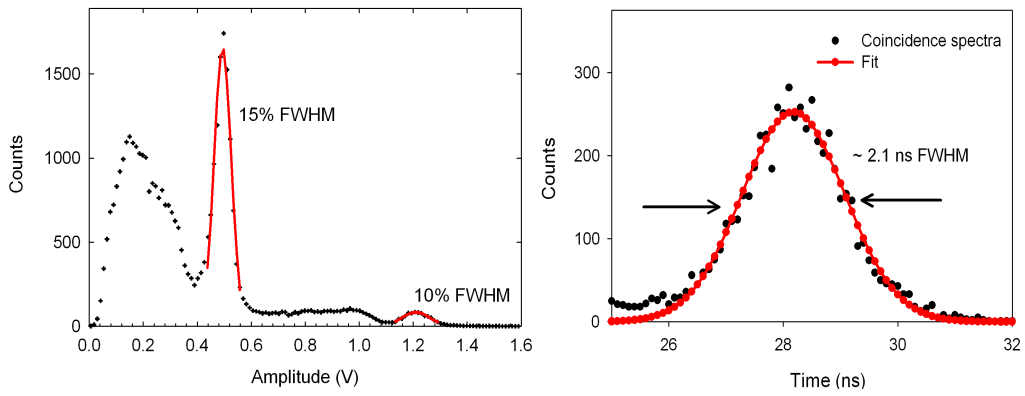

Figure 5.2. *Left*: Energy spectrum obtained with a ^{22}Na source and a single Teflon wrapped 2 x 2 x 10 mm^3 LSO crystal mounted on the APD. *Right*: Coincidence time spectra obtained with the same detector in coincidence with a fast BaF_2-PMT detector. An energy resolution of 15% FWHM, and a timing resolution of 2.1 ns FWHM was measured at 511 keV.

Energy and timing measurements for the APD were carried out with a single 2 x 2 x 10 mm^3 Teflon wrapped LSO crystal. A single APD was biased and readout with the same preamplifier-shaper combination. For the energy measurement, the amplified and shaped APD output was first fed through standard NIM electronics, and subsequently digitized with a fast digital sampling oscilloscope (TDS-7254B, 2.5GHz; Tektronix, Beaverton, OR). With a ^{22}Na source, an energy resolution of 15% FWHM was measured at 511 keV (Figure 5.2).

Timing resolution was also measured with the above LSO-APD combination in coincidence with a fast BaF_2-PMT detector (H5023 PMT; Hamamatsu Photonics, Japan). Standard NIM electronics was used to process signals from both the detectors. Timing for both the detectors was generated with the help of standard leading edge discriminator (model 708; Philips Scientific, NJ). The output from the discriminator was fed to a gate and delay generator, and finally to a fast digital sampling oscilloscope (TDS-7254B, 2.5 GHz).

While the setup was not optimized for fast timing, a coincidence timing resolution of ~2.1 ns was observed at 511 keV (Figure 5.2).

5.3 Detector Design

Since many of the optimizations could be implemented relatively quickly, most of the components on the improved prototype detector were updated.

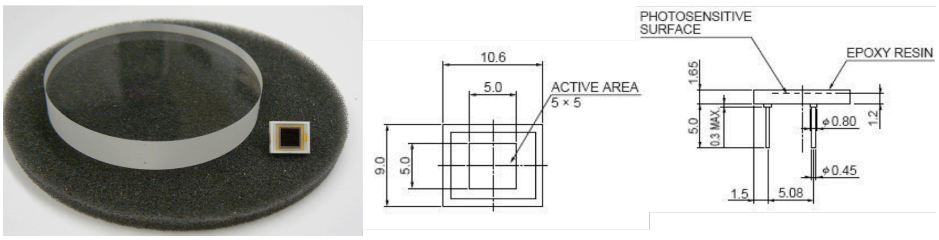

Figure 5.3. *Left*: Photograph of the LYSO scintillator (10 mm thick, 6 cm diameter) and a single Hamamatsu APD used to build an improved prototype. *Right*: An engineering drawing of the APD [156], illustrating the poor packing fraction for the APD.

Originally, it was expected that a 10 mm thick LSO scintillator would provide good resolution and sensitivity when compared to existing commercial systems. Since the S8664-55 APDs were reasonably sized for a 10 mm thick scintillator, the improved detector continued to use a 10 mm thick scintillator. Specifically, a 10 mm thick, 6 cm diameter disk of Cerium doped lutetium yttrium oxyorthosilicate (LYSO) scintillator (Crystal Photonics Inc, Sanford, FL) was used.

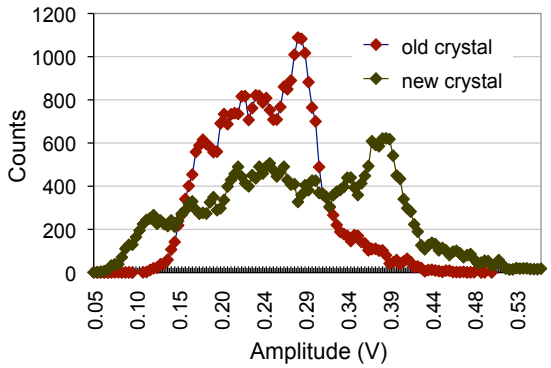

Figure 5.4. Measuring the light output of the new LYSO scintillator slab: Background subtracted energy spectrum for the improved LYSO scintillator coupled to a PMT, and irradiated with the collimated ^{137}Cs source. Also shown for comparison is the spectrum obtained with the older LSO slab.

LYSO is a more recent scintillator, and has properties very similar to that of LSO. A concern with the original LSO crystal was its relatively low light yield. Hence, the light output of the new slab was measured before assembling the detector. As before, the LYSO slab was coupled to a 2" PMT (Hamamatsu R2059) and irradiated with the collimated ^{137}Cs source. The entire process is outlined in Section 4.4.2. An intrinsic light yield of ~26000 photons/MeV was measured for the new LYSO slab. Figure 5.4 shows a direct comparison of the energy spectrum obtained with a ^{137}Cs source. As expected, the LYSO scintillator had improved light yield when compared to the old scintillator (~30%, consistent with calculations).

The improved design also had an updated optical coupling. The original detector used a thin layer of Sylgard-527 (refractive index = 1.4; Dow Corning Corporation, Midland, MI). While Sylgard-527 in itself works well, and has been successfully used as an optical-couplant [124, 157], a higher refractive index optical coupling would be more appropriate and beneficial for this design. Specifically, it would improve the light collection efficiency.

Monte Carlo investigations have already demonstrated this significance; spatial resolution directly correlates with the scintillator light output and light collection efficiency (Figure 4.32). Also, improving the light collection efficiency should help improve energy resolution (Figure 4.33), and possibly timing resolution. Typically, energy resolution in a detector helps to improve the image quality by rejecting scattered events. However, in this detector design, (explained later in Chapter 6), improving the energy resolution also helps in improving the spatial resolution.

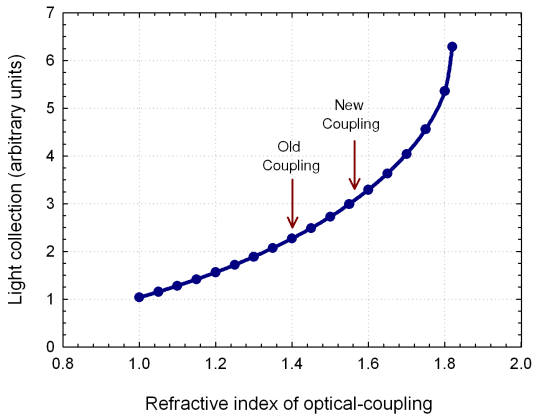

Figure 5.5. Improved optical coupling: The new detector used an improved optical coupling, which was expected to provide ~30% improvement in the intrinsic light collection efficiency. The intrinsic light collection efficiency was computed by calculating the total solid angle subtended onto the face of the LSO scintillator.

LS–3357 (Nusil Silicone Technology, Carpinteria, CA) is a two-part encapsulation gel used in the photonics industry, and has a refractive index of ~1.57 at 420 nm. Also, it has excellent transmission at 420 nm (Figure 4.28). Curing of the optical coupling takes place at 75 °C (6 hours) or 100 °C (4 hours). Further, unlike most other optical couplants, this couplant is not permanent. Figure 5.5 illustrates the benefit of using this new optical-coupling (~35% better light collection when compared to using Sylgard-527).

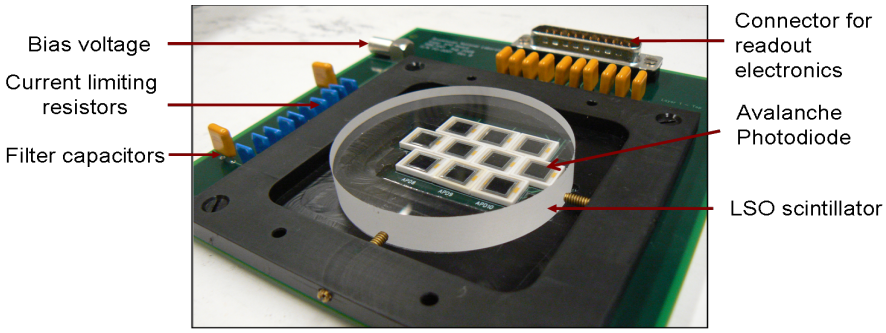

Figure 5.6. An improved light-sharing prototype PET detector assembled with a 10 mm thick LYSO slab (60 mm diameter) and large-area APDs from Hamamatsu. A similar arrangement of APDs and readout electronics is used to read the opposite face of the scintillator.

The final detector design consisted of a 10 mm thick LYSO slab coupled with Hamamatsu APDs on both sides of the scintillator (Figure 5.6). New PCBs to accommodate the Hamamatsu APDs were designed. The newer PCBs had a similar architecture to the previous detector boards, but were simpler and compact due to the lack of high voltage (> 1kV) components. Each board filtered and distributed the bias voltage for up to 10 APDs. While each APD had a separate voltage feed line, provision was also made to operate the detector with a single supply (via an onboard LEMO connector). The board also included current limiting resistors and capacitors to filter the bias voltage. With the lower leakage current, a more appropriate series resistor (10 MΩ, to reduce the parallel noise contributions) was chosen. The rest of the detector design was similar to the first prototype detector (Chapter 3.5).

5.4 Readout Electronics

In Chapter 4.3.1 it was demonstrated that the BNL modified slow-preamplifier offered the lowest ENC for the S8664 APDs. Since these APDs

had slightly higher leakage current than expected (Figure 5.1), an ENC measurement was performed after the detector was assembled. In addition to the previously tested preamplifiers, the commercially available eV preamplifier (eV-5093; EI Detection and Imaging Systems, Saxonburg, PA [158]) was also evaluated (Figure 5.7). Since the commercial eV preamplifiers offered the lowest ENC, it was decided to instrument the detector with the eV-5093 preamplifiers. Each preamplifier was followed by a BNL IO-708 shaping-amplifier (~70 ns peaking time). The multi-channel preamplifier-shaper unit was redesigned to accommodate sixteen of these preamplifier-shaper combinations. Since the BNL-slow preamplifier and the eV-5093 had a fairly similar configuration (8-pin, SIP; 0.100" spacing), the boards were made general-purpose and could accommodate either of the preamplifiers.

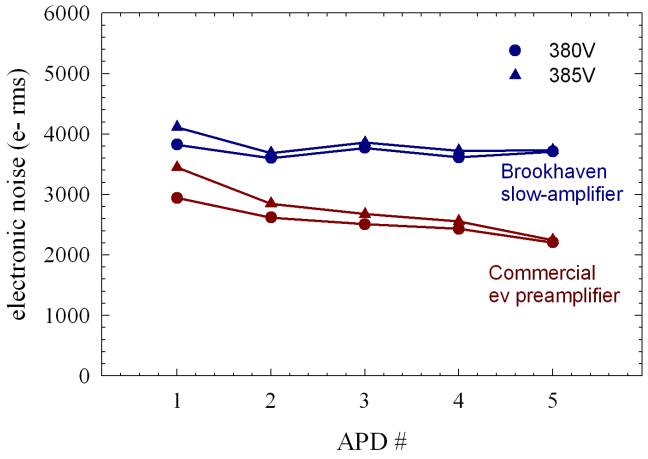

Figure 5.7. Electronic noise performance of the assembled detector: Since the eV preamplifier offered the lowest electronic noise, they were used to fully instrument the detector.

Overall, the readout electronics consisted of the preamplifier-shaper combination (eV5093 preamplifier and BNL IO-708 shaping amplifier)

followed by standard NIM electronics. The amplified and shaped APD signals were first fed to a variable-gain amplifier (model 778; Phillips Scientific, NJ). Apart from providing additional gain (x5 – x10), the amplifier helps equalize gain variations within the detector. The APD signals were then passed onto standard fan-out modules (model 744; Phillips Scientific), which generate the energy and timing signals. Energy for the event is decoded by using the analog sum of all 14 APDs. The timing trigger is generated with a leading edge discriminator (model 708; Phillips Scientific) and an analog sum of all 14 APDs. The APD signals were finally fed to the input of a VME peak sensing ADC (model V785, 12 bit ADC; CAEN Technologies, Italy). A schematic representation of the complete readout electronics is shown in Figure 5.8.

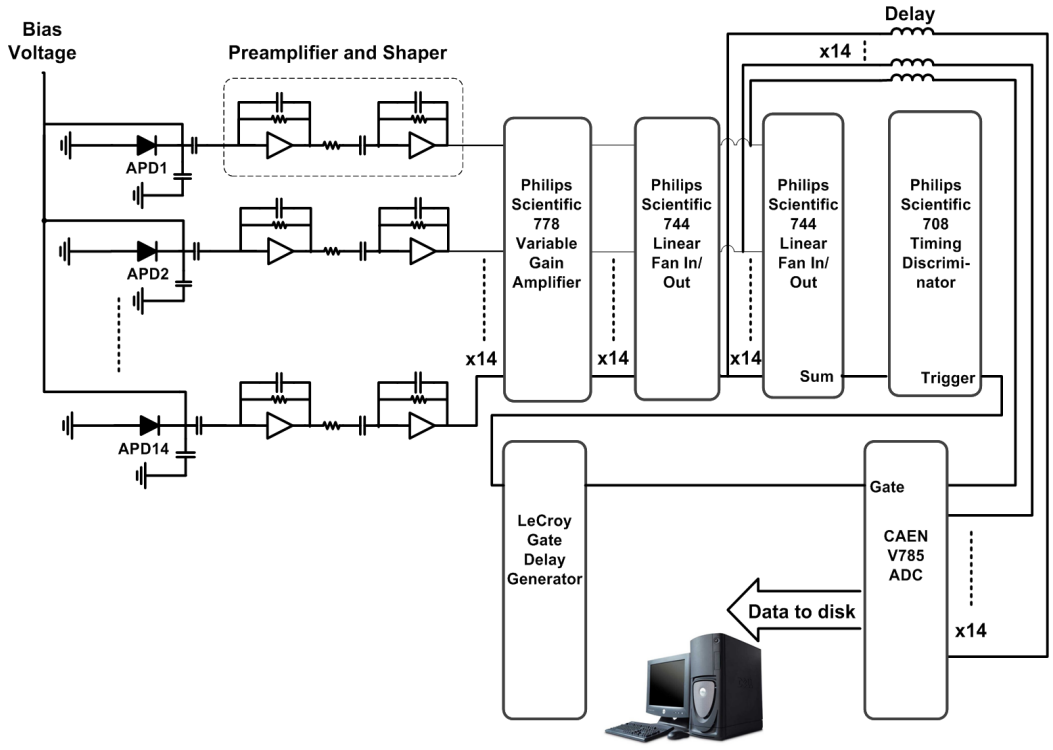

Figure 5.8. Schematic of the electronics used to readout signals from the detector.

For the light sharing design, it is important that the data acquisition have a linear response. While the ADC was expected to have very good linearity (Integral Nonlinearity of +/- 0.1% and a Differential Nonlinearity of +/- 1.5%), it was important the entire data acquisition behave in a linear fashion. To test this, test pulses from a precision DG535 pulse generator (Stanford Research Systems, Sunnyvale, CA) were fed into a test capacitor at the preamplifier input. The amplified, shaped output signal was finally fed to the peak sensing ADC. The linearity of the DAQ was charted by varying the test pulse amplitude (Figure 5.9) and it was found to be excellent.

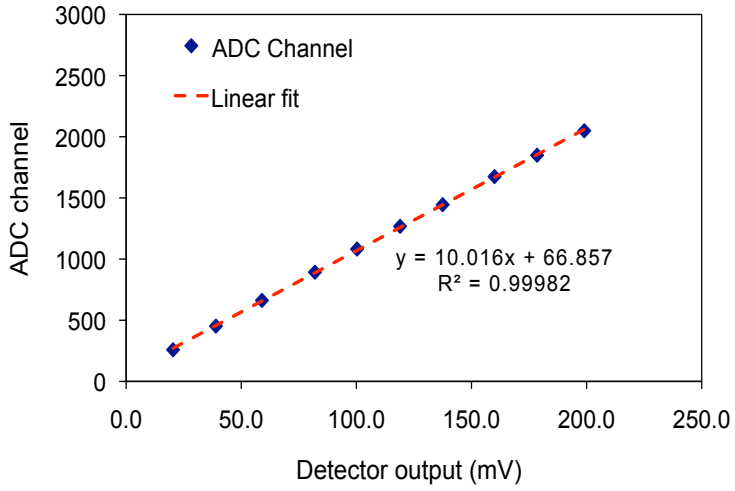

Figure 5.9. Data acquisition linearity: DAQ linearity was measured by injecting a calibration pulse via a test capacitor available on the preamplifier.

Data (on an event-by-event basis) from the ADC was stored to disk, and analyzed off-line using the ROOT package [136]. Software to perform the data analysis was written in C/C++.

5.5 Performance Evaluation

A collimated beam is necessary to characterize the performance of a light-sharing detector, and most of the DAQ components were drawn upon from the previously developed experimental setup. As before, the collimated 662 keV ^{137}Cs source was used to measure the detector performance (Chapter 4.4.1).

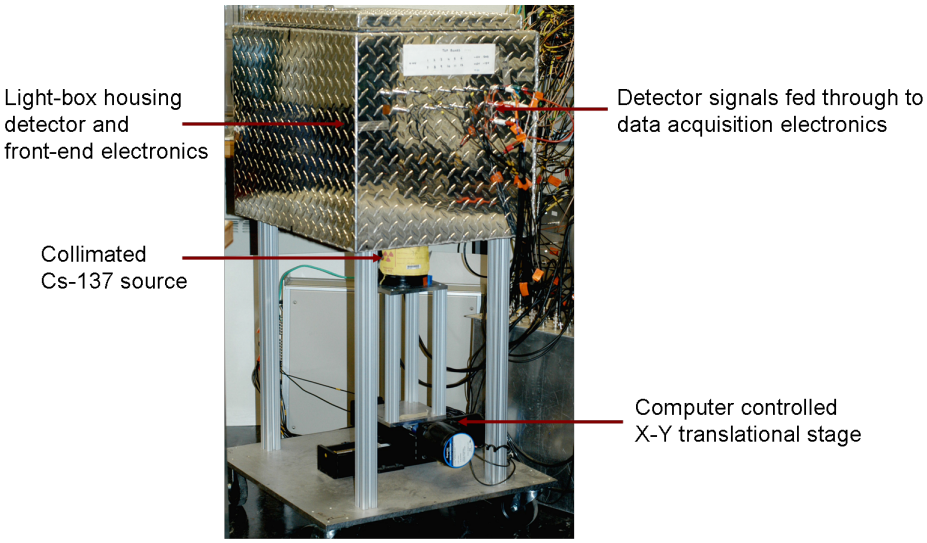

Figure 5.10. An improved experimental setup housing the detector and collimated Cs-137 source on a computer controlled translational stage. The entire detector was enclosed in a metal light-box that also acted as a faraday cage, shielding against stray electromagnetic interferences.

The assembled detector and its associated front-ends were placed inside a light-tight box. To help reduce pickup noise, the light-tight box was made of aluminum, which also doubled as an electromagnetic shield (Figure 5.10). The inside of the box was painted black to reduce any possible light reflections from the polished metal surfaces.

5.5.1 Transverse Spatial Resolution

Before assessing the performance of the detector, it was essential to establish the relative positions of the source and the detector. For this, the collimated source was stepped along the face of the detector and responses from the APDs on the bottom side were measured.

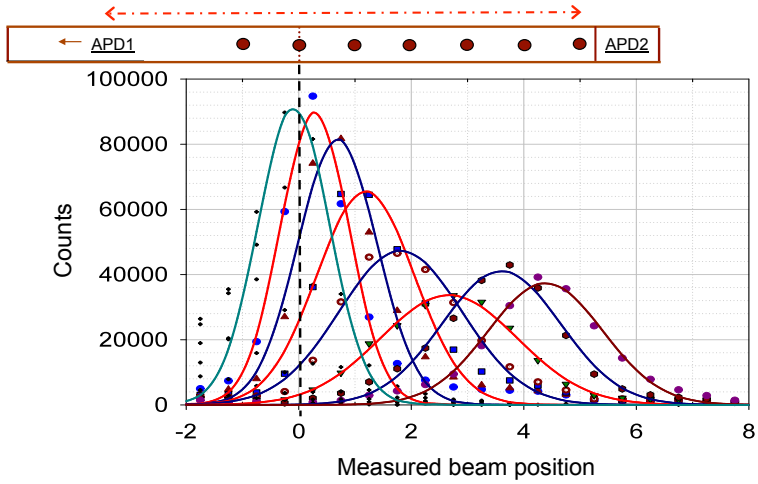

Figure 5.11. Position histogram measured by stepping a collimated ^{137}Cs source and traditional anger logic along the face of the detector. Also shown is the Gaussian fits overlaid on top of each of the position histograms.

Prior to characterization, the optimal operating voltage for the detector was determined in the manner discussed in section 4.2. Instead of modeling the SNR, energy resolution for a single APD (coupled with a Teflon wrapped 2 x 2 x 10 mm^3 LSO crystal) with measured at 511 keV. The bias voltage was varied, and a best energy resolution (indicative of SNR) was obtained at a bias voltage of 380 – 390 V.

To characterize spatial resolution, the collimated ^{137}Cs source was scanned in 1 mm steps across the face of the detector. A sum of all 14 APDs was used to generate the energy and trigger signals. Transverse position was measured

by using traditional Anger logic and all 14 APDs from both sides of the detector. For each beam position, the transverse position was computed and histogrammed (Figure 5.11). A Gaussian fit was then used to compute the spatial resolution (FWHM) for that beam position. For each source position, data was collected for approximately 20 min. To eliminate the LSO background, a pre-measurement background scan was collected (without the source) and subtracted from the spatial resolution measurement data. After correcting for the nonlinearity, a transverse spatial resolution of ~3 mm FWHM was measured (Figure 5.12).

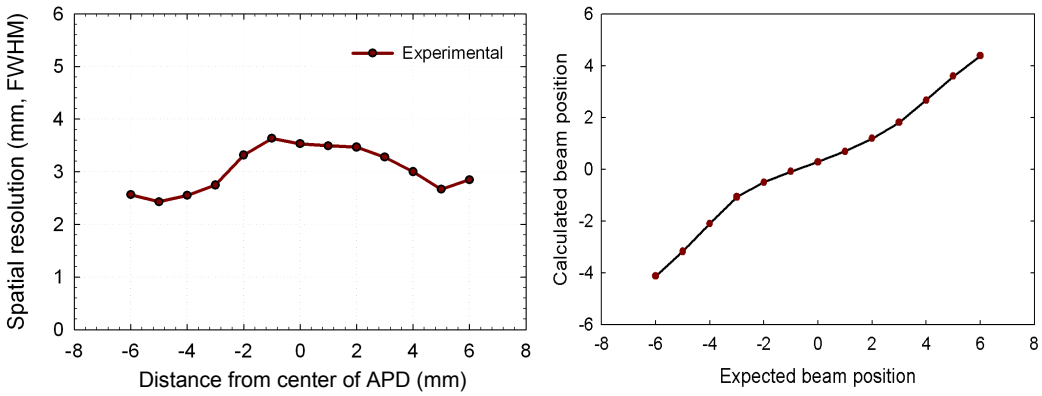

Figure 5.12. Measuring transverse spatial resolution (X-direction) for the improved prototype detector. *Left*: Transverse spatial resolution measured with a collimated ^{137}Cs source & traditional Anger-logic. As the separation of the peaks is dependent on the beam position (*right*), a position dependent calibration was used to correct for the detector nonlinearity.

Similar experiments to characterize the transverse spatial resolution in the other transverse direction (Y-direction) were also performed. A spatial resolution of ~2.8 mm FWHM was measured (Figure 5.13). The slightly better (~10%), and more uniform spatial resolution is likely due to the improved linear-sampling arising from offsetting the APDs (Figure 3.15) along the Y-direction.

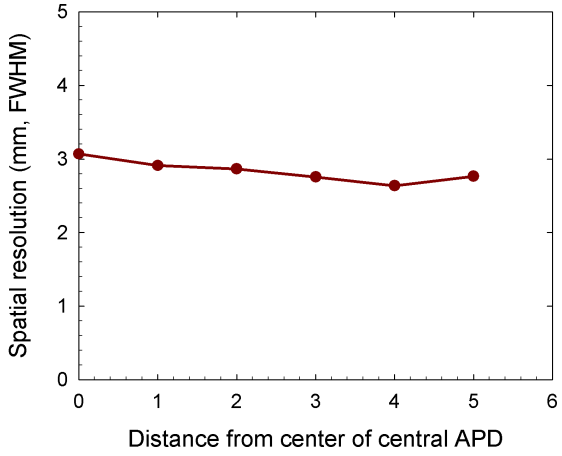

Figure 5.13. Transverse spatial resolution measured along the Y-direction, i.e. along a direction perpendicular to the previous measurement (see Figure 5.12). The improved sampling (APDs offset relative to each other) assuaged detector nonlinearity and provided a more uniform spatial resolution.

Traditional (and most of the current) light-sharing detectors have photosensors on only one side of the scintillator. They also possess a light-guide to ensure a minimum amount of light sharing between adjacent photosensors. In contrast, the above detector lacks a light-guide. The lack of a light-guide is compensated by coupling large-area photosensors onto both sides of the scintillator. While the use of photosensors from both sides is necessary to measure DOI, it was also expected to provide a better measure of the transverse spatial resolution. Including a larger number of APDs though, comes at the expense of adding noise contributions from each of the APDs. The flexibility in choosing a different trigger and event-positioning scheme (decreasing the number of APDs) though is largely dependent on the detector light spread function, APD size, electronic noise and DAQ architecture. While most light sharing detectors make of photosensors on a single side, it was hypothesized that making use of APDs from both sides should provide a better and more uniform estimate of transverse position.

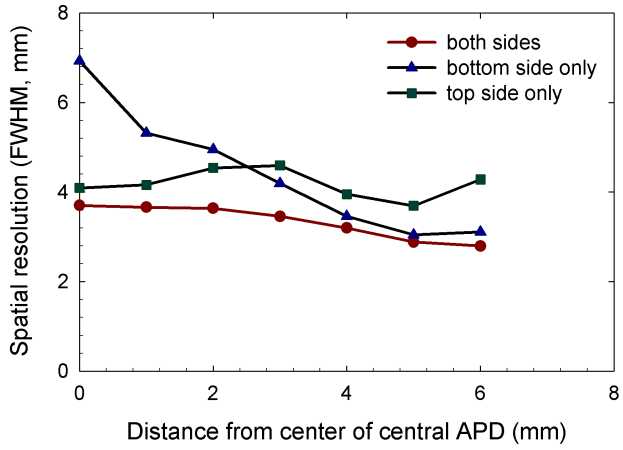

Figure 5.14. Transverse event positioning: An investigation of the merits of using APDs from either the front, back or both sides for transverse event positioning. Note that the collimated beam was centered on an APD on the bottom board.

To evaluate this, the collimated ^{137}Cs source (as described above) was stepped along the face of the detector in 1 mm intervals. Traditional Anger-logic using all 14 APDs, or only each of the seven APDs on either top or bottom sides was used to measure the transverse position. As usual, the spatial resolution calculation was corrected for the nonlinearity introduced by using simple Anger-logic. As expected, the use of APDs from both sides (top and bottom) provided a better measure of the transverse position (Figure 5.14). It is important to note that using APDs from both sides should also provide a better estimate for energy and possibly timing resolution.

Spatial resolution measurements (Figure 5.11 – Figure 5.14) were performed with the detector biased at 380 V. A negligible change in the transverse spatial resolution was observed at a detector bias of 385 V (supporting the fact that optimal bias was predicted to be around the 380 – 390 V range).

5.5.2 Energy Resolution

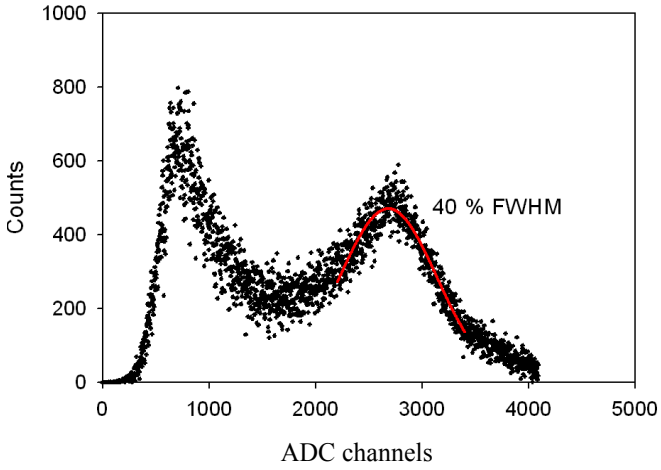

Figure 5.15. Energy resolution measured with the collimated Cs^{137} source. The analog sum of all 14 APDs was used to measure the energy for the gamma ray.

Energy resolution for the detector was measured with the same apparatus (described above) used to characterize detector spatial resolution. The ^{137}Cs source was positioned at the center of the detector, and its response was measured. The APD signals, after amplification and shaping were fed to standard NIM electronics, and finally to a peak sensing ADC. The sum of all 14 APD channels (top and bottom sides) was used to measure the gamma-ray energy. An energy resolution of ~40% FWHM was measured. Figure 5.15 shows a sample energy spectrum from the detector measured with the beam centered at the center of the detector. The poor energy resolution is attributed to the poor packing fraction of the APD (25% active area, poor light collection efficiency).

5.5.3 Coincidence Timing Resolution

The spatial, and energy resolution for the detector was characterized above with a collimated ^{137}Cs source, which only emits a single gamma at 662 keV. Measuring coincidence timing resolution necessitated a positron-emitting source. Since the mechanical setup had the provision to accommodate a coincidence detector, the collimated ^{137}Cs source was replaced with a ~30 μCi ^{68}Ge source (Sanders Medical Products Inc., Knoxville, TN) and a coincident detector was also added.

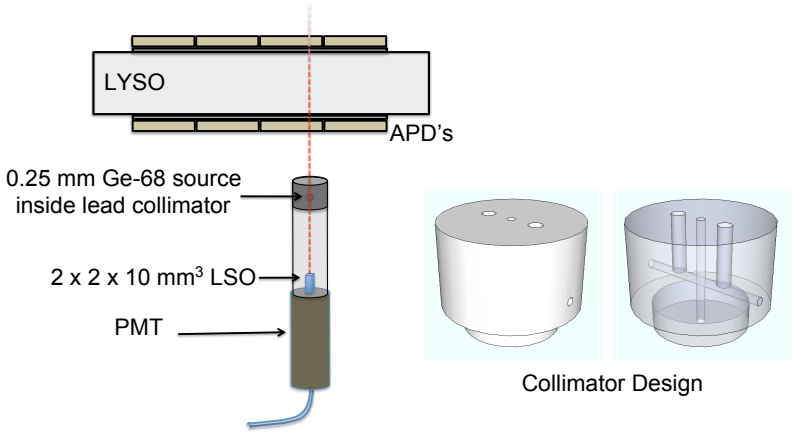

Figure 5.16. Coincidence setup: A 0.25 mm diameter ^{68}Ge point source was electronically collimated with a single 2 x 2 x 10 mm^3 LSO–PMT combination to produce a narrow beam of 511 keV photons. *Inset*: A specially designed lead collimator with a ~2 mm bore surrounded the source to decrease accidental coincidences.

Figure 5.16 illustrates the coincidence setup. A 0.25 mm diameter, ^{68}Ge point source was "electronically" collimated by requiring a time coincidence with a single 2 x 2 x 10 mm^3 LSO–PMT (R3479; Hamamatsu Photonics, Japan) combination, to produce a narrow beam of 511 keV photons. The entire assembly was mounted onto the X-Y translational stage. To decrease the

number of accidental coincidences, a custom designed lead collimator (~0.9" tall, 2 mm bore) surrounded the ^{68}Ge source.

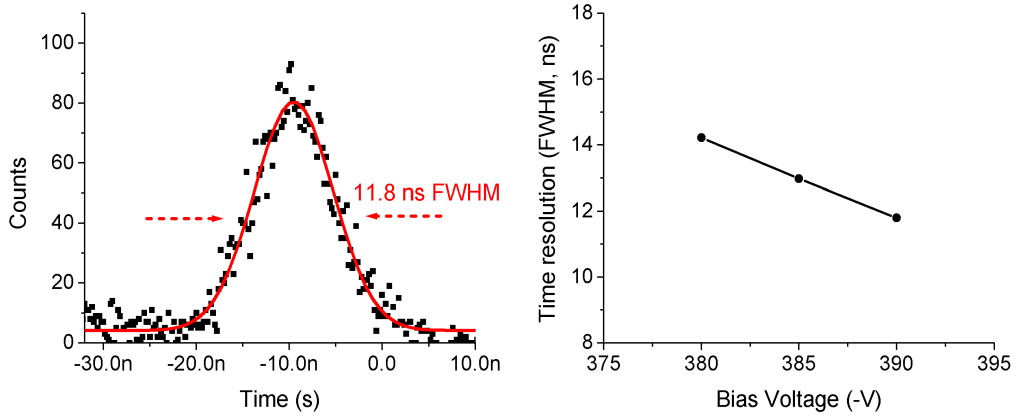

Figure 5.17. Coincidence timing resolution of the detector. *Left*: Coincidence timing resolution of the detector was measured using a Ge-68 point source in coincidence with a fast LSO-PMT detector. *Right*: Optimizing coincidence timing. Timing resolution of ~12 ns FWHM was measured with a 350 keV threshold on a leading edge discriminator.

Timing measurements for the detector were conducted with the above-described LSO-PMT combination. The APD signals after amplification, and shaping (70 ns) were passed through standard NIM fan-out circuits. The analog sum of all 14 APDs was then fed through a standard leading edge discriminator (model 708; Phillips Scientific, NJ) to produce a logic pulse. The signal from the coincidence detector (LSO-PMT) was fed through a fast shaping amplifier (model 474; Advanced Measurement Technology, Oak Ridge, Tennessee) and further to the same leading edge discriminator. The logic pulse from both the detectors were finally sent to a time to amplitude convertor (TAC, model 566; Advanced Measurement Technology, Oak Ridge, Tennessee), with the PMT providing the "start" signal. Figure 5.17 shows a coincidence-timing spectrum obtained with the source at the center of the detector and a 350 keV threshold on the light-sharing detector.

Since the timing resolution is dependent on the APD bias voltage, it was measured for a range of bias voltages. A timing resolution in the 12 – 15 ns range was measured (Figure 5.17). While the APD in itself could achieve far better timing (Figure 5.2), timing for the detector was mainly limited by the poor APD packing fraction (i.e. poor light collection efficiency; Figure 4.33). Also, all 14 APDs did not have similar breakdown voltages, and the bias voltage optimizations were limited by the APD with the lowest breakdown voltage.

5.5.4 Validating Monte Carlo Simulations with Experimental Data

While the Monte Carlo model is a powerful tool on its own, the real power lies in its ability to help with rapid optimization and "virtual" prototyping. To this end a validated model is invaluable. A detailed, fully Monte Carlo model (with GATE) had already been built and used to predict detector performance for an optimized detector (Chapter 4.4.1). The model though did not use measured estimates for many of the detector components. For the model to be validated with experimental data, it was important that the components be updated to reflect their true nature. The updated model used measured estimates for most components and included:

- A 10 mm thick LYSO slab having a light yield of 26,000 photons/MeV, an intrinsic resolution of 10% and refractive index of 1.82
- A 0.5 mm thick layer of optical coupling with a refractive index of 1.57
- APD quantum efficiency of 70% at 420 nm
- APD gain of 200
- Electronic noise of 2,500 e- rms

The simulations were repeated, and all the data was treated in the same manner as the experimental data. Data analysis also accounted for the operating energy threshold, and the size of the ^{137}Cs source (1.3 mm, conservative) used in experiments. The updated simulations were compared, and validated with experimental data on various fronts: spatial resolution (Figure 5.18), energy resolution (Figure 5.19), and their individual APD spectra under varying experimental conditions (Figure 5.20, Figure 5.21, Figure 5.22). As shown below, the Monte Carlo predictions were in very good agreement with experimental data.

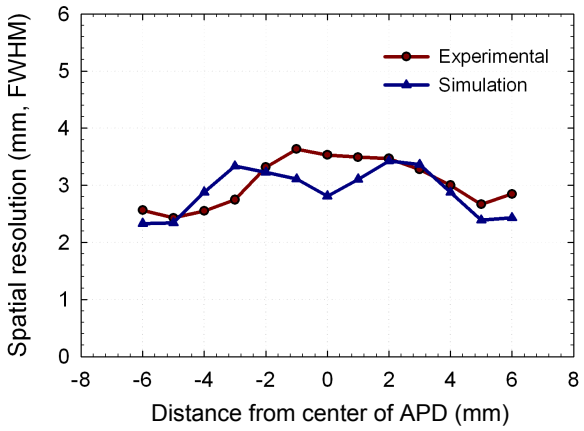

Figure 5.18. Comparison of transverse spatial resolution obtained from Monte Carlo simulations with experimental characterization. The measured spatial resolution was corrected for contributions arising due to size of the beam.

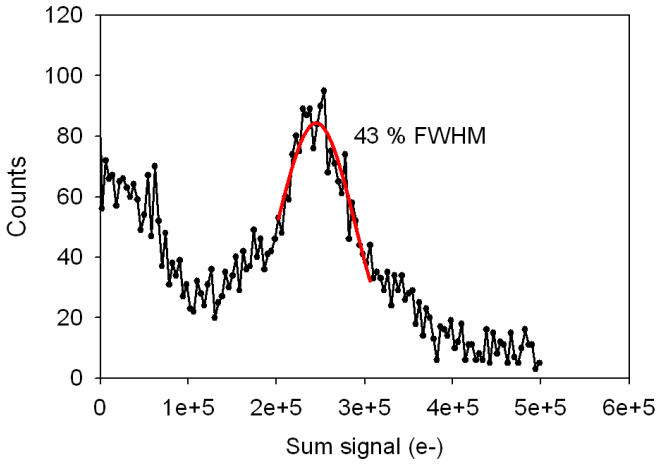

Figure 5.19. Energy spectrum for a ^{137}Cs source obtained via Monte Carlo simulations with experimental characterization: The predicted energy resolution was comparable to experimentally obtained data (Figure 5.15).

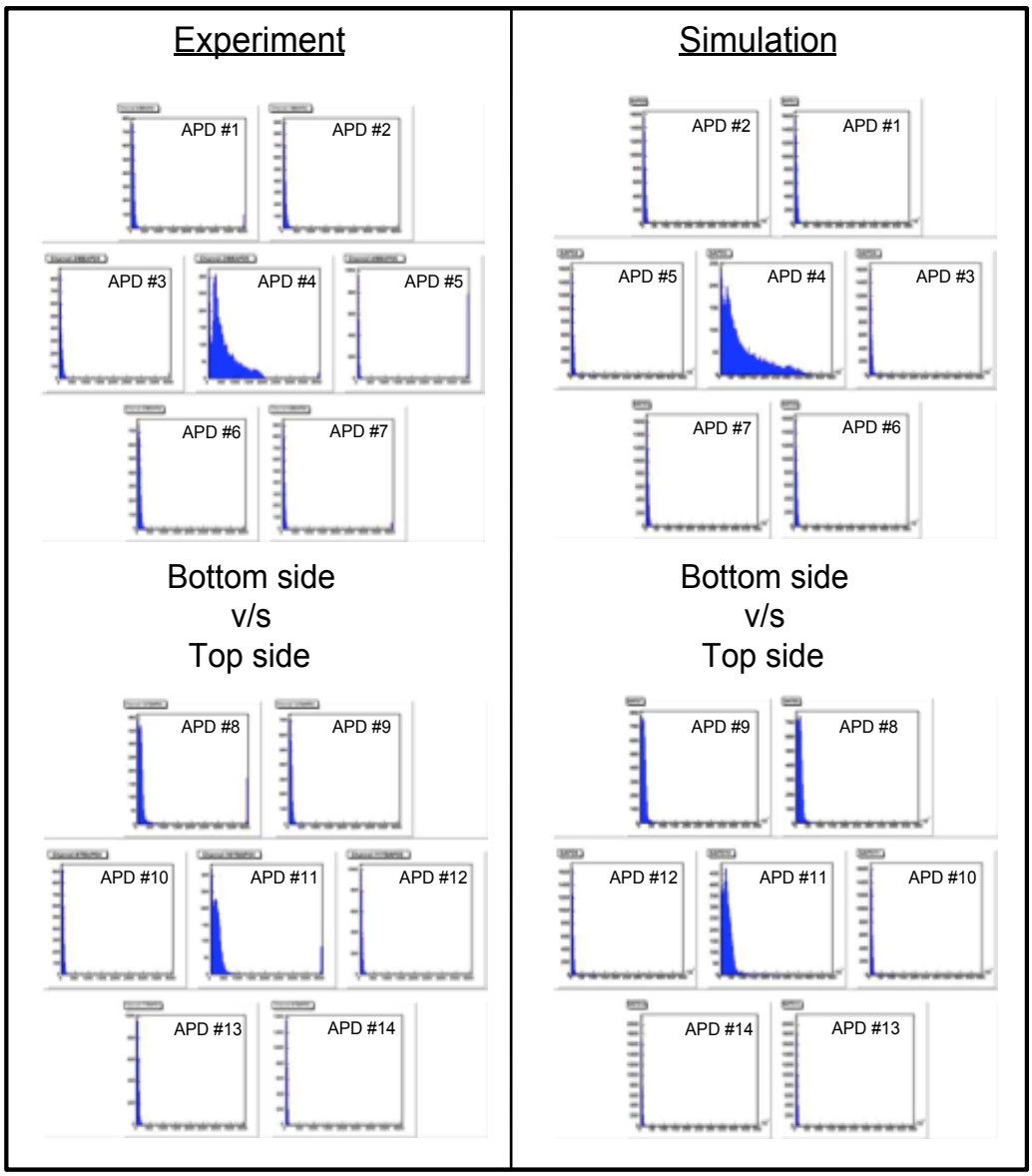

Figure 5.20. Validating the GATE Monte Carlo simulation with experimental data from the improved prototype detector. Comparison of the individual APD spectra with the source positioned at the center of APD#4.

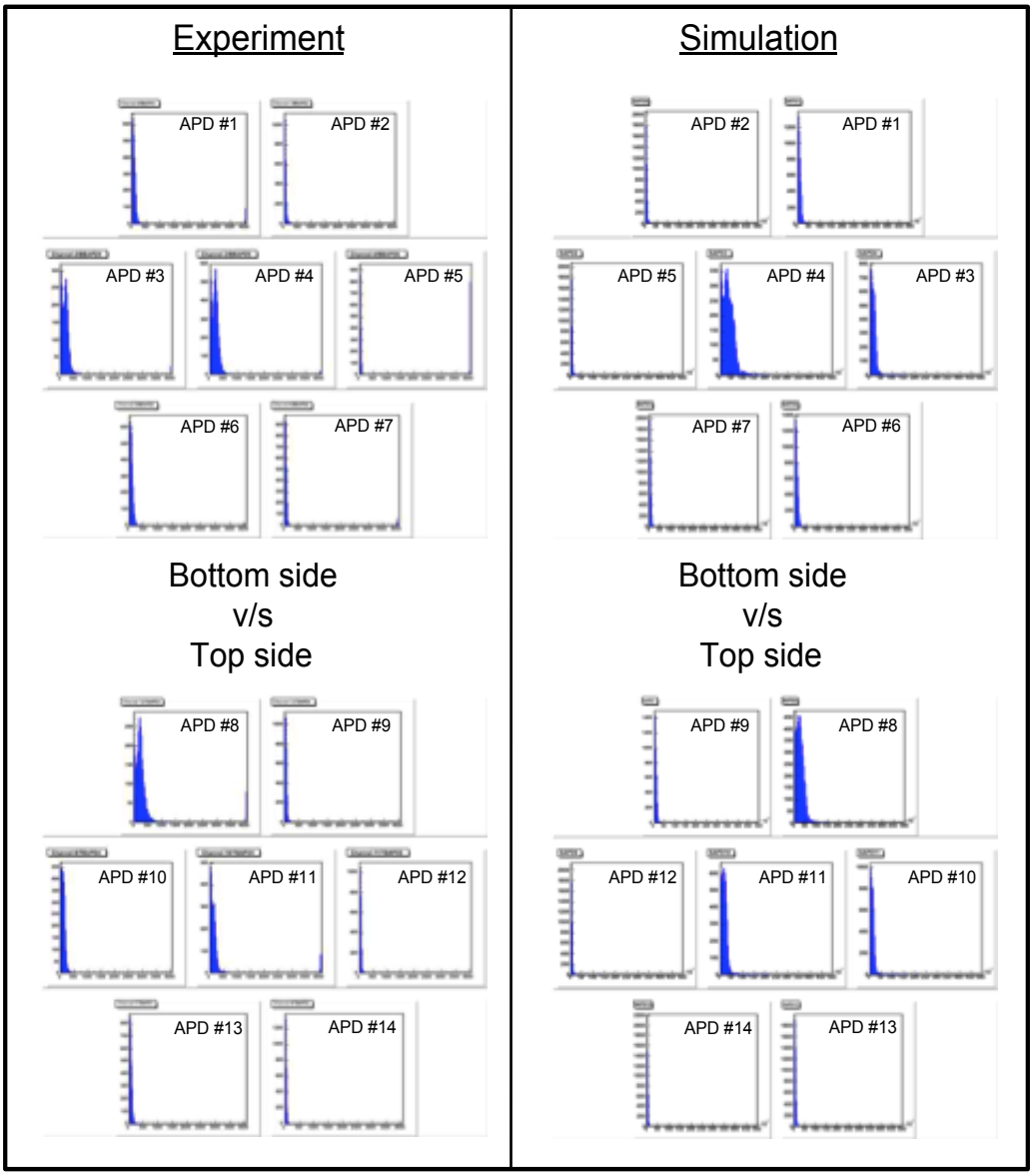

Figure 5.21. Validating the GATE Monte Carlo simulation with experimental data from the improved prototype detector. Comparison of the individual APD spectra with the source positioned between APD#3 and APD#4.

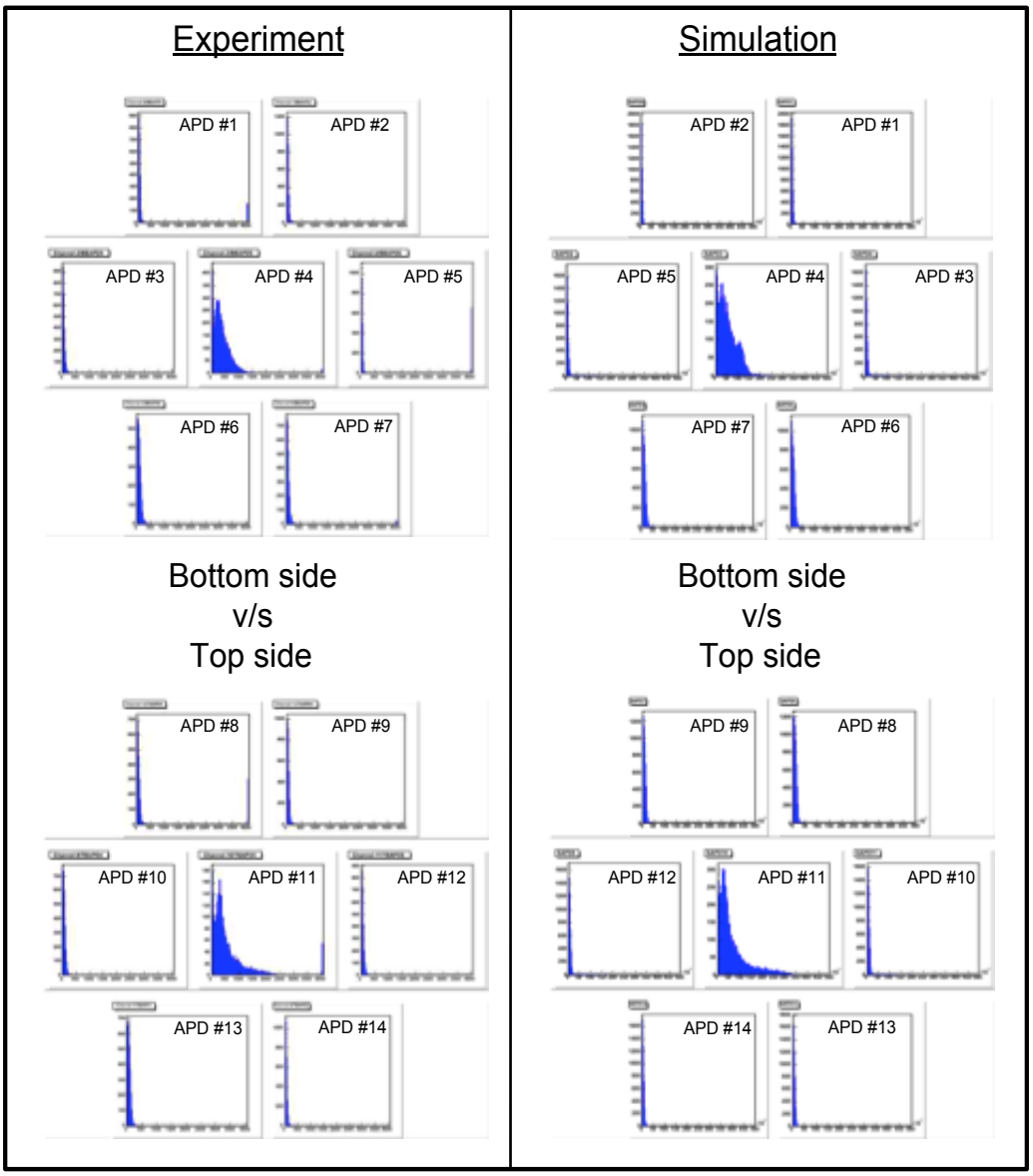

Figure 5.22. Validating the GATE Monte Carlo simulation with experimental data from the improved prototype detector. Comparison of the individual APD spectra with the source positioned at the center of APD#11.

5.5.5 Depth-of-Interaction studies

A unique advantage of placing photosensors on both sides of the scintillator is the ability it provides in measuring DOI of the gamma-ray interaction. DOI in this detector can be assessed by comparing the dispersion of signals on both sides of the scintillator. The dispersion information has been derived and combined into a depth-parameter (dp) (section 3.1), which can be used as a measure of the depth at which gamma rays interact.

$$dp = \sqrt{\left(\sum_{i=1}^{7} s_i (x_i - \bar{x})^2 \Big/ \sum_{i=1}^{7} s_i\right)} - \sqrt{\left(\sum_{i=8}^{14} s_i (x_i - \bar{x})^2 \Big/ \sum_{i=8}^{14} s_i\right)} \tag{5.1}$$

$$dp = \frac{\sum_{i=1}^{7} s_i (x_i - \bar{x})^2 \Big/ \sum_{i=1}^{7} s_i}{\sum_{i=8}^{14} s_i (x_i - \bar{x})^2 \Big/ \sum_{i=8}^{14} s_i} \tag{5.2}$$

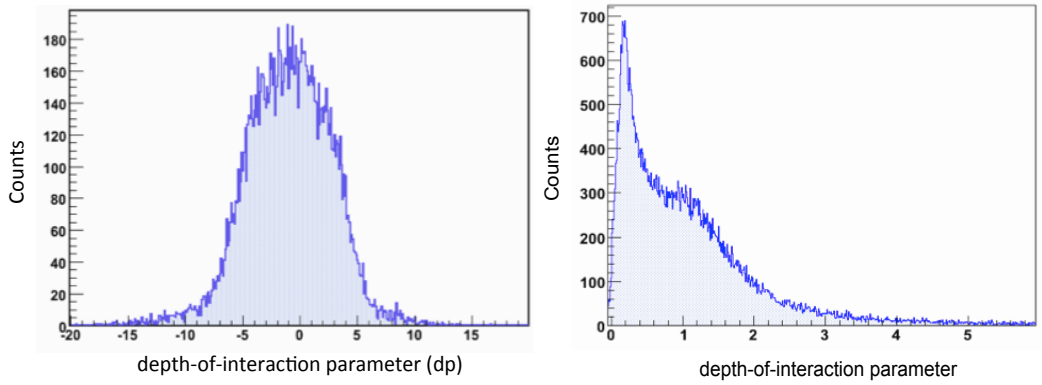

Figure 5.23. Depth-of-interaction parameter: A histogram of the depth-of-interaction parameter (experimental) for a normally incident ^{137}Cs beam near the center of the detector. (*Left*) difference of the widths i.e. equation 5.1, and (*Right*) ratio of the variances i.e. equation 5.2.

The depth-parameter (dp), as depicted by equations 5.1 and 5.2, is a continuous function and is representative of the various depths at which the gamma ray interacts (smaller DOI parameter indicates a shallower interaction depth). Figure 5.23 depicts a histogram of the depth parameter for a ^{137}Cs beam normally incident near the center of the detector. The distributions are shown for both the depth-parameters:

- equation 5.1: difference of the widths of the signal distributions
- equation 5.2: ratio of the variances of the signal distributions

To compute the distributions, the collimated ^{137}Cs source was positioned near the center of the detector. The DAQ was triggered using a sum of all 14 APDs (top and bottom), and data was collected in a similar fashion as the spatial resolution of the detector was measured. The APDs data was used offline to compute the distributions. Note that the shape of the depth-parameter distribution is dependent on the gamma ray interaction location (due to the detector packing fraction).

5.5.5.1 Experimentally Validating the DOI parameter

Since the depth parameter was recently developed, it necessitated a careful evaluation and validation before subjecting it to further assessments. The availability of a fully instrumented detector provided the ability to directly test it via experiments.

To achieve reasonably good detection efficiency, a PET detector must utilize a sufficiently thick scintillator. Also, the spatial resolution in a continuous scintillator detector is intrinsically related to the scintillator thickness. Even with a thinner scintillator the light-spread function and consequently the spatial-resolution) is broadened by the varying depth-of-interaction of the

gamma ray (e.g. Figure 4.8). While traditional light-sharing detectors do not have any depth-sensing capabilities, the DOI measuring ability of this detector should help resolve the depth-dependent broadening of the light-response function. To test this, the DOI parameter was used to evaluate:

a. Data from a single APD on the detector (Figure 5.24)
b. Data from the entire detector i.e. all 14 APDs (Figure 5.25)

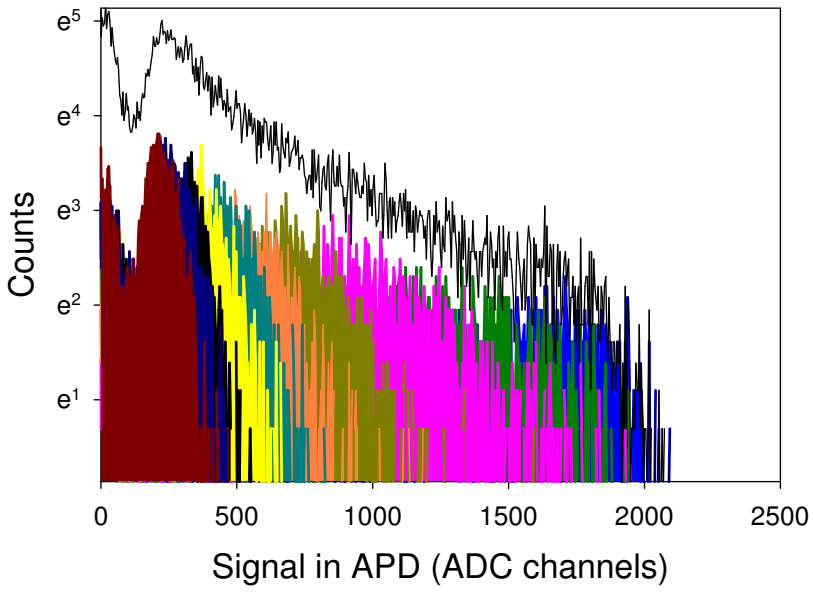

Figure 5.24. Validating the depth-parameter: Histogram (experimental) of the signal from a single APD, plotted as a function of the depth-parameter. The ^{137}Cs beam was aimed normally at the center of the APD. The DOI parameter was used to discretize the scintillator thickness, and consequently the total APD signal into 10 depth levels (1 mm each). As expected, a shallow interaction gave the maximum signal (dark blue curve). The black curve is the composite light from event occurring at all depths inside the scintillator. *Note*: Log scale is used to highlight the differences among spectra.

The collimated beam was positioned at the center of the central APD on the bottom board and data was collected. DAQ was triggered using a sum of all 14 APDs. Data from all 14 APDs was used to compute the DOI parameter. The DOI–parameter was then used to separate the 10 mm thick scintillator into

10 depth levels (each 1 mm deep). In conjunction, the APD signal was also separated based on the depth reported by the DOI parameter. Figure 5.24 demonstrates the effect of using the DOI parameter to deblur the depth-dependent broadening of the APD signal. As expected, a shallower interaction provided a higher APD signal (larger solid angle) and vice versa. The DOI parameter was also tested to validate the dependent broadening of the light collection efficiency in the detector. Instead of discretizing a single APD signal, the sum of all 14 APDs (energy signal) was separated (ten, 1 mm depths) based on the depth reported by the DOI parameter (Figure 5.25).

Further, since the light-spread function can be improved by using the DOI parameter, it can be postulated that it could also help improve the transverse spatial resolution. Figure 5.26 shows the transverse position histogram for a single beam position, with and without using the DOI parameter. Also, spatial resolution measurements (described in Chapter 4.4.1) were performed with and without using the depth-parameter. The red curve in Figure 5.27 shows the spatial resolution without using the depth-parameter. The data was also analyzed by using the depth-parameter to account for the depth at which the gamma ray interacts. Ten 1 mm depth segments were used in the data. Figure 5.27 demonstrates that the DOI parameter helps in decreasing the light-spread function. The large variations seen here can be attributed to the poor APD packing fraction (~25%).

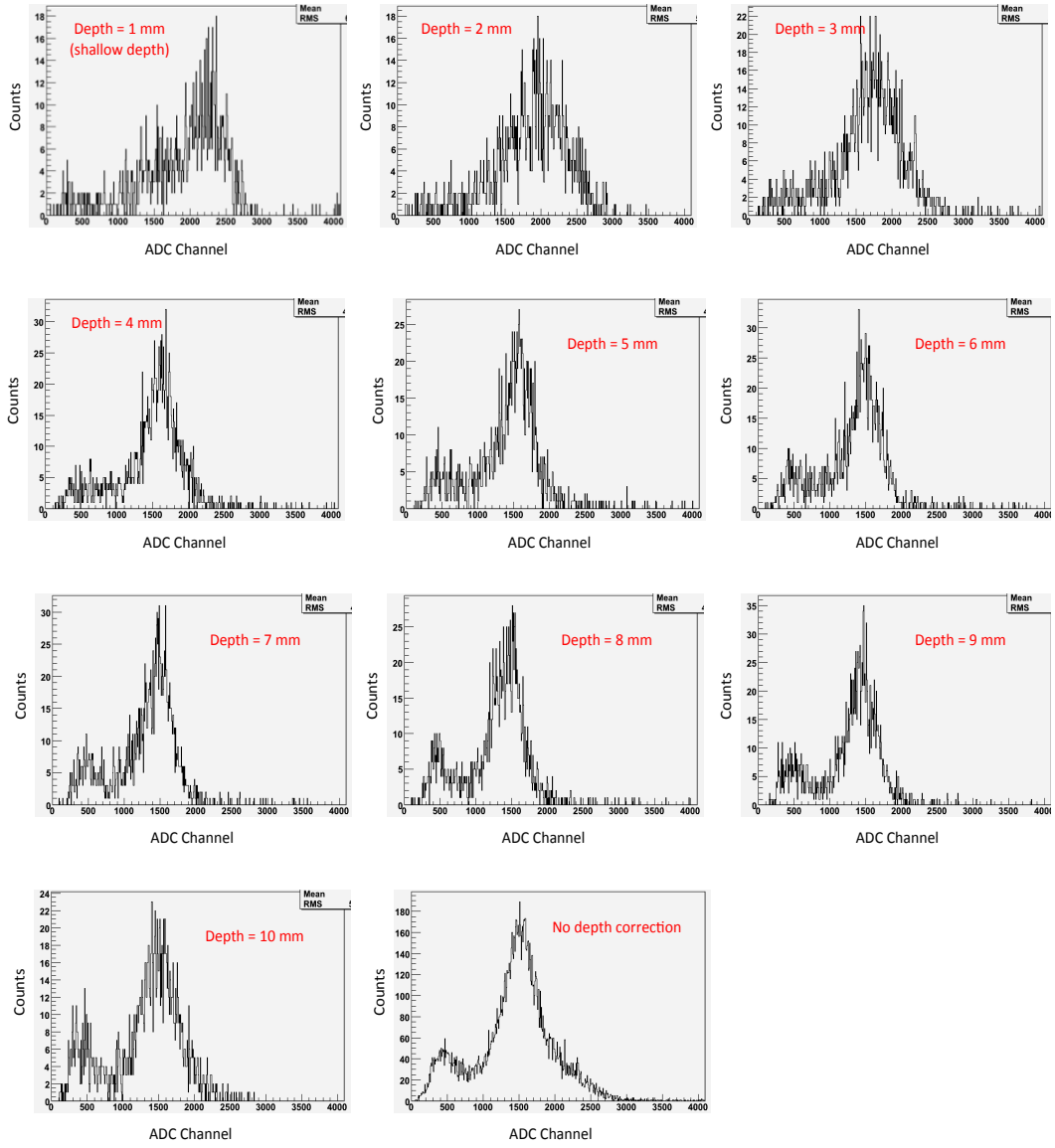

Figure 5.25. Using the DOI parameter to reduce the depth-dependent broadening of the light collection efficiency in the detector: Experimental confirmation with a normally incident beam at the center of the detector. The sum of all 14 APDs was used. Also shown for comparison is the light collection without correcting for DOI (*bottom row*). Note the long tails on the uncorrected energy spectrum.

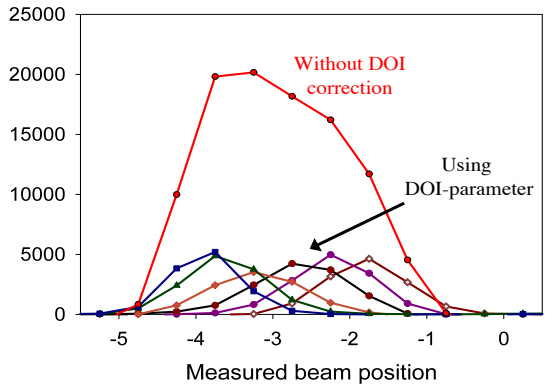

Figure 5.26. Indication that correctly identifying the depth-of-interaction could help improve the in-plane resolution: Experimental data from a ^{137}Cs beam positioned at the center of the detector. Using the depth-parameter resulted in position histograms with a narrower width.

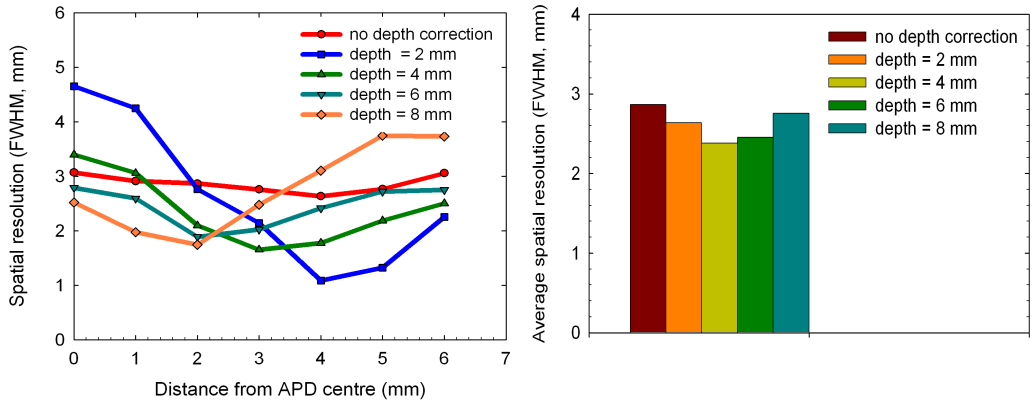

Figure 5.27. Verification that the DOI parameter can help reduce the blurring of the light-spread function and spatial resolution caused by the varying DOI for the gamma ray. The large variations in spatial resolution arise from the poor APD packing fraction. For comparison, spatial resolution measured without using the DOI parameter is also shown (red curve).

Both the depth-parameters (equations 5.1 and 5.2) worked equally well, and were validated with experimental data. However, since the "difference of widths" method is linearly related to depth for an idealized detector, and is a more well-behaved measure, it is preferred over the latter. Hereafter, any reference to the depth-parameter (dp) shall pertain to equation 5.1 i.e.

depth-parameter derived from using the difference of the widths of the signal distributions.

5.5.5.2 Predicting DOI resolution

DOI in discrete crystal PET detectors is typically measured by stepping a collimated beam along the length of the crystal (i.e. the depth direction for the detector). But given the large area of the detector, this was challenging to accomplish. Hence, a first estimate of DOI performance was obtained with the help of the validated GATE Monte Carlo simulations. Using these GATE simulations, 662 keV photons from a ^{137}Cs beam were aimed normally at the center of the detector. The DOI parameter was used to extract the DOI with 1 mm accuracy (i.e. ten, 1 mm depth segments). With an accurate knowledge of the true DOI, a correlation histogram between the measured DOI and the true DOI was computed. This data predicted a DOI resolution of ~2 mm FWHM for true photoelectric interactions occurring inside the scintillator (Figure 5.28).

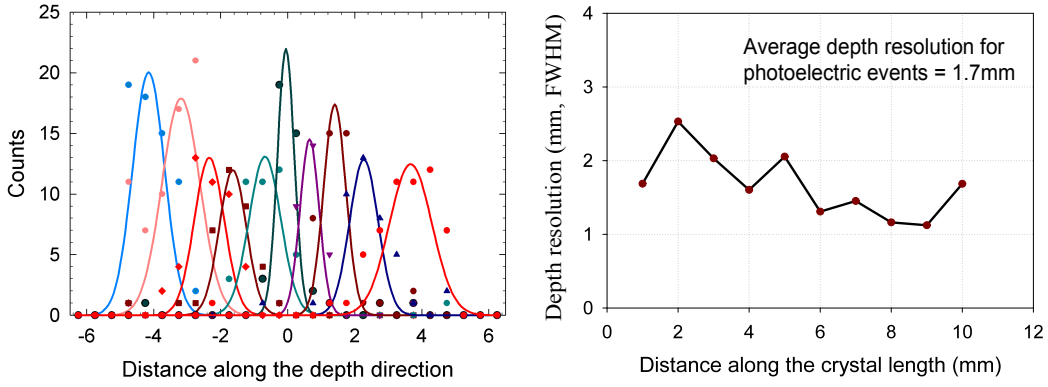

Figure 5.28. Predicting DOI resolution using the validated GATE simulations: L*eft*: Histogram of "measured DOI" (using the DOI parameter) for a normally incident ^{137}Cs beam at the center of the detector. The 10 mm thick scintillator was assumed to have 10, 1mm depth segments. *Right*: Data suggested an average DOI resolution better than 2 mm FWHM. Note: Only photoelectric interactions were considered.

6. Event Positioning in Continuous Scintillator Detectors

Chapter 5 discussed the design, implementation, and detailed characterization of an improved prototype detector. In that chapter, transverse positioning was accomplished by utilizing traditional Anger positioning logic. However, Anger-positioning is known to introduce nonlinearities, and is not ideally suited to exploit the full potential of this detector.

This chapter discusses the investigation and development of a novel maximum likelihood (ML) based event-positioning algorithm. The algorithm uses the DOI measuring capabilities of the detector to locate the three-dimensional (3-D) interaction location of the gamma ray inside the scintillator. The developed 3D-ML positioning algorithm is utilized to further characterize the performance of the improved detector. The algorithm is also used to experimentally measure DOI resolution for the improved detector.

6.1 Current Art

The gamma-ray interaction location (i.e. transverse position) in most light-sharing detectors is determined with the help of Anger-logic [93]. While its speed and relatively straightforward implementation makes it an attractive and widespread choice, it is known to have inherent nonlinearities.

The algorithm does not consider the statistical properties of the PMT responses, thereby mis-positioning events, and introducing bias.

Group	Readout	Scintillator thickness	Intrinsic DOI	Event positioning
Belgians /Delft	Semiconductor; either side	✪✪✪✪	✗	Neural networks
BNL	large-area semiconductor; both sides	✪✪✪	✔	3D maximum likelihood
Scottish	APD; layered	✪✪	✗	Statistics based
U. Penn	PMT	✪✪✪✪✪	✗	Maximum likelihood
U. of Wash	PSPMT; either side	✪✪✪	✔	Statistics based
Valencia	PSPMT	✪✪✪	✔	3D maximum likelihood

Semiconductor = APD/SiPM

Table 6-1: A summary of continuous scintillator detection, and event-positioning schemes being pursued by various research groups [53-55, 159-173].

A more sophisticated positioning scheme would definitely be useful. To this end, maximum likelihood [174] and neural network [175, 176] based techniques have been used to derive bias-free position estimates in a continuous scintillator. The development of efficient positioning algorithms to compute the interaction location inside a continuous scintillation detector is an active field of research in itself. Table 6-1 summarizes the various continuous crystal detector designs, and event positioning algorithms being pursued by various research groups around the globe.

Neural networks based position estimators have been investigated and successfully developed by [159, 160, 177, 178]. Their intrinsic capacity to help with classification, easily lends to position estimation. But at the same

time, their implicit and hidden ("black-box like") nature does not provide any information on the underlying process and limits the ability to understand and form correlations between various parameters of interest.

Maximum likelihood (ML) based estimators on the other hand are more thorough and exact in nature. Also, they are known to be robust, efficient, unbiased, and stable. Over the years, a variety of ML positioning algorithms have been suggested and developed [166, 167, 179-184]. While the methods have progressively improved, all of the above methods only estimated the two-dimensional response function (x, y). The depth dependence of the 2-D response function is well understood [185, 186]. Also, the depth dependence is of greater significance when using thick scintillators. More recently, [169, 187-189] have proposed maximum likelihood approaches that account for the problem in a fully three-dimensional manner. However, most of these approaches use an analytical function to model the depth-response, and later combine it with a measured 2-D response function to generate a fully 3-D detector model. By using analytical assumptions, the models likely sacrifice accuracy.

This work focuses on the development of a fully 3-D event-positioning algorithm that utilizes a measured system response to compute the 3-D interaction location of the gamma ray inside a continuous scintillator. Being a measured model, it would automatically be all-inclusive, and account for all real world effects (e.g. gamma-ray and optical photon generation and transport, light collection, gain mechanisms, electronic noise). Also, most of the groups (see Table 6-1) use photomultiplier tubes to read out the scintillator. Given the situation, the statistics describing the number of primary photoelectrons from any of the PMT's is well known, following Poisson statistics [190]. Replacing the PMT with an APD complicates the

noise model significantly. A measured model is well suited in this scenario and helps simplify the generation of an accurate system model.

6.2 3-D Maximum Likelihood Positioning

For any gamma-ray interaction inside a continuous scintillator, the photosensor responses are dependent on the 3-D interaction location (x, y, z) and the energy deposited by the gamma ray. Consider a set of N independent observations of X, say X_1, X_2, …, X_N. In this case, the observations are the detector responses (i.e. APD1, APD2, …, APD14), and θ is the parameter which the model investigates. The joint probability density function (pdf) for X_N is then denoted by:

$$f(X_1, X_2, \ldots, X_N \mid \theta) = f(X_1 \mid \theta) * f(X_2 \mid \theta) \ldots f(X_N \mid \theta) \tag{6.1}$$

$$P(X \mid \theta) = P(X_1, X_2, \ldots, X_N \mid \theta) = \prod_{i=1}^{N} f(X_i \mid \theta) \tag{6.2}$$

Now, given the sensor distributions, the likelihood that the gamma-ray originated from a particular location inside the crystal, can be computed by the likelihood function:

$$L(\theta \mid X_1, X_2, \ldots, X_N) = f(\theta \mid X_1, X_2, \ldots, X_N) = \prod_{i=1}^{N} f(\theta \mid X_i) \tag{6.3}$$

An easy way to estimate the parameter θ is to maximize the likelihood function, or equivalently its log-likelihood function.

$$\ln L(\theta \mid X_1, \ldots, X_N) = \sum_{i=1}^{N} \ln f(\theta \mid X_i) \tag{6.4}$$

According to ML theory, the best estimate of the interaction position ($\hat{\theta}$), given a distribution, is the one for which its probability is maximum, and can be computed by:

$$\hat{\theta}_{ML} = \arg\max_{\theta} \ln (\theta \mid X_1, \ldots, X_N) \tag{6.5}$$

6.2.1 Detector Calibration

As described in Chapter 5.5.5, one of the unique advantages of reading both sides of the scintillator is the ability it provides in measuring DOI for the gamma ray. This unique ability of the detector to measure DOI is put to use for creating a fully 3-D measured system-response. To characterize the 2-D system-response, the detector response had to be measured as a function of the source position in the XY-plane. Initial detector characterizations (specifically the spatial resolution, and DOI studies) were performed with a collimated 662 keV ^{137}Cs source. Since the size of the beam was significant (~ 1.5 mm), the Cs-source was replaced with a 0.25 mm diameter ^{68}Ge source (Sanders Medical Products Inc., Knoxville, TN). The coincidence setup also helped with automatically eliminating the intrinsic LSO background (Figure 3.6). The ^{68}Ge-source was electronically collimated with a 2 x 2 x 10 mm^3 LSO-PMT combination (R3479; Hamamatsu Photonics, Japan) (Figure 6.1). By only considering coincidence events, a finely collimated beam was obtained at the face of the continuous scintillator. The source-LSO-PMT assembly also included the flexibility to adjust the source-crystal distance, thereby varying the beam-size at the detector. The entire assembly was mounted onto a XY translation stage (Velmex Inc., Bloomfield, NY), which could be moved with an accuracy of 0.1 mm. Provision was also made to

pivot the entire source-PMT assembly at arbitrary angles onto the detector surface. To decrease the number of accidental coincidences, a custom-designed lead collimator (0.9" tall, 2 mm bore) surrounded the ^{68}Ge source.

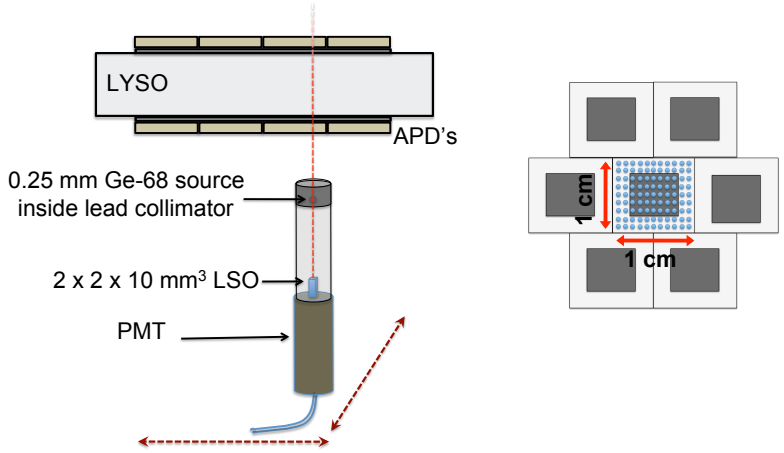

Figure 6.1. Detector calibration: The electronically collimated ^{68}Ge source was used to experimentally measure the detector model. The collimated source was mounted onto a X-Y translational stage and scanned across the face of the detector in 1 mm increments.

To measure the 2-D detector response, the collimated beam was scanned across the face of the detector in 1 mm increments. At each position, each of the individual APD signals, as well as the sum signal was saved. The measured depth-of-interaction parameter was then used to convert the measured 2-D response to a fully 3-D response. To make the model more realistic, gamma-ray attenuation was also incorporated into the model. Detector symmetries could be used to accelerate the 2-D response measurement process. Figure 6.2 illustrates generation of the measured fully 3-D system model.

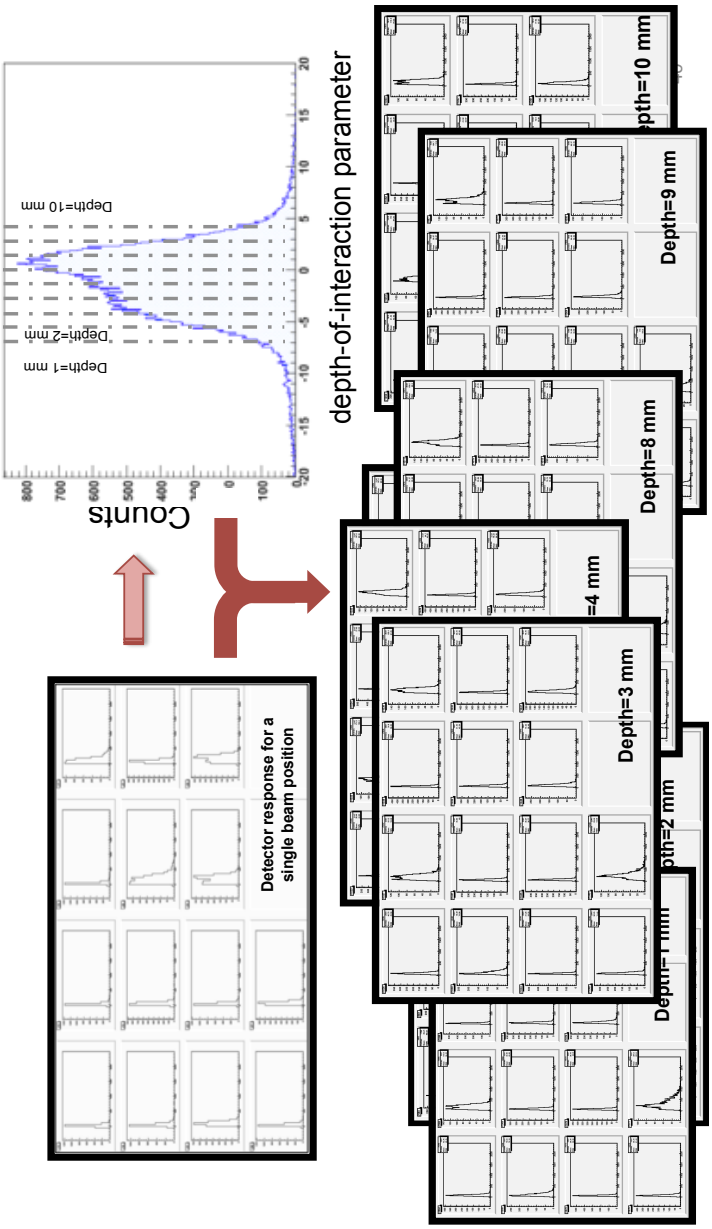

Figure 6.2. An illustration of how the detector calibration data is used to generate a fully 3-D system response. The collimated source is first used to measure the 2-D response from the detector. For each beam position, the measured DOI parameter was then used to decompose the 2-D response into a fully 3-D system model.

6.2.2 Event Reconstruction

Once the fully 3-D system response is measured, the 3-D interaction location and energy for any arbitrary gamma ray incident on the detector can be reconstructed by using the maximum likelihood algorithm. Initially, the reconstruction was performed with a comprehensive search. While a comprehensive search is known to be computationally intensive, the lower number of readout channels offers relief and flexibility. Also there are well known approaches to accelerate the process that can be applied later. For each event, the algorithm computes the likelihood function for all points in 3-D space and chooses the point that gives the maximum likelihood of the data. Due to the poor energy resolution of the current detector (~40% FWHM), results presented here are limited to a single energy window, although in general the energy is an independent free parameter in this method. Figure 6.3 depicts how the algorithm saves the reconstructed 3-D interaction location for any gamma-ray incident on the detector.

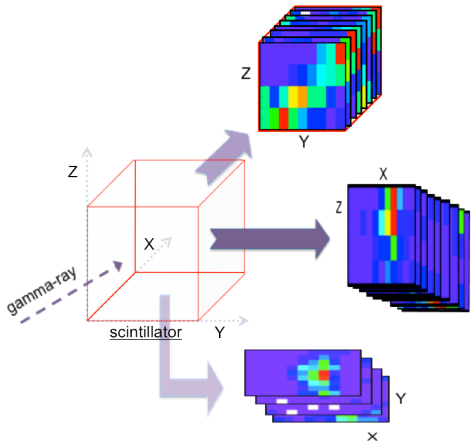

Figure 6.3. An illustration of how the 3D-ML algorithm stores the reconstructed interaction location for any arbitrarily incident gamma ray on the detector. For each gamma ray, the 3-D interaction location is reconstructed using a comprehensive search method. The location is later stored into a corresponding histogram along

the Transverse, Coronal and Sagittal planes i.e. it is stored as a 2-D slices in 3-D space. This provided the flexibility to view the reconstructed interaction locations along any of the image planes: Axial, Sagittal, or Coronal.

6.2.3 Validation

Since this positioning algorithm was recently developed, a careful assessment and validation would definitely be useful before subjecting it to any experimental evaluation. The availability of a validated, fully Monte Carlo GATE model provided this flexibility. The accurate detector model, developed and validated with experimental data (Chapter 5.5.4) was used for this. As described above (Chapter 6.2.1 – 6.2.2), the entire process was realized via simulations. First, the detector 2-D response was measured. This was accomplished by stepping a ^{68}Ge point source in 1 mm intervals across the face of the detector. The scans were repeated over the active area of the detector (~1 x 1 cm^2) (Figure 6.1). For each beam position, ~30,000 gamma rays were generated. As explained before, the detailed simulations tracked both gamma rays and optical photons to provide a realistic estimate of the signal from each APD. Since the primary objective of this exercise was to validate the algorithm itself, the poor packing fraction of the APDs, as well as the electronic noise were ignored. For each beam position, the signal from each of the 14 APDs, as well as the sum of all 14 APDs were used to construct the 2-D system model. An energy threshold of ~400 keV was used. Further, for each beam position, the measured depth of interaction was used to divide the scintillator thickness into 10 depth segments (1 mm each), and a fully 3-D system model was characterized. For a 1 cm^3 of detector, the fully 3-D model had ~1,000 voxels, and 14,000 pdf's. All of the data processing code was developed under the ROOT environment [136] with code written in C/C++. To make the model more practical, the model also accounted for the gamma-

ray attenuation. While a simple exponential distribution could have been sufficient, to make the model more accurate, the attenuation profile was also derived from the GATE simulations. The attenuation model accounted for multiple interactions within the scintillator, and used an energy-weighted positioning scheme to derive the attenuation profile (Figure 6.8).

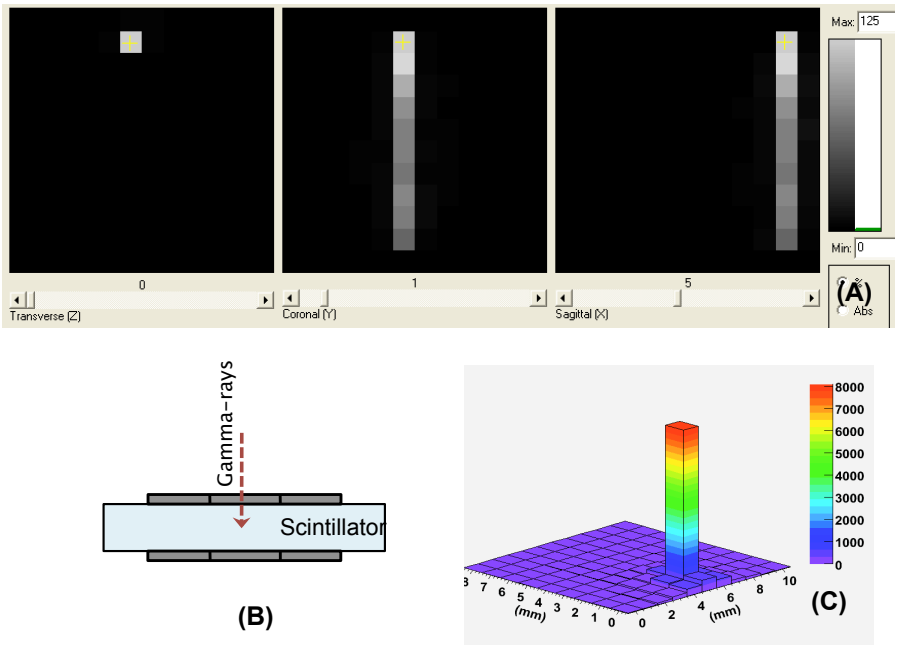

Figure 6.4. Validating the 3D-ML positioning algorithm: The validated Monte Carlo GATE simulation was used to authenticate the capability of the novel 3D-ML positioning algorithm. The entire system model was generated via simulations. The model divided the 10 mm thick scintillator into 10, 1 mm depth segments (1-mm^3 voxels). Shown above is the ability of the 3D-ML algorithm to reconstruct a normally incident beam (B). The histogram of the reconstructed interaction locations can be viewed as (A) Transverse, Coronal and Sagittal slices through the center of the crystal, or as (C) 3-D view of its 2-D projection onto the transverse plane. Since the objective of this exercise was to validate the 3D-ML algorithm, detector sampling and electronic noise were not modeled in these simulations. Note the ability of the algorithm to reproduce the modeled gamma-ray attenuation profile.

To test the reconstruction ability, a separate evaluation dataset was simulated with gamma rays normally incident onto the face of the detector

(Figure 6.4). The 3D-ML algorithm along with the comprehensive search technique was used to reconstruct the interaction locations of the beam. As shown by Figure 6.4, the algorithm not only reconstructed the interaction locations for the beam but also reproduced the incorporated gamma-ray attenuation profile.

6.2.4 First Experimental Evaluations

Since a fully working detector was available, the Monte Carlo validations were succeeded by first experimental evaluations of the 3D-ML algorithm. As illustrated by Figure 6.1, the collimated ^{68}Ge beam was used to measure the detector's 2-D response. The source-PMT distance was adjusted to produce a ~0.75 mm^2 beam spot at the face of the detector. The entire source assembly was then scanned over the face of the detector (~1 cm^2) in 1 mm increments. The readout electronics for the continuous detector is depicted in Figure 5.8. To accommodate the LSO-PMT detector, and generate the coincidence trigger, an additional logic unit was added. Data from the light-sharing detector was collected with a threshold of ~250 keV. At each beam position, ~20,000 gamma rays were collected; individual, and sum signals from all 14 APDs were saved. On an event-by-event basis, the measured depth-of-interaction parameter was then used to convert the 2-D response function to a fully 3-D model. Ten, 1 mm depths were considered and the fully 3-D model had ~1,000 voxels, and 14,000 pdf's. The model also incorporated the gamma-ray attenuation for the beam (described in the preceding section; Chapter 6.2.3).

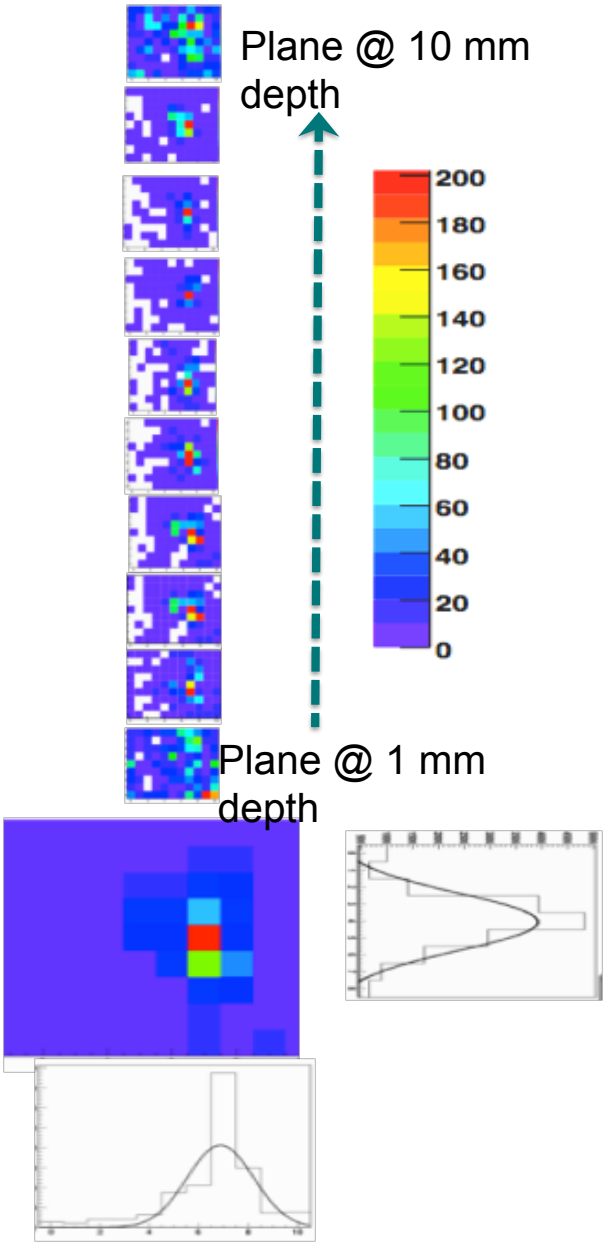

Figure 6.5. First experimental reconstruction of a normally incident beam using the 3D-ML algorithm: Reconstructed 2-D interaction locations layered by the depth at which the interaction location was measured. Also shown is a projection of the entire 3-D volume onto the transverse plane (i.e. the large image shown at the bottom), and Gaussian fits to projections along the X and Y directions.

The experimentally measured 3-D system response was then used to evaluate the 3-D positioning capabilities for gamma rays interacting inside the scintillator. Evaluations were performed with datasets that were separate from ones used to characterize the 3-D system response. To begin with, the ^{68}Ge-collimated beam was positioned normally and near the center of the detector; ~30,000 gamma rays were collected. Data from the detector was processed and collected in a similar manner to measuring the system response i.e. ~250 keV threshold was used on the sum of all 14 APDs, and all 14 individual APD and sum signals were saved to disk. The dataset was further fed to the 3D-ML algorithm. On an event-by-event basis, the 3D-ML algorithm used the measured system model, and a comprehensive search technique to plough through the ~14,000 pdf's (i.e. ~1000 voxels in 3-D space), and find the 3-D location which maximized the likelihood function for the detector (equation 6.5). Figure 6.5 shows the detailed reconstruction results from the experimental reconstruction of a normally incident ^{68}Ge beam near the center of the detector.

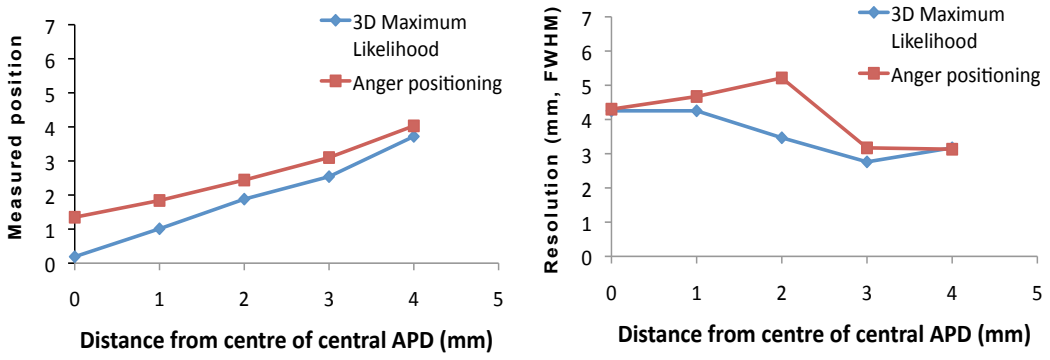

Figure 6.6. A first comparison of how the 3D-ML algorithm compares with traditional Anger-positioning. *Left*: Positioning bias (i.e. deviation of the measured value from its true value). *Right*: Spatial resolution. As expected the ML method has significantly less bias. For both the cases, performance was measured by translating the collimated beam at various locations along the face of the detector.

To characterize the transverse spatial resolution of the detector (along the X-direction) using the 3D-ML algorithm, the collimated ^{68}Ge beam was stepped across the face of the detector in 1 mm increments. At each position ~25,000 gamma-ray events were collected. Data was collected and analyzed as explained above. To calculate the transverse spatial resolution with the 3D-ML algorithm, a Gaussian fit was used on the projection of the reconstructed locations along the transverse direction (Figure 6.5). For a direct comparison, the spatial resolution for the same dataset was also computed using traditional Anger positioning logic and signals from the same 14 APDs. As expected, the 3D-ML algorithm exhibited significantly less bias (i.e. deviation of the measured value from the true value) when compared to using plain Anger-logic (Figure 6.6).

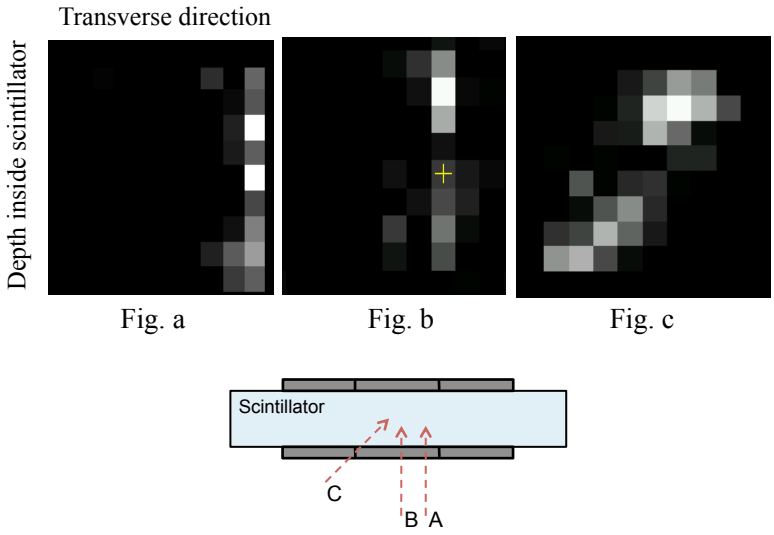

Figure 6.7. Detailed experimental evaluation of the 3D-ML positioning algorithm: The experimentally measured system response (1-mm^3 voxels) was further used to reconstruct interaction locations for varying beam geometries. Images represent, Coronal slice (through the center of the crystal) of the histogram of reconstructed 3-D interaction locations for: Fig. a–b = Normally incident beams at two different locations. Fig. c = an angled beam. The beam locations are illustrated in the bottom cartoon.

While first impressions from the early experimental characterizations were reasonable, further evaluations were necessary, especially to evaluate the DOI-positioning capabilities of the algorithm. This was tested by placing the collimated ^{68}Ge beam at varying locations and angles (i.e. the collimated source assembly was rotated) along the face of the detector. The data was collected and processed in a similar manner discussed above. In addition to analyzing the histograms of reconstructed images (Figure 6.7), the ability of the algorithm to reproduce the modeled gamma-ray attenuation was also tested.

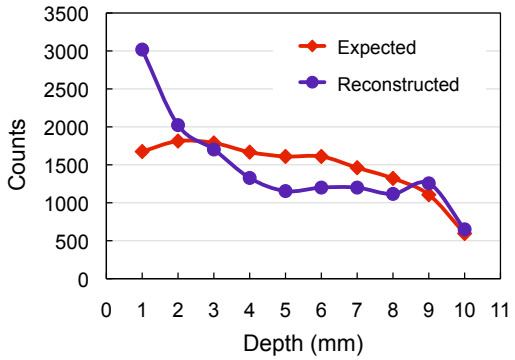

Figure 6.8. Bias with reproducing the modeled gamma-ray attenuation: While the 3D-ML algorithm worked well for certain reconstructions, for others, e.g. Figure 6.7, the reconstructions did not faithfully reproduce the expected depth distribution. Above plot demonstrates this situation. For a single reconstruction, the sum of all counts at that depth was used to demonstrate this.

While the reconstruction algorithm worked well for certain beam positions, for others, it failed to exactly reproduce the modeled gamma-ray attenuation (Figure 6.8). This was analyzed by comparing the expected distribution with the sum of all counts reconstructed at each of the depths inside the scintillator (i.e. a profile of the reconstructed position histogram along the depth direction). As shown above, there seemed to be an apparent bias with

the DOI-positioning capability of the 3D-ML algorithm. The bias was fairly consistent for beams at varying locations and angles (e.g. Figure 6.7).

6.2.5 Investigating, Optimizing Performance of the 3D-ML Algorithm

While first experimental evaluations of the 3D-ML algorithm were encouraging, there were concerns over the accuracy with which the algorithm positioned events along the depth-direction. A systematic and detailed study was essential to understand, and also improve the performance of this novel positioning-algorithm. The validated GATE Monte Carlo model was an invaluable tool to assist with this. Hence the validated GATE model was used for the following purposes:

1. To predict performance of the 3D-ML algorithm under similar experimental conditions.
2. To understand and improve the various factors affecting performance of the 3D-ML positioning algorithm.

6.2.5.1 Investigating Performance with GATE simulations

The entire process, from system-model generation to using the model for evaluations was replicated via GATE simulations. The validated detector model developed in Chapter 5.5.4 was used for this. First, the 2-D detector response was measured by translating a ^{68}Ge point source over the face of the detector (~1 x 1 cm^2) in 1 mm increments. At each position ~30,000 gamma rays were generated. Simulations, after tracking in detail, the gamma and optical photons provided a realistic estimate of the signal from each APD. The signals from each APD were treated in an identical manner as described above (i.e. all 14 APDs used; ~250 keV threshold). For each beam position

the DOI parameter was then used to generate a fully 3-D model (ten, 1 mm depth segments, i.e. a total of ~1,000 voxels and ~14,000 pdfs). Gamma-ray attenuation was also incorporated into the model.

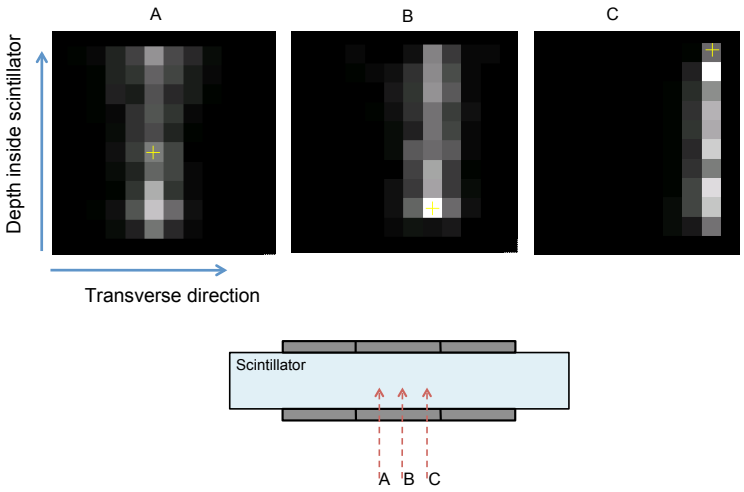

Figure 6.9. Detailed Monte Carlo evaluation of the 3D-ML positioning algorithm: The entire system response (with 1-mm^3 voxels) was simulated using the validated GATE model. It was further used to reconstruct interaction locations for varying beam geometries. Figs. A – C show a Coronal slice (through the center of the crystal) of the histogram of reconstructed interaction locations for normally incident beams at three different locations. The beam locations are depicted in the bottom cartoon.

To evaluate the performance of the algorithm, separate datasets were simulated with gamma rays normally incident onto the face of the detector. The 3D-ML algorithm along with the comprehensive search technique was used to reconstruct the 3-D interaction locations. Figure 6.9 shows the histogram of reconstructed locations (through the center of the crystal) for three different normally incident beams. While the reconstructions worked reasonably well along the transverse directions, the DOI-positioning had a similar bias as observed with the experimental data (Figure 6.8). To further investigate the cause and effects of the miscalculated depth positioning, their error distributions were also examined. This was accomplished by

computing the deviation of the 3D-ML reconstructed location from the true interaction location. To account for the multiple scattering within the scintillator, an energy-weighted position was used to determine the true interaction location. To begin with, the errors (transverse and depth positioning) were computed for a single fixed beam position. The error-distribution histograms (for both transverse and depth-positioning) were well defined and symmetric in nature (Figure 6.10).

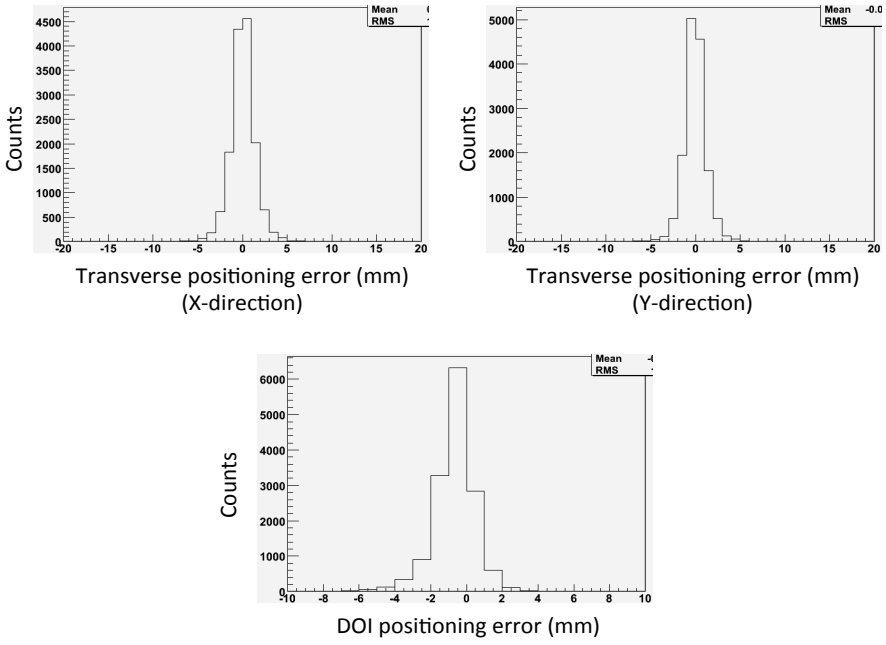

Figure 6.10. 3D-ML positioning-error distributions: For a single beam position, the positioning errors from using the 3D-ML algorithm were histogrammed. The error-distributions were estimated along both, the transverse and depth directions.

The error histograms were also used to calculate the predicted DOI-resolution for the detector. To calculate the DOI-resolution, the ^{68}Ge source was stepped across the face of the detector in 1 mm increments. At each position a Gaussian fit to the error histograms yielded the DOI-resolution (Figure 6.11).

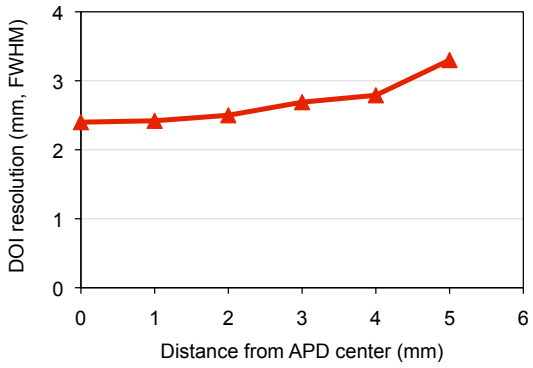

Figure 6.11. DOI-resolution for the detector estimated using Monte Carlo simulations: For each beam position, a Gaussian fit to the positioning errors (Figure 6.10) from using the 3D-ML algorithm was used to estimate the DOI-resolution.

Apart from predicting DOI-resolution over the face of the detector (i.e. over the transverse plane), the simulations were also used to explore in detail the DOI-resolution as a function of the depth-of-interaction inside the scintillator (i.e. at different depths over the transverse plane of the scintillator). This study was performed to evaluate potential pitfalls arising from the poor packing fraction of the current detector (Figure 5.3). As before, a Gaussian fit was used with each of the error histograms (10 depths for each beam position) to compute the DOI-resolution (Figure 6.12). A similar detailed study of the transverse spatial resolution (Figure 6.13 - Figure 6.14), as well as the "cumulative 3-D" positioning error was also performed (Figure 6.15). Since, the GATE simulations are computationally intensive and time consuming, the above detailed evaluations were only performed for one half of the detector (symmetry assumed to carry over results for the other half). The simulations predicted an average DOI resolution of ~3 mm FWHM and was best near the center of the APD. While this is contrary to the transverse spatial resolution, it can be attributed to the complete sampling of the light distribution for events interacting near the center of the APD.

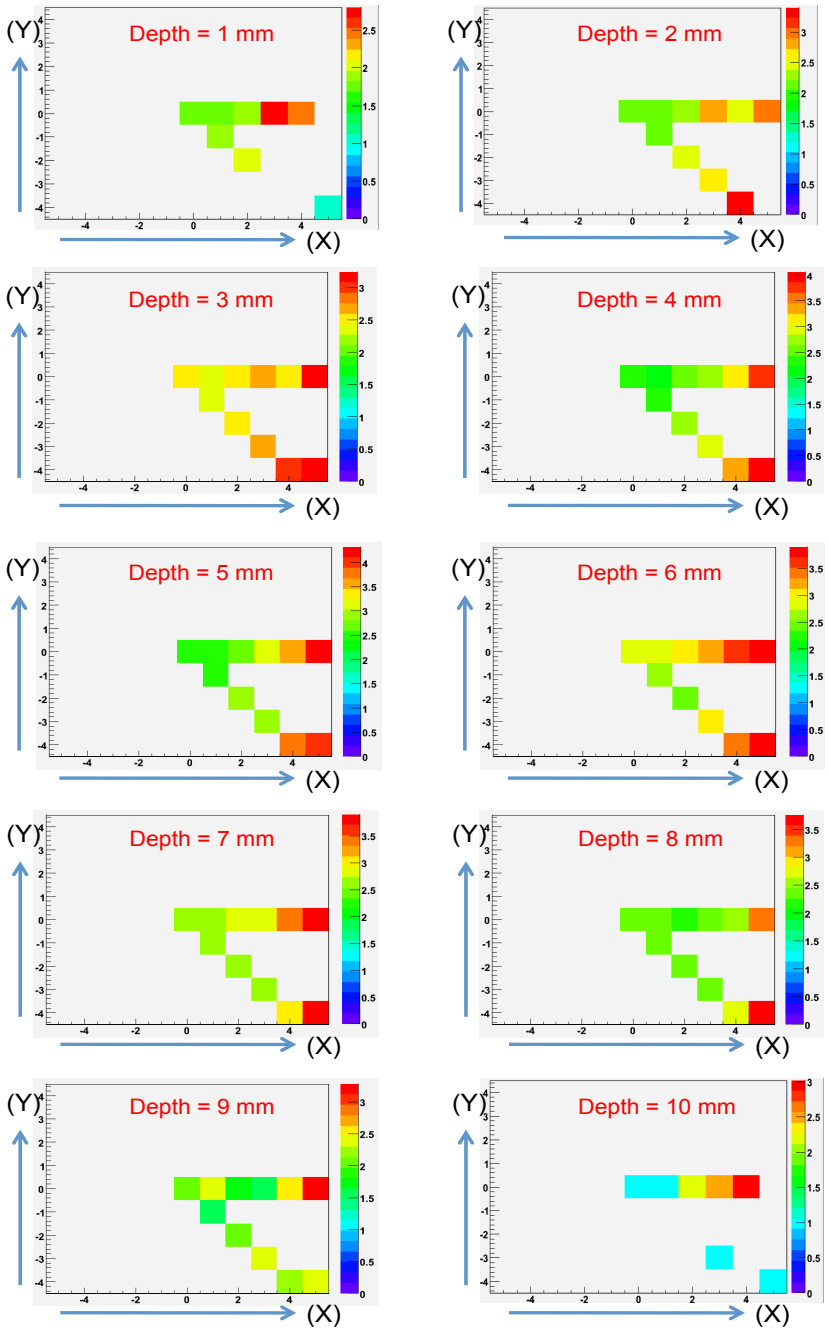

Figure 6.12. Analysis of the DOI-resolution using simulations: Shown is the DOI-resolution (mm, FWHM) over the transverse plane, and at various depths inside the scintillator.

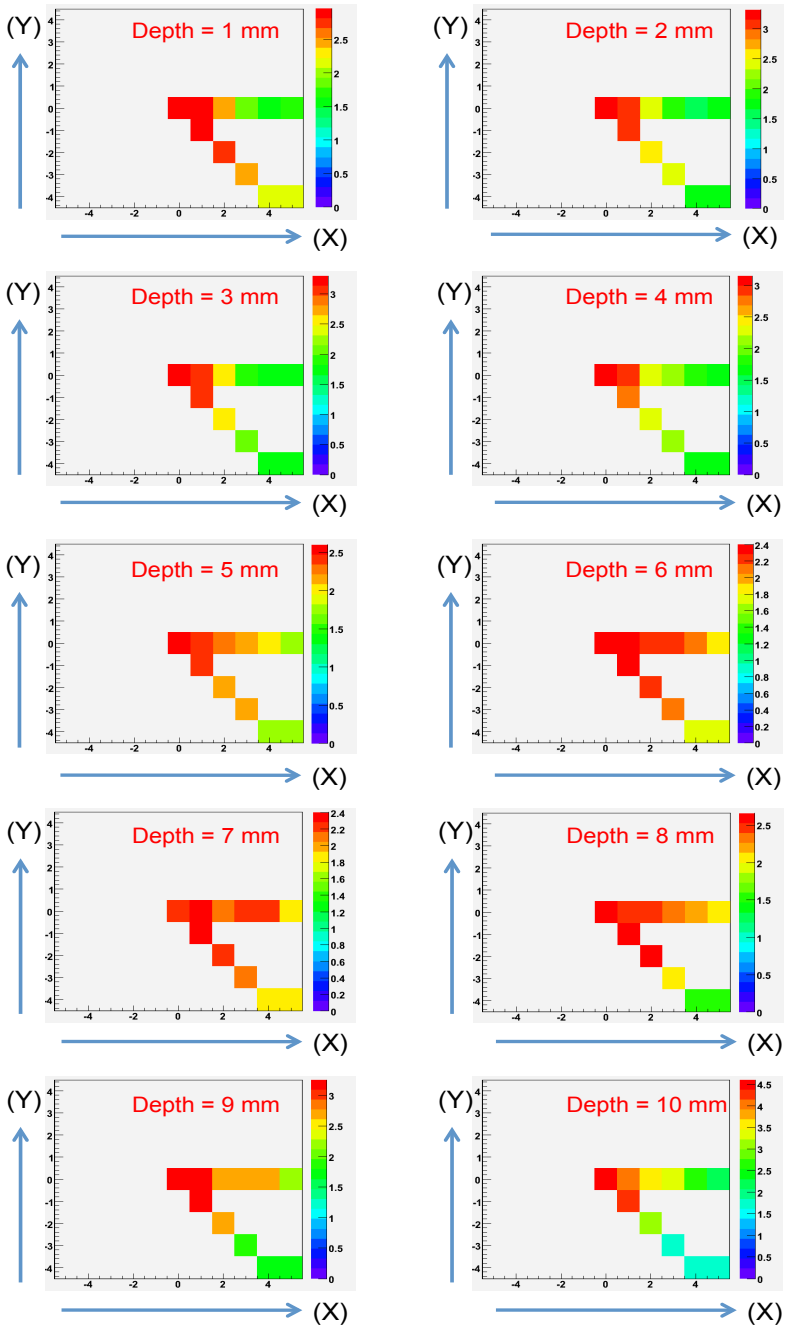

Figure 6.13. Analysis of the transverse spatial resolution (along the X-direction) using simulations: Shown is the transverse spatial resolution (mm, FWHM) over the transverse plane, and at various depths inside the scintillator.

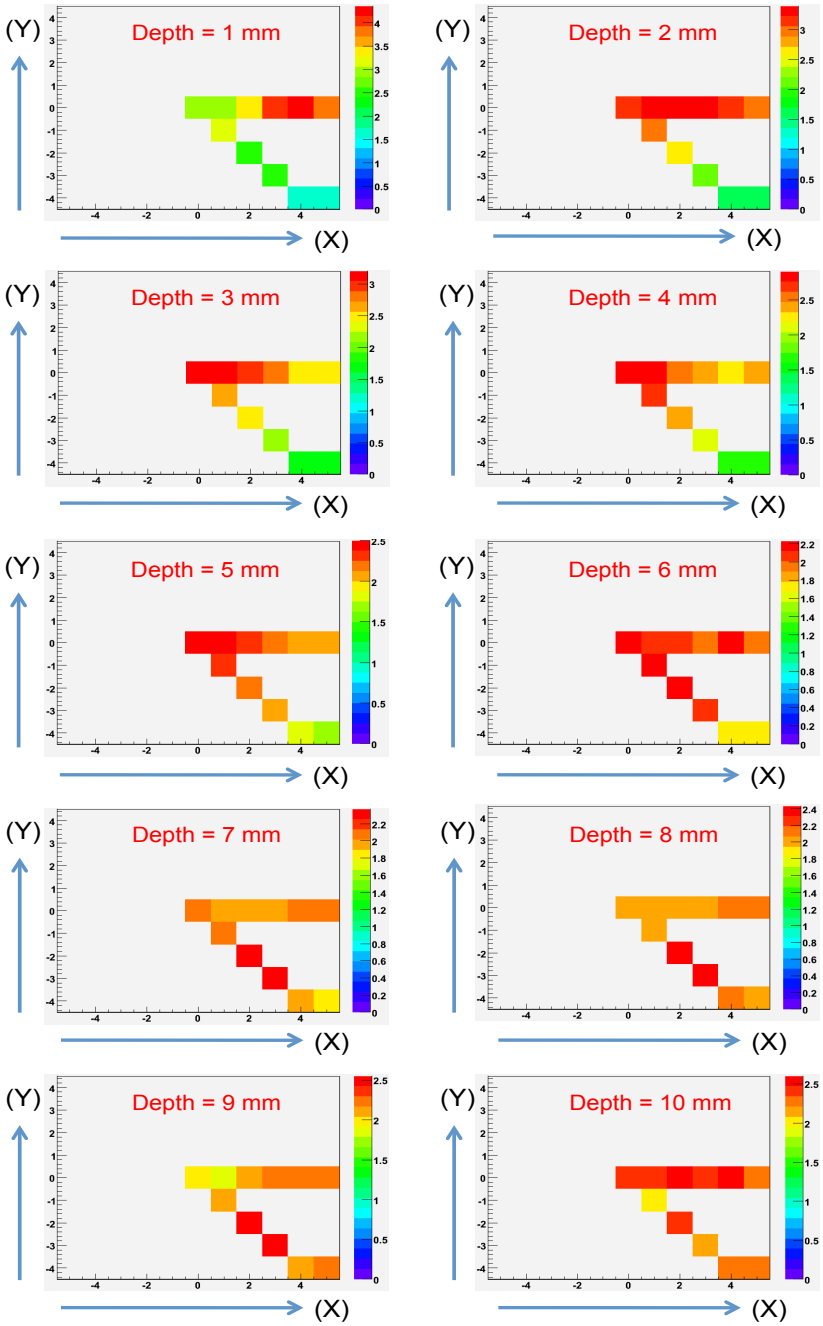

Figure 6.14. Analysis of the transverse spatial resolution (along the Y-direction) using simulations: Shown is the transverse spatial resolution (mm, FWHM) over the transverse plane, and at various depths inside the scintillator.

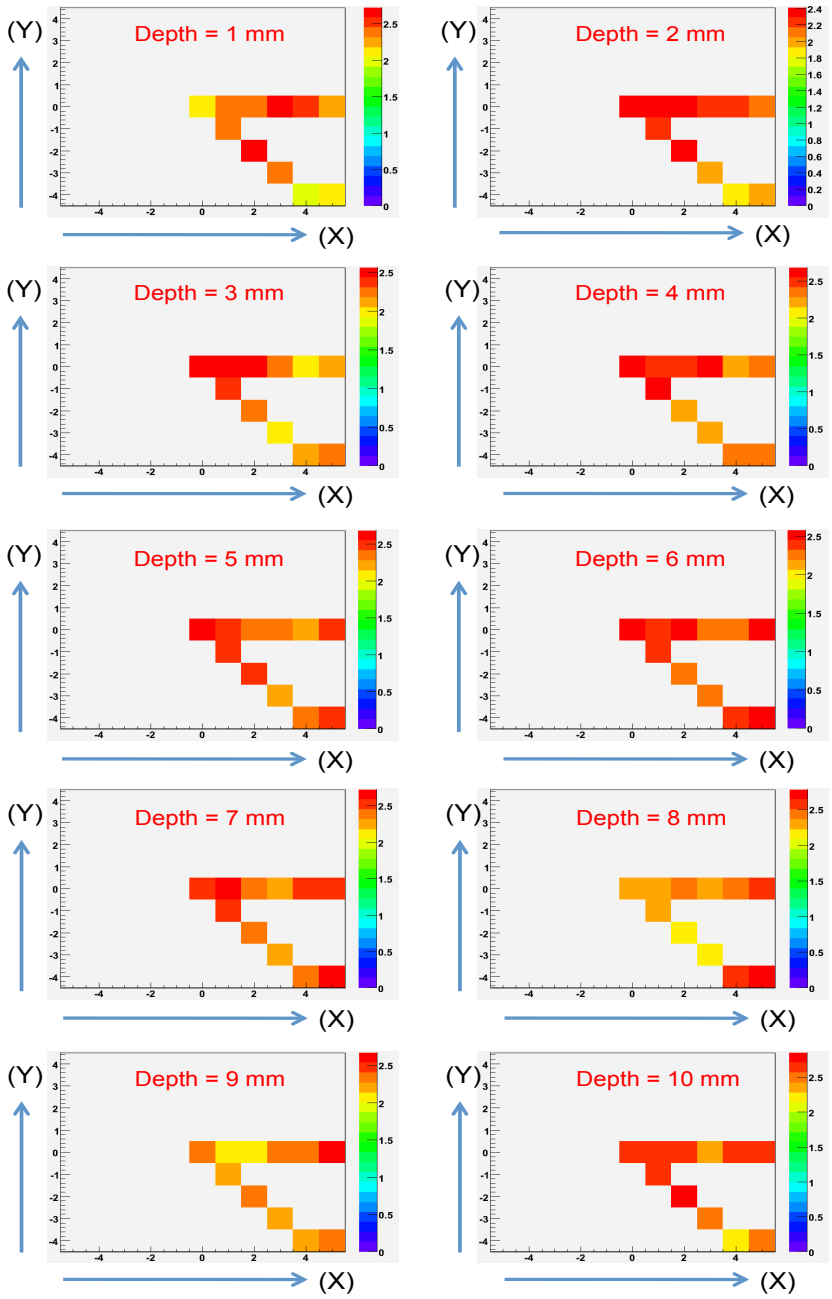

Figure 6.15. Analysis of the cumulative "3-D" resolution using simulations: The cumulative error was calculated by computing the Euclidian distance between the measured and true interaction locations in three-dimensional space. Shown are results over the entire transverse plane and at various depths inside the scintillator.

6.2.5.2 Factors affecting 3D-ML performance

Reconstructions with the 3D-ML algorithm were encouraging but being new, there was a definite need to first understand and later improve the various factors that affected its performance. The validated GATE Monte Carlo simulations offered a convenient method to test and evaluate this. The various factors affecting performance included:

6.2.5.2.1 Statistical accuracy of the system model

With a measured model, there is always a practical limit on the amount of statistical noise (arising from counting statistics) that is present in the system. This is directly reflected as noise in the system model (i.e. individual APD pdf's; top row of Figure 6.16).

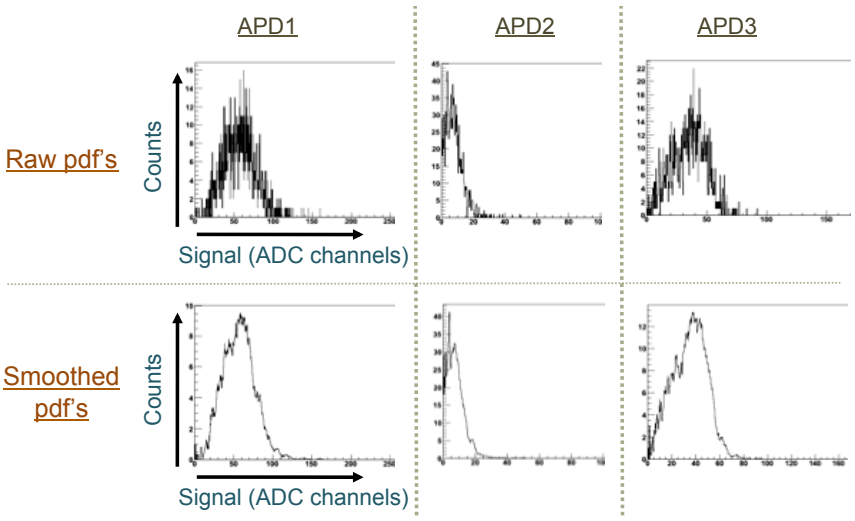

Figure 6.16. Statistical accuracy of the system model: To mitigate the statistical noise in the system-model arising from the finite 'source' counting statistics, a nonlinear smoothing algorithm was developed. Each of the pdf's was processed with a rectangular smoothing kernel with a window size directly proportional to the error expected from the photostatistics. Shown are representative pdf's. *Top row*: Unprocessed pdf's from the detector (simulations). *Bottom row*: Corresponding pdf's after smoothing.

An alternative way (first being counting longer; has practical limits) to decrease the statistical noise is by using a filter having an appropriate cut-off frequency (complicated by the large dynamic range of the pdf's). Hence, to alleviate the statistical noise in the system model, a nonlinear smoothing scheme was devised. The algorithm utilized a rectangular smoothing kernel whose width was directly proportional to the amount of photostatistical noise expected for any particular pdf. Sample spectra before and after smoothing are shown in Figure 6.16.

6.2.5.2.2 Modeling gamma-ray attenuation

Efforts were previously devoted to accurately model the gamma-ray attenuation in this detector. But the poor packing fraction of the detector meant that the gamma-ray attenuation seen by the detector varied with beam position and thus was different from the actual, modeled attenuation profile. It was observed that the performance of the detector was very sensitive to the modeled gamma-ray attenuation.

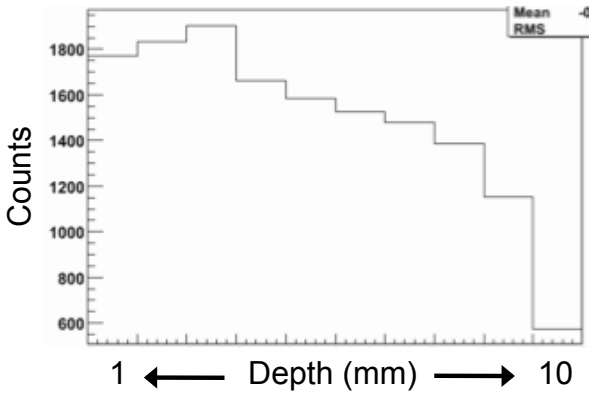

Figure 6.17. Accurately modeling gamma-ray attenuation: Due to the relatively poor sampling of this detector, the actual gamma-ray attenuation, as seen by the detector, differed from the previously modeled profile (Figure 6.8).

6.2.5.2.3 Energy of the gamma-ray

For any gamma-ray interaction, the detector response is dependent on both the 3-D interaction location and energy deposited by the gamma ray. Hence it is imperative that the energy of the gamma ray be known (Figure 6.18).

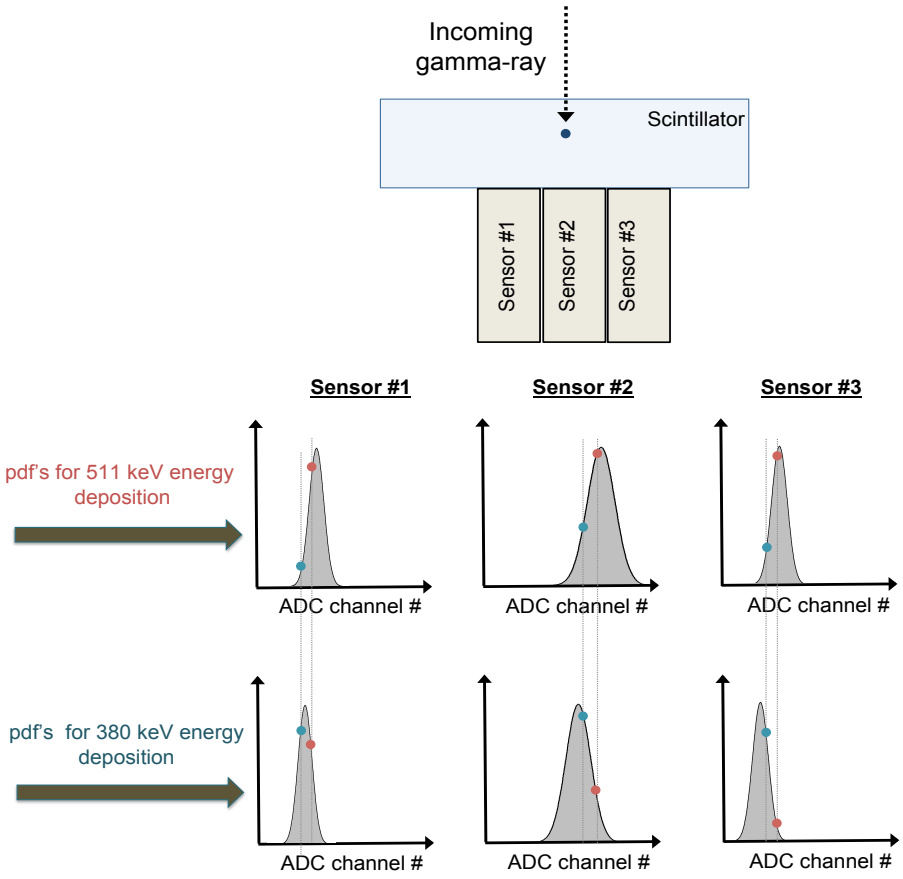

Figure 6.18. A simplified cartoon, illustrating the importance of correctly including the energy of the gamma ray for the 3D-ML algorithm. *Top row*: Continuous scintillator detector readout by three noiseless photosensors. *Middle row*: Sensor pdf's when the photon deposits all of its energy (511 keV) inside the scintillator. *Bottom row*: Sensor pdf's when the gamma ray deposits 380 keV at a slightly different, but relatively close location. The variation in the deposited energy blurs the pdf's (and, consequently the position information) and need to be accounted for. Note: In reality, noise (both statistical and electronic) worsens the blur in the pdf's and consequently the position.

As shown in Figure 6.18, consider two photons depositing varying energies at different depths, but in the vicinity of each other. If the energies are unaccounted, the varying DOI (in this case) creates an ambiguity for the ML algorithm to estimate the true 3-D interaction location. Note: Intuitively one would assume that the pdf's could be scaled with the energy, but the noise in the pdf's do not scale in a similar fashion. Hence, an accurate estimation of the gamma-ray energy should help the algorithm in identifying the true interaction location.

6.2.5.2.4 Light-collection efficiency

The poor packing fraction of the APD affected the light collection efficiency. In addition to affecting the energy and timing performances, the spatially varying light collection efficiency (Figure 6.19) further distorted the actual gamma-ray attenuation seen by the detector.

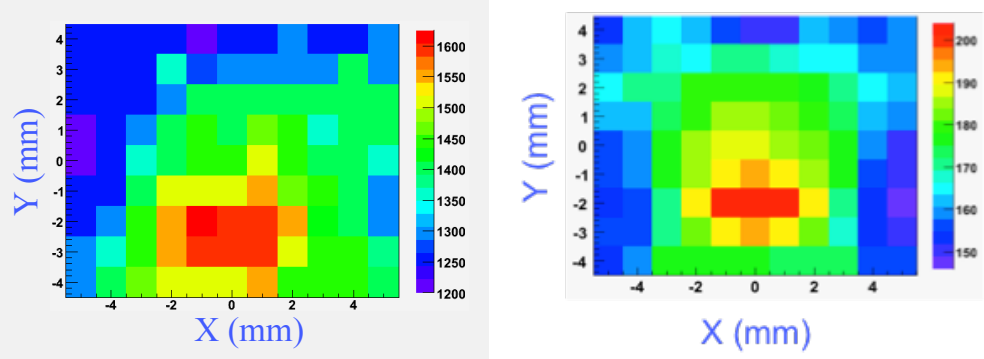

Figure 6.19. A 2-D map of the light collection efficiency across the face of the detector. *Left*: experimental results. *Right*: Simulation results. For both the cases, a 511 keV ^{68}Ge source was stepped across the face of the detector and the photopeak information from the sum of all 14 APDs was used to generate the data.

6.2.5.2.5 Detector Stability and Drifts

The steady and optimal performance of the detector, both over the long and short term is important for this design. More so, because the detector response model once measured can continue to be used until any changes are made to the detector operating conditions (e.g. detector bias voltage, operating thresholds). But, as APDs are temperature sensitive devices, they are susceptible to drifts in gain. Hence, it is important to monitor and correct for any possible drifts that occur with temperature and time. This includes the detector and also the associated read-out electronics.

6.2.6 Performance Evaluation

Chapter 6.2.5 helped provide a better understanding of the working of the 3D-ML positioning algorithm. It also provided an estimate of the expected DOI resolution from the detector. Armed with the above facts, experimental evaluation with an improved 3D-ML algorithm was performed. Critical modifications included:

1. An accurate modeling of the gamma-ray attenuation information in a position-dependent manner.
2. In keeping with the expected DOI resolution of ~3 mm FWHM, 4 depth segments (each 2.5 mm deep) were chosen rather than the 10 segments previously used. The reduced number of depth segments helped improve the statistical quality of the data.

Since the current evaluations were improvements merely at the data processing level, it was decided to make use of the previously measured 2-D response function (Chapter 6.2.4). Further, four 2.5 mm depth segments

were used, and a fully 3-D model consisting of ~400 voxels and ~5600 pdfs (for the same 1 cm^3 volume of scintillator) was generated.

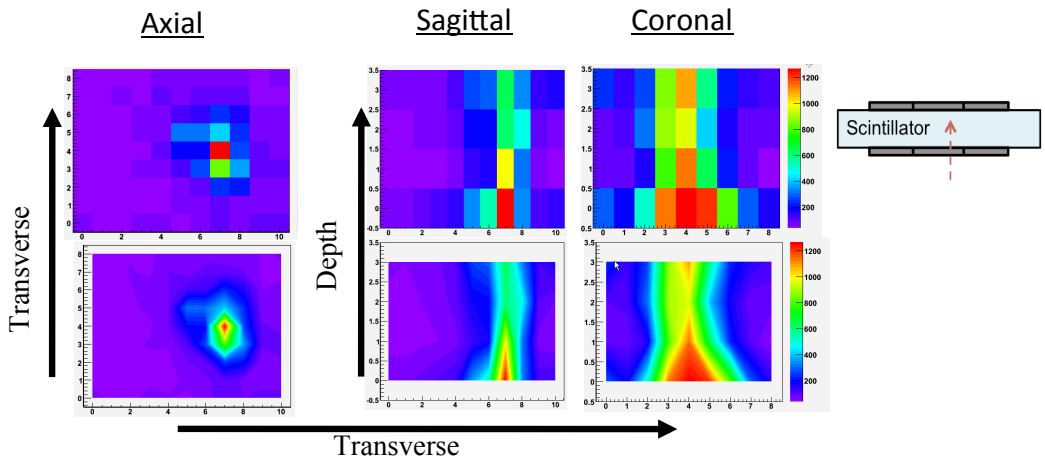

Figure 6.20. 3D-ML reconstruction for a normally incident beam near the center of the detector: *Top row*: 2-D projection of the 3-D event reconstruction histograms along the Transverse, Sagittal and Coronal planes. *Bottom row*: smoothed version of the corresponding image above it. Each depth segment measured 2.5 mm, and each reconstructed voxel measured 2.5 mm^3.

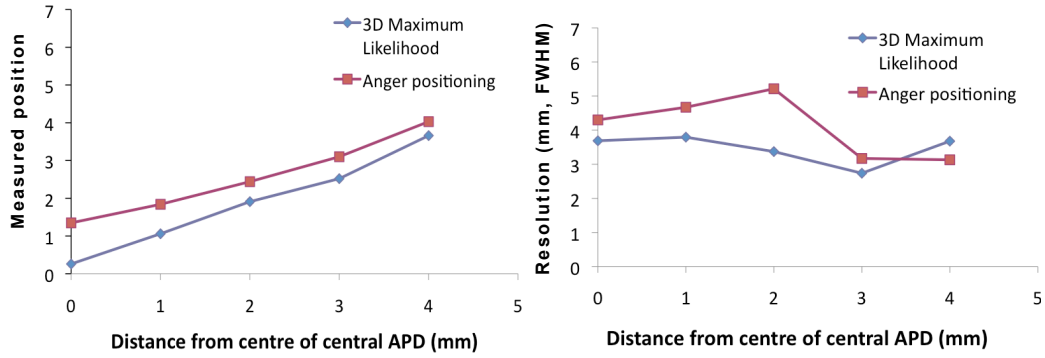

Figure 6.21. Comparison of how the improved 3D-ML positioning algorithm compares with traditional Anger-positioning. *Left*: Positioning bias (i.e. deviation of the measured value from its true value). *Right*: Spatial resolution.

Figure 6.20 shows a projection of the histogram(s) of reconstructed interaction locations for a normally incident beam near the center of the detector. Next, the transverse spatial resolution of the detector was characterized using the improved 3D-ML algorithm. The datasets collected previously (Chapter 6.2.4) were used for this. For comparison purposes, the datasets were also processed using traditional Anger-logic. As expected, the 3D-ML algorithm exhibited lesser bias, when compared to simple Anger-positioning (Figure 6.21).

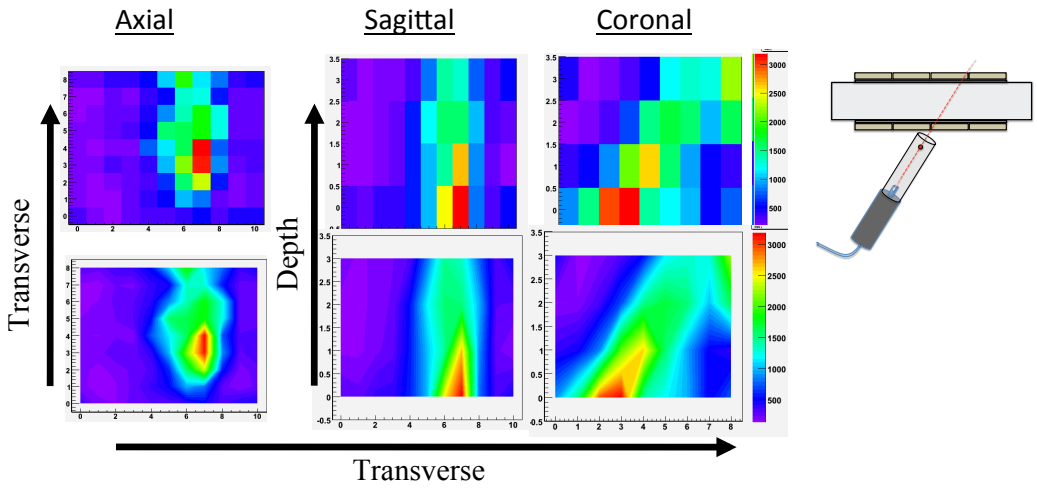

Figure 6.22. Performance of the 3D-ML positioning algorithm when presented with an angled beam (30°): *Top row*: 2-D projections of the 3-D event reconstruction histograms along the Transverse, Sagittal, and Coronal planes. *Bottom row*: smoothed version of the corresponding image above it. Each depth segment measured 2.5 mm, and each reconstructed voxel measured 2.5 mm^3.

Further studies to evaluate the DOI-positioning capability of the algorithm were performed by angling the beam onto the face of the detector. The collimated source assembly was first inclined at an angle of 30° and the resultant data was processed using the 3D-ML algorithm (Figure 6.22). Later, another dataset was acquired with the beam at 45° and was also processed using the 3D-ML algorithm (Figure 6.23). In addition to analyzing the

histograms of the reconstructed interaction locations, the ability of the algorithm to reproduce the modeled gamma-ray attenuation was also examined. This was evaluated by comparing the expected distribution (i.e. modeled gamma-ray attenuation) with the sum of all counts reconstructed at each of the 4 depth segments inside the scintillator (i.e. a profile of the projection of reconstructed position histogram along the depth direction). As shown by Figure 6.24, the algorithm reproduced the incorporated gamma-ray attenuation fairly well.

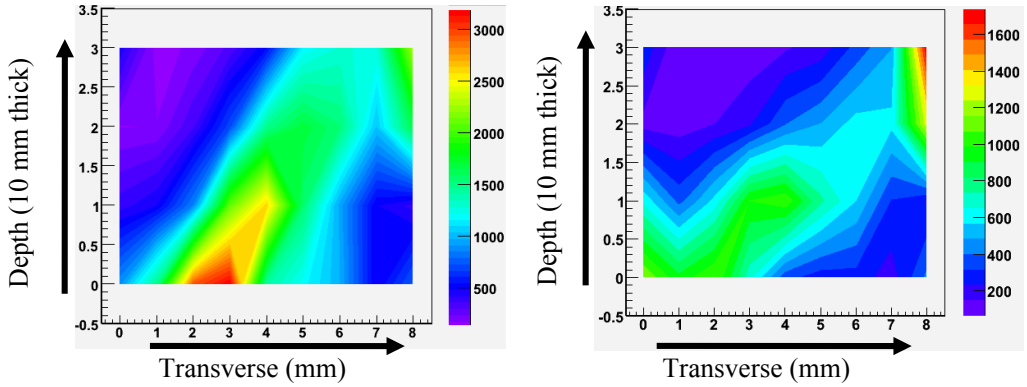

Figure 6.23. Comparison of the 3D-ML reconstruction for two separately inclined gamma-ray beams: 30° (left), and 45° (right). Data obtained from experiments with the collimated ^{68}Ge beam.

To summarize, Figure 6.25 shows a comparison of reconstructed interaction locations for a normally incident and angled beams in the presence and absence of DOI encoding.

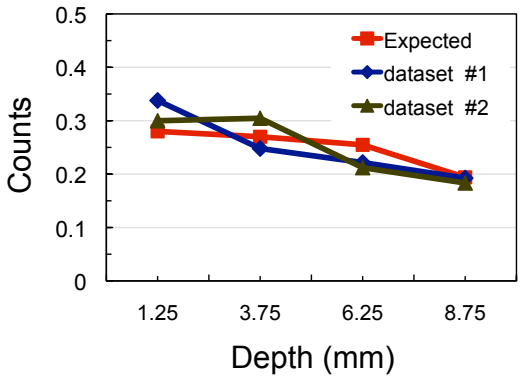

Figure 6.24. Accurately positioning events at various depths along the length of the scintillator: Proof that the improved 3D-ML algorithm accurately positions events at various depths along the length of the scintillator. For each beam position the sum of all counts at a particular depth was used. Data obtained from 3D-ML reconstruction performed in Figure 6.23.

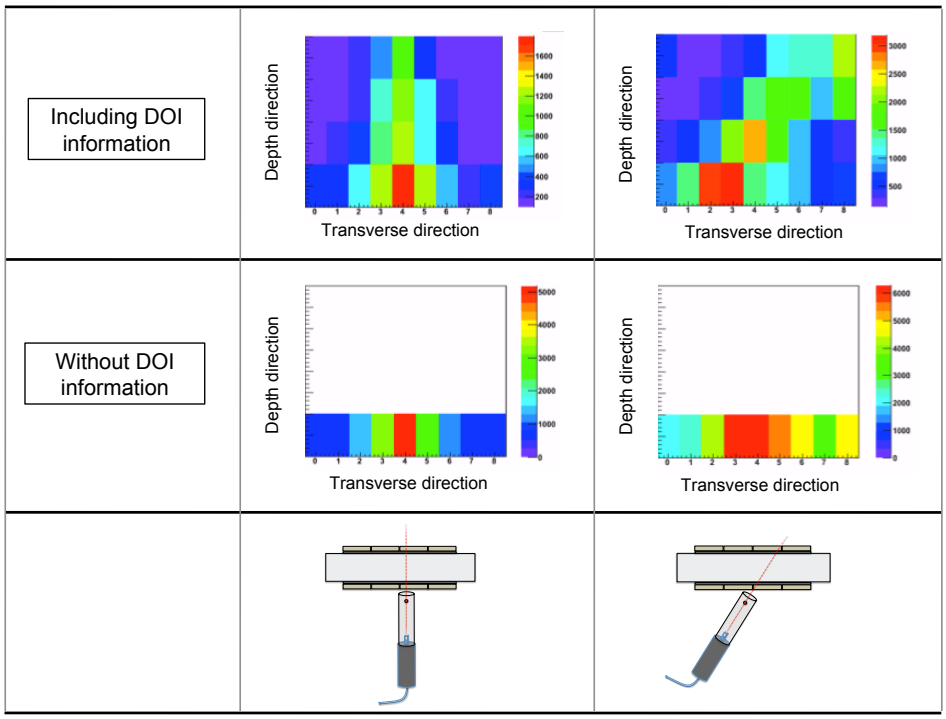

Figure 6.25. Summary of 3D-ML reconstruction for experimental data from normal and obliquely incident gamma-ray beams: Also, shown for comparison is the 3D-ML reconstruction in the absence of DOI decoding. In the absence of DOI-information, all the events were assumed to interact at the entrance face of the scintillator.

6.2.7 Experimental characterization of the DOI resolution

The preceding sections of this chapter have presented and reasonably concluded the functioning of a novel, maximum likelihood based 3-D event positioning algorithm. While its real power would only be evident in a real imaging scenario, it could nevertheless be immediately put to use for experimentally measuring the DOI-resolution of the detector.

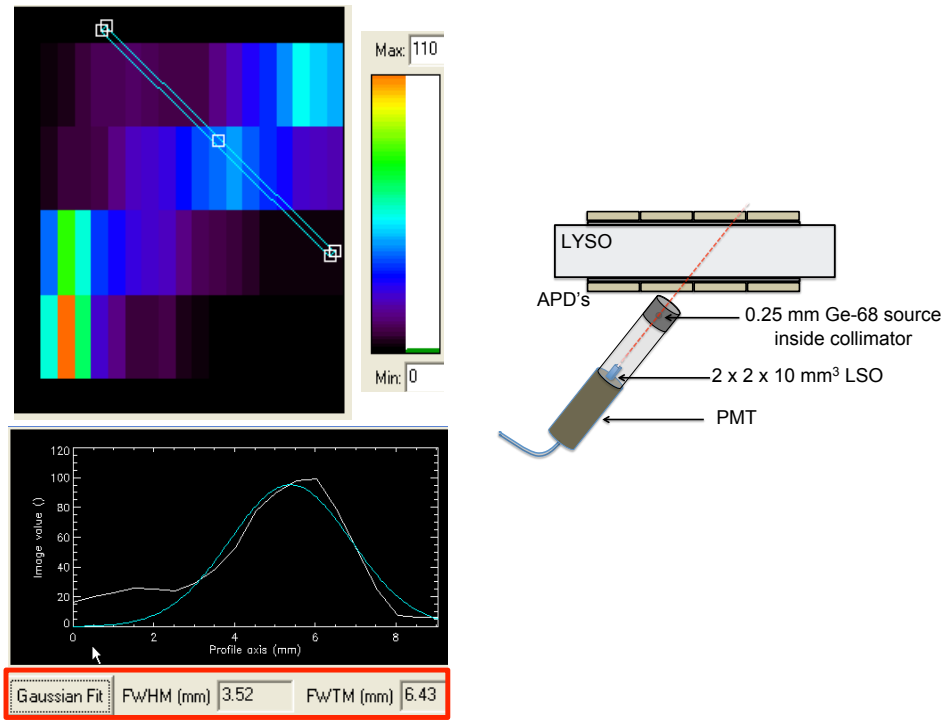

Figure 6.26. DOI was experimentally measured with the collimated beam aimed at the detector an angle of 30°. As before, the 3D-ML algorithm was used to reconstruct the interaction locations inside the scintillator. Figure shows the histogram of the reconstructed interaction locations for a single slice through the center of the crystal. Profiles were drawn normal to the beam incidence angle and a Gaussian fit was used. After accounting for the beam size (0.75 mm), a DOI resolution of 3 – 4 mm FWHM was measured.

To measure the DOI-resolution, the collimated beam was angled onto the face of detector at 30°. The 3D-ML algorithm was then used to reconstruct the 3-D interaction locations inside the scintillator. Figure 6.26 shows a histogram of the reconstructed interaction locations for a single slice through the center of the crystal. Profiles were drawn normal to the incident beam and a Gaussian fit was applied. This was performed with the MicroPET ASI Pro software (formerly sold by CTI Molecular Imaging Inc., now part of Siemens Molecular Imaging; v.6.2.4.0, [191, 192]) that is routinely used to perform image analysis on PET images acquired from the commercially available MicroPET small animal scanner. To satisfy the spatial sampling requirements of the software, a bilinear interpolation (along the X and Y directions) was separately performed prior to the fitting procedure. After taking into account the size of the beam, a DOI resolution of 3 – 4 mm FWHM was measured.

7. Conclusion, Discussion, and Future Work

Spatial resolution in positron emission tomography (PET) has steadily improved over the years, but remains substantially worse than in other imaging modalities, currently at ~2 mm best case for most commercial systems. This is a serious limitation particularly for imaging mice, which have great potential in preclinical PET research largely because of their compatibility with genetic manipulation. Current approaches to improve spatial resolution and sensitivity have performance trade-offs.

This thesis demonstrates the potential of a novel light-sharing gamma-ray detector in providing a cost-effective solution for high performance PET. When compared with conventional PET detectors, it can improve spatial resolution without sacrificing sensitivity. Also, with its ability to measure the depth-of-interaction of the gamma ray, it can help reduce parallax errors in a scanner, an ability most PET scanners lack. The novel detector comprises a single continuous slab of scintillator read out by large-area solid-state photosensors on both sides. Apart from eliminating the costs arising from manufacturing the scintillator arrays, it further reduces costs by making use of a smaller number of readout elements. Also, by making use of solid-state photosensors, the detector design is in principle a MRI compatible detector, facilitating simultaneous PET-MRI.

Primary work involved designing, building, and demonstrating feasibility for this novel detector. While most conventional continuous scintillator

detectors are readout with photomultiplier tubes, the use of solid-state avalanche photodiodes (APDs) necessitated careful optimizations of the electronic noise as well as detector signal-to-noise ratio. While feasibility is successfully demonstrated, it involved the following specific tasks:

a. Building an initial prototype detector and thoroughly investigating its performance.
b. Performing detailed detector optimization to improve the initial detector design.
c. Implementing the detector optimizations for building an improved prototype detector.

In parallel, a fully Monte Carlo model for the detector was also developed and validated with experimental results from the improved prototype.

To utilize the fullest potential of this class of detectors, a novel, maximum likelihood based 3-D event-positioning algorithm was also developed and experimentally evaluated on the improved prototype detector.

The final detector design consisted of a 10 mm thick, 60 mm diameter LYSO crystal, read out with 14 large-area APDs from Hamamatsu (S8664-55; 5 x 5 mm^2 active-area) i.e. 7 APDs on each side of the scintillator. The detector was read-out with off-the-shelf electronics (eV-9053 pramplifiers) offering the lowest electronic noise.

Detailed experimental characterizations of the improved prototype detector provided a transverse spatial resolution and depth resolution of ~3 mm FWHM.

While efforts here were devoted to demonstrate feasibility for the approach, the detailed detector optimizations and validated Monte Carlo model have

already laid the foundations for future work. The Hamamatsu S8664-55 APDs were primarily chosen to economically expedite building of a proof-of-concept detector. The Perkin Elmer APDs have shown to have lower noise (~25%), and also better packing fraction (x2). Both of these should directly improve performance for a next generation APD based detector. The validated GATE model was used to evaluate the performance benefits of an optimized detector utilizing an APD similar to the Hamamatsu S8665, but with almost 100% active area (Figure 7.1).

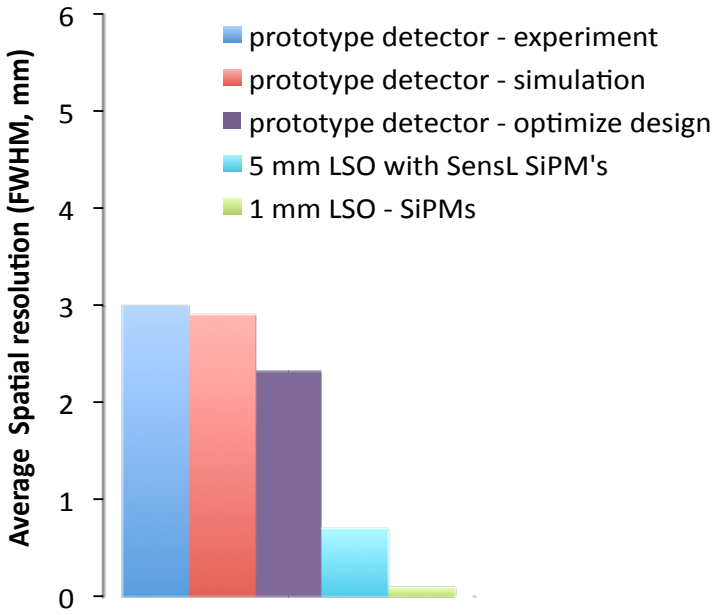

Figure 7.1. Improving the detector spatial resolution: The validated GATE Monte Carlo model was used to optimize detector design.

Silicon photomultipliers (aka SiPM/MPPC) are even better suited for this approach. They provide huge gains and fast response, while retaining many of the desirable properties that solid-state devices have. Recently, a 4 x 4 array of 9 mm^2 SiPMs has become available from SensL (SensL, Cork, Ireland). The array while not being appropriately sized to read out a 10 mm thick scintillator, was reasonably sized for a 5 mm thick scintillator.

Additionally, the spatial resolution in this design directly scales with the light-spread function; a thinner scintillator providing higher spatial resolution (Figure 7.1). Validated Monte Carlo simulations also predict a spatial resolution < 1 mm for a 5 mm thick LYSO scintillator readout by the SensL SiPM arrays (Figure 7.1).

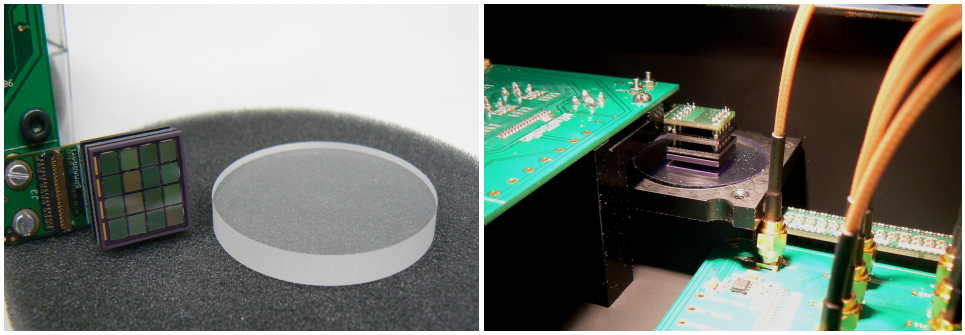

Figure 7.2. *Left*: The scintillator (5 mm thick and 4 cm diameter LYSO slab) and the SiPM array (4 x 4 array of 3 x 3 mm^2 pixels; SensL) used to build a second-generation light sharing detector. *Right*: The assembled detector (in the center of he picture) and the associated front-end electronics used to read-out the detector.

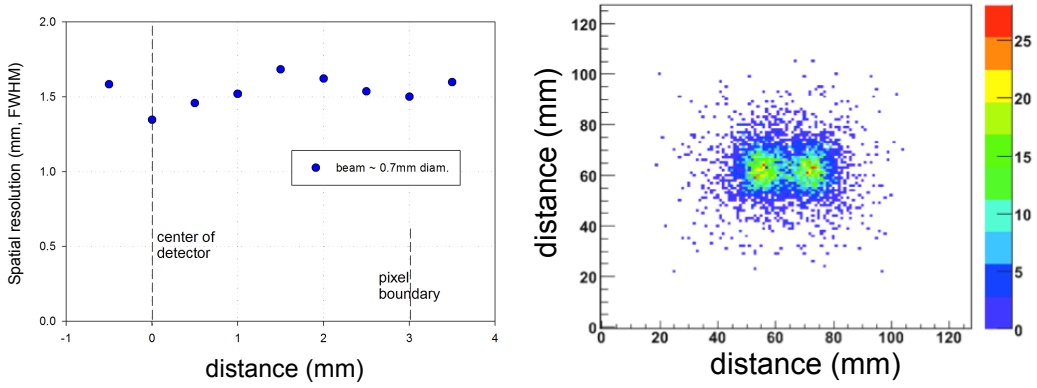

Figure 7.3. *Left*: Preliminary spatial resolution measurements with a next generation light-sharing detector that uses a 5 mm thick LYSO scintillator disk and arrays of 3 x 3 mm^2 SiPMs from SensL. *Right*: Two dimensional reconstruction for two separately collimated (beam size ~0.7 mm^2) ^{68}Ge beams positioned 2 mm apart. Data was generated by superimposing two separate data sets positioned 2 mm apart. Simple Anger-positioning was used to reconstruct the position for both the beams. Note: Spatial resolution measurements include contributions from the beam (~0.75 mm)

While the details for the SiPM based detector (with a 5 mm thick LYSO scintillator) would not be discussed here, preliminary experimental measurements (Figure 7.2, Figure 7.3) [193] have already demonstrated a transverse spatial resolution of ~1.3 mm FWHM; timing resolution of ~4 ns FWHM; and energy resolution of ~20% FWHM. These are significant improvements over the proof-of-concept Hamamatsu APD detector.

While the ultimate goal is the realization of a compact, high-performance, small animal scanner (Figure 7.4), there is still plenty of scope for investigation and improvement. These include developing optimal trigger algorithms optimized for obtaining best timing, spatial, energy, and count-rate performance. For example, using groups of 4 or even 3 photodetectors per side might be desirable – while the smaller number would reduce the electronic noise, the reduced area might prevent full light collection and introduce further non-uniformities in positioning performance. The development of a two-headed prototype, or a large-area planar detector are possible next steps.

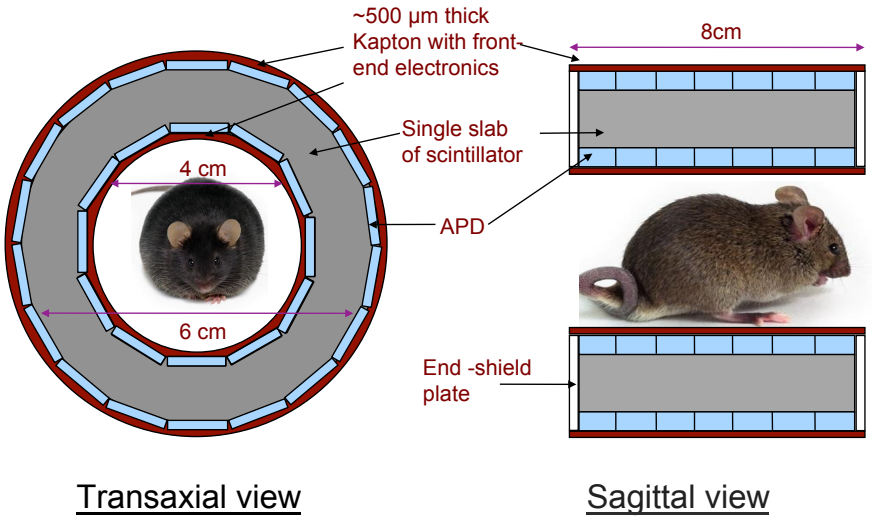

Figure 7.4. Conceptual layout for a future small animal scanner utilizing a single continuous scintillator.

Bibliography

[1] H. Karbe, V. Holthoff, M. Huber, K. Herholz, K. Wienhard, R. Wagner, and W. D. Heiss, "Positron emission tomography in degenerative disorders of the dopaminergic system," *J Neural Transm Park Dis Dement Sect,* vol. 4, pp. 121-30, 1992.

[2] S. P. Hume and R. Myers, "Dedicated small animal scanners: a new tool for drug development," *Curr Pharm Des,* vol. 8, pp. 1497-511, 2002.

[3] J. L. Wang and L. Maurer, "Positron emission tomography: Applications in drug discovery and drug development," *Current Topics in Medicinal Chemistry,* vol. 5, pp. 1053-1075, 2005.

[4] C. C. Meltzer, J. T. Becker, J. C. Price, and E. Moses-Kolko, "Positron emission tomography imaging of the aging brain," *Neuroimaging Clin N Am,* vol. 13, pp. 759-67, Nov 2003.

[5] E. M. Rohren, T. Turkington, and R. E. Coleman, "Clinical Applications of PET in Oncology," *Radiology,* vol. 231, pp. 305-332, 2004.

[6] S. Weber and A. Bauer, "Small animal PET: aspects of performance assessment," *European Journal of Nuclear Medicine and Molecular Imaging,* vol. 31, pp. 1545-1555, Nov 2004.

[7] S. R. Cherry, "In vivo molecular and genomic imaging: new challenges for imaging physics," *Physics in Medicine and Biology,* vol. 49, pp. R13-R48, 2004.

[8] F. H. Fahey, "Data Acquisition in PET Imaging," *Journal of Nuclear Medicine Technology,* vol. 30, pp. 39-49, 2002.

[9] S. E. Derenzo, W. W. Moses, R. H. Huesman, and T. F. Budinger, "Critical instrumentation issues for resolution smaller than 2mm, high sensitivity brain PET," in *Brain PET*, Akita, Japan, 1993, pp. 25-47.

[10] S. R. Cherry, J. A. Sorenson, and M. E. Phelps, *Physics in Nuclear Medicine*, 3 ed. Philadelphia: Saunders, 2003.

[11] S. E. Derenzo, "Mathematical removal of positron range blurring in high resolution tomography," *IEEE Transactions on Nuclear Science,* vol. 33, pp. 565-569, 1986.

[12] B. Bai, R. LaForest, A. Smith, and R. M. Leahy, "Evaluation of MAP image reconstruction with positron range modeling for 3D PET," in *IEEE Nuclear Science Sympoium and Medical Imaging Conference*, Puerto Rico, USA, 2005, pp. 2686-2689.

[13] G. Muehllehner, "Effect of resolution improvement on required count density in ECT imaging: a computer simulation," *Physics in Medicine and Biology,* vol. 30, pp. 163-173, 1985.

[14] R. Lecomte, "Novel detector technology for clinical PET," *European Journal of Nuclear Medicine and Molecular Imaging,* vol. 36, pp. S69-85, 2009.

[15] J. S. Karp, S. Surti, M. E. Daube-Witherspoon, and G. Muehllehner, "Benefit of Time-of-Flight in PET: Experimental and Clinical Results," *Journal of Nuclear Medicine,* vol. 49, pp. 462-470, 2008.

[16] W. W. Moses, "Recent advances and futire advances in time-of-flight PET," *Nuclear Instruments & Methods in Physics Research Section a-Accelerators Spectrometers Detectors and Associated Equipment,* vol. A 580, pp. 919-927, 2007.

[17] B. J. Pichler, M. S. Judenhofer, C. Catana, J. H. Walton, M. D. Kneilling, R. E. Nutt, S. Siegel, C. D. Claussen, and S. R. Cherry, "Performance test of an LSO-APD detector in a 7-T MRI scanner for simultaneous PET/MRI," *Journal of Nuclear Medicine,* vol. 47, pp. 639-647, 2006.

[18] R. Raylman, S. Majewski, S. K. Lemieux, S. S. Velan, B. Kross, V. Popov, M. F. Smith, D. Weisenberger, C. Zorn, and G. D. Marano, "Simultaneous MRI and PET imaging of a rat brain," *Physics in Medicine and Biology,* vol. 51, pp. 6371-6379, 2006.

[19] Y. Shao, S. R. Cherry, K. Farahani, K. Meadors, S. Siegel, R. W. Silverman, and P. Marsden, "Simultaneous PET and MR imaging.," *Physics in Medicine and Biology,* vol. 42, pp. 1965-1970, 1997.

[20] C. Woody, D. Schlyer, P. Vaska, D. Tomasi, S. Solis-Najera, W. Rooney, J. F. Pratte, S. Junnarkar, S. Stoll, Z. Master, M. Purschke, S.-J. Park, S.

Southekal, A. Kriplani, S. Krishnamoorthy, S.-H. Maramraju, P. O'Connor, and V. Radeka, "Preliminary studies of a simultaneous PET/MRI scanner based on the RatCAP small animal tomograph," *Nuclear Instruments & Methods in Physics Research Section a-Accelerators Spectrometers Detectors and Associated Equipment,* pp. 102-105, 2007.

[21] J. B. Birks, *Theory and practice of scintillation counting*. New York: Pergamon, 1964.

[22] "Hamamatsu Photonics, Japan; Available at http://www.hamamatsu.com."

[23] R. J. McIntyre, "Multiplication noise in uniform avalanche diodes," *IEEE Transactions on Electron Devices,* vol. 13, pp. 164-168, 1966.

[24] P. Buzhan, B. Dolgoshein, L. Filatov, A. llyin, V. Kaplin, A. Karakash, S. Klemin, R. Mirzoyan, N. Otte, E. Popov, V. Sosnovtsev, and M. Teshima, "Large area silicon photomultipliers: Performance and applications," in *4th International Conference on New Developments in Photodetection*, Beaune, 2005, pp. 78-82.

[25] D. Henseler, R. Grazioso, N. Zhang, and M. Schmand, "SiPM performance in PET Application: an experimental and theoretical analysis," in *IEEE Nuclear Science Symposium and Medical Imaging Conference*, Orlando, FL, 2009, pp. 1941-1948.

[26] N. Otte, B. Dolgoshein, J. Hose, S. Klemin, E. Lorenz, R. Mirzoyan, E. Popova, and M. Teshima, "The SiPM - A new photon detector for PET," *Nuclear Physics B-Proceedings Supplements,* vol. 150, pp. 417-420, Jan 2006.

[27] R. Freifelder, J. S. Karp, M. J. Geagan, and G. Muehllehner, "Design and performance of the head PENN-PET scanner.," *IEEE Transactions on Nuclear Science,* vol. 41, pp. 436-440, 1994.

[28] S. Surti, J. S. Karp, R. Freifelder, and F. Liu, "Optimizing the performance of a PET detector using discrete GSO crys- tals on a continuous lightguide.," *IEEE Transactions on Nuclear Science,* vol. 47, pp. 1030-1036, 2000.

[29] S. Surti and J. S. Karp, "Imaging characteristics of a 3-dimensional GSO whole-body PET camera," *Journal of Nuclear Medicine,* vol. 45, pp. 1040-1049, Jun 2004.

[30] S. Surti, J. S. Karp, A. E. Perkins, C. A. Cardi, M. E. Daube-Witherspoon, A. Kuhn, and G. Muehllehner, "Imaging performance of A-PET: A small animal PET camera," *IEEE Transactions on Medical Imaging,* vol. 24, pp. 844-852, Jul 2005.

[31] M. Casey and R. Nutt, "A multicrystal two dimensional BGO detector system for positron emission tomography.," *IEEE Transactions on Nuclear Science,* vol. 33, pp. 460-463, 1986.

[32] R. Nutt, "The history of positron emission tomography," *Molecular Imaging and Biology,* vol. 4, pp. 11-26, 2002.

[33] W. H. Wong, J. Uribe, K. Hicks, and M. Zambelli, "A 2-dimensional detector decoding study on BGO arrays with quadrant sharing photomultipliers.," *IEEE Transactions on Nuclear Science,* vol. 41, pp. 1453-1457, 1994.

[34] S. Kim, W. H. Wong, S. P. Xie, R. Ramirez, S. Liu, H. Li, T. Xing, Y. Wang, J. Uribe, H. Baghaei, and J. Zhang, " High resolution GSO block detectors using PMT-quadrant-sharing design for small animal PET," *IEEE Transactions on Nuclear Science,* vol. 53, pp. 40-43, 2006.

[35] S. Liu, J. G. Liu, Y. Zhang, S. Kim, H. Li, R. Ramirez, W. T. Wang, H. Baghaei, and W. H. Wong, "New 9x9 and 10x10 BGO Block Detector for Human PET Using PMT Quadrant Sharing Design," *IEEE Transactions on Nuclear Science,* vol. 55, pp. 457-462, 2008.

[36] R. Lecomte, J. Cadorette, S. Rodrigue, D. Lapointe, D. Rouleau, M. Bentourkia, R. Yao, and P. Msaki, "Initial results from the Sherbrooke avalanche photodiode positron tomograph," *IEEE Transactions on Nuclear Science,* vol. 43, pp. 1952-1957, 1996.

[37] S. I. Ziegler, B. J. Pichler, G. Boening, H. Rafecas, S. Bieler, W. Pimpl, E. Lorenz, and M. Schwaiger, "MadPET: High resolution animal pet with avalanche photodiode arrays and LSO crystals.," *Journal of Nuclear Medicine,* vol. 41, pp. 20P-20P, May 2000.

[38] P. Vaska, C. L. Woody, D. J. Schlyer, S. Shokouhi, S. P. Stoll, J. F. Pratte, P. O'Connor, S. S. Junnarkar, S. Rescia, B. Yu, M. Purschke, A. Kandasamy, A. Villanueva, A. Kriplani, V. Radeka, N. Volkow, R. Lecomte, and R. Fontaine, "RatCAP: Miniaturized head-mounted PET for conscious rodent brain imaging," *IEEE Transactions on Nuclear Science,* vol. 51, pp. 2718-2722, Oct 2004.

[39] J. B. Mosset, O. Devroede, M. Krieguer, M. Rey, J. M. Vieira, J. H. Jung, C. Kuntner, M. Streun, K. Ziemons, E. Auffray, P. Sempere-Roldan, P. Lecoq, P. Bruyndonckx, J. F. Loude, S. Tavernier, and C. Morel, "Development of an optimized LSO/LuYAP phoswich detector head for the Lausanne ClearPET demonstrator," *IEEE Transactions on Nuclear Science,* vol. 53, pp. 25-29, Feb 2006.

[40] C. Woody, P. Vaska, D. Schlyer, J. F. Pratte, S. Junnarkar, S.-J. Park, S. Stoll, M. Purschke, S. Southekal, A. Kriplani, S. Krishnamoorthy, S.-H. Maramraju, D. Lee, W. Schiffer, S. Dewey, J. Neill, A. Kandasamy, P. O'Connor, V. Radeka, R. Fontaine, and R. Lecomte, "Initial studies using the RatCAP conscious animal PET tomograph," *Nuclear Instruments & Methods in Physics Research Section a-Accelerators Spectrometers Detectors and Associated Equipment,* vol. 571, pp. 14-17, 2007.

[41] C. Knoess, S. Siegel, A. Smith, D. F. Newport, N. Richerzhagen, A. Winkeler, A. Jacobs, R. N. Goble, R. Graf, K. Wienhard, and W. D. Heiss, "Performance evaluation of the microPET R4 PET scanner for rodents," *European Journal of Nuclear Medicine and Molecular Imaging,* vol. 30, pp. 737-747, 2003.

[42] Y. C. Tai, A. F. Chatziioannou, Y. F. Yang, R. W. Silverman, K. Meadors, S. Siegel, D. F. Newport, J. R. Stickel, and S. R. Cherry, "MicroPET II: design, development and initial performance of an improved microPET scanner for small-animal imaging," *Physics in Medicine and Biology,* vol. 48, pp. 1519-1537, Jun 7 2003.

[43] Y. C. Tai, A. Ruangma, D. Rowland, S. Siegel, D. F. Newport, P. L. Chow, and R. Laforest, "Performance evaluation of the microPET focus: A third-generation microPET scanner dedicated to animal imaging," *Journal of Nuclear Medicine,* vol. 46, pp. 455-463, Mar 2005.

[44] R. S. Miyaoka, S. G. Kohlmyer, and T. K. Lewellen, "Performance characteristics of micro crystal element (MiCE) detectors," *IEEE Transactions on Nuclear Science,* vol. 48, pp. 1403-1407, Aug 2001.

[45] R. S. Miyaoka, M. L. Janes, K. Lee, B. K. Park, S. B. Gillispie, P. E. Kinahan, and T. K. Lewellen, "Design overview and preliminary results for the micro crystal element scanner (MiCES)." *Journal of Nuclear Medicine,* vol. 44, pp. 160P-160P, May 2003.

[46] J. R. Stickel, K. Vaigneur, and S. R. Cherry, "Fabrication and Experimental Evaluation of a 0.5 mm LSO Array for Use in Small Animal PET Imaging," *IEEE Nuclear Science Symposium, 2005*.

[47] V. V. Nagarkar, S. V. Tipnis, K. Shah, I. Shestakova, and S. R. Cherry, "A high efficiency pixelated detector for small animal PET," *IEEE Transactions on Nuclear Science,* vol. 51, pp. 801-804, Jun 2004.

[48] A. Chatziioannou, R. W. Silverman, K. Meadors, T. H. Farquhar, and S. R. Cherry, "Techniques to Improve the Spatial Sampling of MicroPET - A High Resolution Animal PET Tomograph," *IEEE Transactions on Nuclear Science,* vol. 47, pp. 422-427, 2000.

[49] J. S. Karp, R. Freifelder, M. J. Geagan, G. Muehllehner, P. E. Kinahan, B. Lewitt, and L. Shao, "Three-dimensional imaging characteristics of the HEAD PENN-PET scanner," *IEEE Transactions on Nuclear Science,* vol. 38, pp. 636-643, 1997.

[50] L. E. Adam, J. S. Karp, M. E. Daube-Witherspoon, and R. J. Smith, "Performance of a whole-body PET scanner using curve-plate NaI(Tl) detectors," *Journal of Nuclear Medicine,* vol. 42, pp. 1821-1830, 2001.

[51] S. Siegel, S. R. Cherry, A. R. Ricci, Y. P. Shao, and M. E. Phelps, "Development of Continuous Detectors for a High-Resolution Animal Pet System," *IEEE Transactions on Nuclear Science,* vol. 42, pp. 1069-1074, Aug 1995.

[52] E. N. Gimenez, J. M. Benlloch, M. Gimenez, C. W. Lerche, N. Fernandez, N. Pavon, M. Rafecas, F. Sanchez, A. Sebastia, R. Esteve, J. D. Martinez, and J. Toledo, "Detector optimization of a small animal PET camera based on continuous LSO crystals and flat panel PS-PMTs," *Nuclear Science Symposium Conference Record, 2004 IEEE,* vol. 6, pp. 3885-3889, 2004.

[53] J. Joung, R. S. Miyaoka, and T. K. Lewellen, "cMiCE: a high resolution animal PET using continuous LSO with a statistics based positioning scheme," *Nuclear Instruments & Methods in Physics Research Section a-Accelerators Spectrometers Detectors and Associated Equipment,* vol. 489, pp. 584-598, Aug 21 2002.

[54] S. Tavernier, P. Bruyndonckx, S. Leonard, and O. Devroede, "A high-resolution PET detector based on continuous scintillators," *Nuclear Instruments & Methods in Physics Research Section a-Accelerators Spectrometers Detectors and Associated Equipment,* vol. 537, pp. 321-325, Jan 21 2005.

[55] S. McCallum, P. Clowes, and A. Welch, "A four-layer attenuation compensated PET detector based on APD arrays without discrete crystal elements," *Physics in Medicine and Biology,* vol. 50, pp. 4187-4207, Sep 7 2005.

[56] M. C. Maas, D. J. van der Laan, D. R. Schaart, J. Huizenga, J. C. Brouwer, P. Bruyndonckx, S. Leonard, C. Lemaitre, and C. W. E. van Eijk, "Experimental characterization of monolithic-crystal small animal PET detectors read out by APD arrays," *IEEE Transactions on Nuclear Science,* vol. 53, pp. 1071-1077, Jun 2006.

[57] D. Meier, P. Czermak, P. Jalocha, B. Sowicki, M. Kowal, W. Dulinski, G. Maelhum, E. Nygard, K. Yoshioka, J. Fuster, C. Lacasta, M. Mikuz, S. Roe, P. Weilhammer, C.-H. Hua, S. J. Park, S. J. Wildermann, L. Zhang, N. H. Clinthorne, and W. L. Rogers, "Silicon detector for a compton camera in nuclear medical imaging," *IEEE Transactions on Nuclear Science,* vol. 49, pp. 812-816, 2002.

[58] B. F. Phlips, R. A. Kroeger, J. D. Kurfess, W. N. Johnson, W. N. Wulf, and E. I. Novikova, "Small animal PET imaging with germanium strip detectors," in *IEEE Nuclear Science Symposium and Medical Imaging Conference*, 2002.

[59] S.-J. Park, W. L. Rogers, and N. H. Clinthorne, "Design of a very high-resolution small animal PET scanner using a silicon scatter detector insert," *Physics in Medicine and Biology,* vol. 52, pp. 4653-4677, 2007.

[60] S.-J. Park, W. L. Rogers, S. Huh, H. Kagan, K. Honscheid, D. Burdette, E. Chesi, C. Lacasta, G. Llosa, M. Mikuz, A. Studen, O. Weilhammer, and N.

H. Clinthorne, "Performance evaluation of a very high resolution small animal PET imager using silicon scatter detectors," *Physics in Medicine and Biology,* vol. 52, pp. 2807-2826, 2007.

[61] H. C. Boston, A. J. Boston, R. J. Cooper, J. Cresswell, A. N. Grint, A. R. Mather, P. J. Nolan, D. P. Scraggs, G. Turk, C. J. Hall, I. Lazarus, A. Berry, T. Beveridge , J. Gillam, and R. Lewis, "Characterisation of the SmartPET planar Germanium detectors," in *Proceedings of the 11th Symposium on Radiation Measurements and Applications* 2007.

[62] P. Vaska, A. Bolotnikov, G. Carini, G. Camarda, J. F. Pratte, A. Dilmanian, S. J. Park, and R. B. James, "Studiess of CZT for PET applications," *IEEE Nuclear Science Symposium and Medical Imaging Conference,* vol. 1-5, pp. 2799-2802, 2005.

[63] A. Drezet, O. Monnet, F. Mathy, G. Montemont, and L. Verger, "CdZnTe detectors for small field of view positron emission tomographic imaging," *Nuclear Instruments & Methods in Physics Research Section a-Accelerators Spectrometers Detectors and Associated Equipment,* vol. 571, pp. 465-470, 2007.

[64] K. Ishii, Y. Kikuchi, S. Matsuyama, Y. Kanai, K. Kotani, T. Ito, H. Yamakazi, D. Amano, M. Yamada, and T. Yamaguchi, "First achievement of less than 1 mm FWHM resolution in practical semiconductor animal PET scanner," *Nuclear Instruments & Methods in Physics Research Section a-Accelerators Spectrometers Detectors and Associated Equipment,* vol. 576, pp. 435-440, 2007.

[65] G. Mitchell, S. Sinha, J. R. Stickel, S. Bowen, L. Cirignano, P. A. Dokhale, S. Kim, K. Shah, and S. R. Cherry, "CdTe strip detector characterization for high resolution small animal PET," *IEEE Transactions on Nuclear Science,* vol. 55, pp. 870-876, 2008.

[66] P. Vaska, D.-H. Kim, S. Krishnamoorthy, S. Southekal, S. Stoll, J. Fried, D. Schulz, J. F. Pratte, A. Dragone, Y.-G. Cui, G. DeGeronimo, A. Bolotnikov, C. Woody, and P. O'Connor, "Performance of a Prototype Ultra-High Resolution PET Scanner Using CZT Pixel Detectors," in *IEEE Nuclear Scienc Symposium and Medical Imaging Conference* Orlando, FL, 2009.

[67] P. Vaska, D.-H. Kim, S. Southekal, J. F. Pratte, J. Fried, S. Krishnamoorthy, S. Stoll, and A. Bolotnikov, "Ultra-high resolution PET: A CZT-based

scanner for the mouse brain," *Journal of Nuclear Medicine,* vol. 50, p. 293P, 2009.

[68] H. Peng and C. S. Levin, "Design study of a high-resolution breast-dedicated PET system built from cadmium zinc telluride detectors," *Physics in Medicine and Biology,* vol. 55, pp. 2761-2788, 2010.

[69] A. P. Jeavons, R. A. Chandler, and C. A. R. Dettmar, "A 3D HIDAC-PET camera with sub-millimetre resolution for imaging small animals," *IEEE Transactions on Nuclear Science,* vol. 46, pp. 468-473, Jun 1999.

[70] J. Missimer, Z. Madi, M. Honer, C. Keller, A. Schubiger, and S.-M. Ametamey, "Performance evaluation of the 16-module quad-HIDAC small animal PET camera," *Physics in Medicine and Biology,* vol. 49, pp. 2069-2081, 2004.

[71] J. L. Lacy, C. S. Martin, and L. P. Armendarez, "High sensitivity, low cost PET using lead-walled straw detectors," *Nuclear Instruments & Methods in Physics Research Section a-Accelerators Spectrometers Detectors and Associated Equipment,* vol. 471, pp. 88-93, Sep 21 2001.

[72] N. N. Shehad, A. Athanasaides, C. S. Martin, L. Sun, and J. L. Lacy, "Novel lead-walled straw PET detector for specialized imaging applications," *IEEE Nuclear Science Symposium Conference Record, 2005,* vol. 5, pp. 2895-2898, 2005.

[73] A. Blanco, V. Chepel, R. F. Marques, P. Fonte, M. I. Lopes, V. Peskov, and A. Policarpo, "Perspectives for positron emission tomography with RPCs," in *Proceedings of the Sixth International Workshop on Resistive Plate Chambers and Related Detectors* 2003, pp. 88-93.

[74] A. Blanco, N. Carolino, C. M. B. A. Correia, L. Fazendeiro, N. C. Ferreira, M. F. F. Marques, R. F. Marques, P. Fonte, and M. P. Macedo, "RPC-PET: a new very high resolution PET technology," *IEEE Transactions on Nuclear Science,* vol. 53, pp. 2489-2494, 2006.

[75] V. Chepel, V. Solovov, J. van Der Marel, M. I. Lopes, P. Crespo, L. Janeiro, D. Santos, R. F. Marques, and A. J. P. L. Policarpo, "The liquid xenon detector for PET: recent results," *IEEE Transactions on Nuclear Science,* vol. 46, pp. 1038-1044, 1999.

[76] P. Amaudruz, D. Bryman, L. Kurchaninov, P. Lu, C. Marshall, J. P. Martin, A. Muennich, F. Retiere, A. Sher, and V. Sossi, "Simultaneous reconstruction of scin- tillation light and ionization charge produced by 511 keV photons in liquid xenon: Potential application to PET," *Nuclear Instruments & Methods in Physics Research Section a-Accelerators Spectrometers Detectors and Associated Equipment,* vol. 607, pp. 668-676, 2009.

[77] F. Retiere, "A liquid Xenon detector for micro-PET," in *1st International Conference on Technology and Instrumentation in Particle Physics* 2010, pp. 591-593.

[78] F. Lamare, A. Turzo, Y. Bizais, C. C. Le Rest, and D. Visvikis, "Validation of a Monte Carlo simulation of the Philips Allegro/GEMINI PET systems using GATE," *Physics in Medicine and Biology,* vol. 51, pp. 943-962, Feb 21 2006.

[79] R. Lecomte, "Technology challenges in small animal PET imaging," *Nuclear Instruments & Methods in Physics Research Section a-Accelerators Spectrometers Detectors and Associated Equipment,* vol. A 527, pp. 157-165, 2004.

[80] S. Southekal, "Strategies for Quantitative Neuroimaging with the Rat Conscious Animal PET (RatCAP)," in *Biomedical Engineering*: Stony Brook University, 2009.

[81] J. R. Stickel, Q. Jinyi, and S. R. Cherry, "Fabrication and Characterization of a 0.5-mm Lutetium Oxyorthosilicate Detector Array for High-Resolution PET Applications," *Journal of Nuclear Medicine,* vol. 48, pp. 115-121, 2007.

[82] S. St James, M. Koschan, C. L. Melcher, and S. R. Cherry, "Characterizing the Performance of a 220 Micron Depth-of-Interaction LSO PET Detector," in *IEEE Nuclear Science Symposium and Medical Imaging Conference* Knoxville, 2010.

[83] J. Seidel, J. J. Vaquero, S. Siegel, W. R. Gandler, and M. V. Green, "Depth identification accuracy of a three layer phoswich PET detector module," *IEEE Transactions on Nuclear Science,* vol. 46, 1999.

[84] N. Inadama, H. Murayama, T. Omura, T. Yamashita, S. Yamamoto, H. Ishibashi, H. Kawai, K. Omi, T. Umehara, and T. Kasahara, "A depth of

interaction detector for PET with GSO crystals doped with different amounts of Ce," *Ieee Transactions on Nuclear Science,* vol. 49, pp. 629-633, Jun 2002.

[85] N. Indama, H. Murayama, M. Hamamoto, T. Tsuda, Y. Ono, T. Yamaya, E. Yoshida, K. Shibuya, and F. Nishikodo, "8-Layer DOI Encoding of 3-Dimensional Crystal Array," *IEEE Transactions on Nuclear Science,* vol. 53, 2006.

[86] W. W. Moses and S. E. Derenzo, "Design studies for a PET detector module using a pin photodiode to measure depth of interaction," *IEEE Transactions on Nuclear Science,* vol. 41, pp. 1441-1445, 1994.

[87] P. A. Dokhale, R. W. Silverman, K. Shah, R. Grazioso, R. Farrell, J. Glodo, M. McClish, G. Entine, V.-H. Tran, and S. R. Cherry, "Performance measurements of a depth-encoding PET detector module based on position-sensitive avalanche photodiode read-out," *Physics in Medicine and Biology,* vol. 49, pp. 4293-4304, 2004.

[88] M. B. Williams, R. M. Sealock, S. Majewski, and D. Weisenberger, "PET detector using waveshifting optical fibers and microchannel plate PMT with delay line readout," *IEEE Transactions on Nuclear Science,* vol. 45, pp. 195-205, 1998.

[89] T. Tsuda, H. Murayama, K. Kitamura, N. Inadama, T. Yamaya, E. Yoshida, F. Nishikido, M. Hamamoto, H. Kawai, and Y. Ono, "Performance evaluation of a subset of a four-layer LSO detector for a small animal DOI PET scanner: jPET-RD," *IEEE Transactions on Nuclear Science,* vol. 53, pp. 35-39, Feb 2006.

[90] Y. Yang, P. A. Dokhale, R. W. Silverman, K. Shah, M. McClish, R. Farrell, G. Entine, and S. R. Cherry, "Depth of interaction resolution measurements for a high resolution PET detector using position sensitive avalanche photodiodes," *Physics in Medicine and Biology,* vol. 51, pp. 2131-2142, 2006.

[91] Y. Wang, J. Seidel, B. M. W. Tsui, J. J. Vaquero, and M. G. Pomper, "Performance evaluation of the GE healthcare eXplore VISTA dual-ring small-animal PET scanner," *Journal of Nuclear Medicine,* vol. 47, pp. 1891-1900, 2006.

[92] H. W. A. M. Jong, F. H. P. van Velden, R. W. Kloet, F. L. Buijs, R. Boellaard, and A. Lammertsma, "Performance evaluation of the ECAT HRRT: an LSO-LYSO double layer high resolution, high sensitivity scanner," *Physics in Medicine and Biology,* vol. 52, pp. 1505-1526, 2007.

[93] H. O. Anger, "Scintillation Camera," *Review of Scientific Instruments,* vol. 29, pp. 27-33, 1958.

[94] "Saint Gobain Crystals - NaI(Tl); Available at http://www.detectors.saint-gobain.com/uploadedFiles/SGdetectors/Documents/Product Data Sheets/NaI(Tl)-Data-Sheet.pdf," 2008.

[95] S. Surti, J. S. Karp, and G. Muehllehner, "Evaluation of Pixelated Nai(Tl) detectors for PET," *IEEE Transactions on Nuclear Science,* vol. 50, pp. 24-31, 2003.

[96] C. L. Melcher and J. S. Schweitzer, "A Promising New Scintillator - Cerium-Doped Lutetium Oxyorthosilicate," *Nuclear Instruments & Methods in Physics Research Section a-Accelerators Spectrometers Detectors and Associated Equipment,* vol. 314, pp. 212-214, Apr 1 1992.

[97] P. Vaska and D. L. Alexoff, "Effects of natural LSO radioactivity on microPET quantitation.," *Journal of Nuclear Medicine,* vol. 44, pp. 138P-138P, May 2003.

[98] E. V. D. Van Loef, P. Dorenbos, C. W. E. van Eijk, K. Kramer, and H. U. Gudel, "High-energy-resolution scintillator: Ce3+ activated LaBr3," *Applied Physics Letters,* vol. 79, pp. 1573-1575, Sep 3 2001.

[99] E. V. D. Van Loef, P. Dorenbos, C. W. E. van Eijk, K. W. Kramer, and H. U. Gudel, "Scintillation properties of LaBr3 : Ce3+ crystals: fast, efficient and high-energy-resolution scintillators," *Nuclear Instruments & Methods in Physics Research Section a-Accelerators Spectrometers Detectors and Associated Equipment,* vol. 486, pp. 254-258, Jun 21 2002.

[100] K. S. Shah, J. Glodo, M. Klugerman, W. W. Moses, S. E. Derenzo, and A. J. Weber, "LaBr3 : Ce scintillators for gamma-ray spectroscopy," *IEEE Transactions on Nuclear Science,* vol. 50, pp. 2410-2413, Dec 2003.

[101] "Advanced Photonics, Inc.; Available at http://www.advancedphotonix.com/."

[102] "Radiation Monitoring Devices Inc; Available at http://www.rmdinc.com."

[103] W. W. Moses, S. E. Derenzo, C. Melcher, and R. Manante, "A room temperature LSO/PIN photodiode PET detector module that measures depth-of-interaction," *IEEE Transactions on Nuclear Science,* vol. 42, pp. 1085-1089, 1995.

[104] T. Frach, W. Ruetten, K. Fiedler, G. Maehlum, T. Solf, and A. Thon, "Assessment of photodiodes as a light detector for PET scanners," in *IEEE Nuclear Science Symposium*, Rome, Italy, 2004, pp. 4177-4181.

[105] B. J. Pichler, B. K. Swann, J. Rochelle, R. E. Nutt, S. R. Cherry, and S. B. Siegel, "Lutetium oxyorthosilicate block detector readout by avalanche photodiode arrays for high resolution animal PET," *Physics in Medicine and Biology,* vol. 49, pp. 4305-4319, Sep 21 2004.

[106] R. Grazioso, M. Aykac, M. Casey, G. Givens, and M. Schmand, "APD performance in light sharing PET Applications," *IEEE Transactions on Nuclear Science,* vol. 52, pp. 1413-1416, 2005.

[107] R. Lecomte, R. Dekemp, R. Klein, J. Cadorette, M. Bergeron, M. Lepage, V. Selivanov, M. A. Tetrault, V. Viscogliosi, and R. Fontaine, "LabPET: A high-performance APD-based digital PET scanner for small animal imaging," *Journal of Nuclear Medicine,* vol. 47 (Supplement), p. 194P, 2006.

[108] R. Farrell, K. Vanderpuye, L. Cirignano, M. Squillante, and G. Entine, "Radiation detection performance of a very high gain avalanche photodiode," *Nuclear Instruments & Methods in Physics Research Section a-Accelerators Spectrometers Detectors and Associated Equipment,* vol. 353, pp. 176-179, 1994.

[109] R. Farrell, K. Shah, K. Vanderpuye, R. Grazioso, R. Myers, and G. Entine, "APD arrays and large-area APDs via a new planar process," *Nuclear Instruments & Methods in Physics Research Section a-Accelerators Spectrometers Detectors and Associated Equipment,* vol. A442, pp. 171-178, 2000.

[110] P. Andreo, "Monte-Carlo techniques in medical radiation physics," *Physics in Medicine and Biology,* vol. 36, pp. 861-920, 1991.

[111] H. Zaidi, "Relevance of accurate Monte Carlo modeling in nuclear medical imaging," *Medical Physics,* vol. 24, pp. 574-608, 1999.

[112] H. Zaidi and G. Sqouros, *Therapeutic Applications Of Monte Carlo Calculations In Nuclear Medicine*, 1 ed.: Taylor & Francis, 2002.

[113] A. Levin and C. Moisan, "A more physical approach to model the surface treatment of scintillation counters and its implementation into DETECT," in *IEEE Nuclear Science Symposium*, Anaheim, CA, 1996, pp. 702-706.

[114] I. Buvat and I. Castigloni, "Monte Carlo simulatios in SPECT and PET," *Quarterly Journal of Nuclear Medicine,* vol. 46, pp. 48-61, 2002.

[115] T. K. Lewellen, R. Harrison, and S. Vannoy, "The SimSET Program, in Monte Carlo Calculations," in *Monte Carlo Calculations in Nuclear medicine*, M. Ljungberg, S. Strand, and M. King, Eds. Philadelphia: Institute of Physics Publishing, 1998, pp. 77-97.

[116] "GEANT4; Available at http://geant4.web.cern.ch/geant4/."

[117] S. Agostinelli, J. Allison, K. Amako, J. Apostolakis, H. Araujo, P. Arce, M. Asai, D. Axen, S. Banerjee, G. Barrand, F. Behner, L. Bellagamba, J. Boudreau, L. Broglia, A. Brunengo, H. Burkhardt, S. Chauvie, J. Chuma, R. Chytracek, G. Cooperman, G. Cosmo, P. Degtyarenko, A. Dell'Acqua, G. Depaola, D. Dietrich, R. Enami, A. Feliciello, C. Ferguson, H. Fesefeldt, G. Folger, F. Foppiano, A. Forti, S. Garelli, S. Giani, R. Giannitrapani, D. Gibin, J. J. G. Cadenas, I. Gonzalez, G. G. Abril, G. Greeniaus, W. Greiner, V. Grichine, A. Grossheim, S. Guatelli, P. Gumplinger, R. Hamatsu, K. Hashimoto, H. Hasui, A. Heikkinen, A. Howard, V. Ivanchenko, A. Johnson, F. W. Jones, J. Kallenbach, N. Kanaya, M. Kawabata, Y. Kawabata, M. Kawaguti, S. Kelner, P. Kent, A. Kimura, T. Kodama, R. Kokoulin, M. Kossov, H. Kurashige, E. Lamanna, T. Lampen, V. Lara, V. Lefebure, F. Lei, M. Liendl, W. Lockman, F. Longo, S. Magni, M. Maire, E. Medernach, K. Minamimoto, P. M. de Freitas, Y. Morita, K. Murakami, M. Nagamatu, R. Nartallo, P. Nieminen, T. Nishimura, K. Ohtsubo, M. Okamura, S. O'Neale, Y. Oohata, K. Paech, J. Perl, A. Pfeiffer, M. G. Pia, F. Ranjard, A. Rybin, S. Sadilov, E. Di Salvo, G. Santin, T. Sasaki, N. Savvas, Y. Sawada, S. Scherer, S. Seil, V. Sirotenko, D. Smith, N. Starkov, H. Stoecker, J. Sulkimo, M. Takahata, S. Tanaka, E. Tcherniaev, E. S. Tehrani, M. Tropeano, P. Truscott, H. Uno, L. Urban, P. Urban, M. Verderi, A.

Walkden, W. Wander, H. Weber, J. P. Wellisch, T. Wenaus, D. C. Williams, D. Wright, T. Yamada, H. Yoshida and D. Zschiesche, "GEANT4-a simulation toolkit," *Nuclear Instruments & Methods in Physics Research Section a-Accelerators Spectrometers Detectors and Associated Equipment,* vol. 506, pp. 250-303, Jul 1 2003.

[118] "DETECT2000; Available at http://www.gel.ulaval.ca/detect."

[119] G. F. Knoll, T. F. Knoll, and T. M. Henderson, "Light Collection in Scintillation Detector Composites for Neutron Detection," *IEEE Transactions on Nuclear Science,* vol. 35, pp. 872-875, Feb 1988.

[120] G. W. McKinney and S. L. James, "MCNPX 2.7.X - New Features Being Developed," in *IEEE Nuclear Science Symposium and Medical Imaging Conference*, Orlando, FL, 2009.

[121] "GATE - Geant4 Application for Tomographic Emission; Available at http://opengatecollaboration.healthgrid.org/."

[122] S. Jan, G. Santin, D. Strul, S. Staelens, K. Assie, D. Autret, S. Avner, R. Barbier, M. Bardies, P. M. Bloomfield, D. Brasse, V. Breton, P. Bruyndonckx, I. Buvat, A. F. Chatziioannou, Y. Choi, Y. H. Chung, C. Comtat, D. Donnarieix, L. Ferrer, S. J. Glick, C. J. Groiselle, D. Guez, P. F. Honore, S. Kerhoas-Cavata, A. S. Kirov, V. Kohli, M. Koole, M. Krieguer, D. J. van der Laan, F. Lamare, G. Largeron, C. Lartizien, D. Lazaro, M. C. Maas, L. Maigne, F. Mayet, F. Melot, C. Merheb, E. Pennacchio, J. Perez, U. Pietrzyk, F. R. Rannou, M. Rey, D. R. Schaart, C. R. Schmidtlein, L. Simon, T. Y. Song, J. M. Vieira, D. Visvikis, R. V. de Walle, E. Wieers, and C. Morel, "GATE: a simulation toolkit for PET and SPECT," *Physics in Medicine and Biology,* vol. 49, pp. 4543-4561, Oct 7 2004.

[123] "OptiCAD; Available at http://www.opticad.com/."

[124] A. Kriplani, S. P. Stoll, D. J. Schlyer, S. Shokouhi, P. Vaska, A. J. Villanueva, and C. L. Woody, "Light output measurements of LSO single crystals and 4×8 arrays: comparison of experiment with Monte Carlo simulations," in *IEEE Nuclear Science Symposium and Medical Imaging Conference*, Portland, OR, 2003, pp. 3036-3040.

[125] "ZEMAX; Avaialable at http://www.zemax.com/."

[126] E. Lorincz, G. Erdei, I. Peczeli, C. Steinbach, F. Ujhelyi, and T. Bukki, "Modeling and Optimization of Scintillator Arrays for PET Detectors," *IEEE Transactions on Nuclear Science,* vol. 57, pp. 48-54, 2010.

[127] G. Tsang, C. Moisan, and J. G. ROgers, "A simulation to model position encoding multicrystal PET detectors," *IEEE Transactions on Nuclear Science,* vol. 42, pp. 2236-2243, 1995.

[128] G. Hull, S. Du, T. Niedermayr, S. Payne, N. Cherepy, A. Drobshoff, and L. Fabris, "Light collection optimization in scintillator-based gamma-ray spectrometers," *Nuclear Instruments & Methods in Physics Research Section a-Accelerators Spectrometers Detectors and Associated Equipment,* vol. 588, pp. 384-388, 2008.

[129] C. O. Steinbach, A. Szlavecz, B. Benyo, T. Bukki, and E. Lorincz, "Validation of Detect2000-Based PetDetSim by Simulated and Measured Light Output of Scintillator Crystal Pins for PET Detectors," *IEEE Transactions on Nuclear Science,* vol. 57, pp. 2460-2467, 2010.

[130] E. Hoskinson, A. Levine, and C. Moisan, "BUILDER, a high level language interface to DETECT for the design of scintillation detectors," 3.0 ed, 1996, pp. TRI-DN-96-28.

[131] C. L. Melcher and J. S. Schweitzer, "Cerium-Doped Lutetium Oxyorthosilicate - a Fast, Efficient New Scintillator," *IEEE Transactions on Nuclear Science,* vol. 39, pp. 502-505, Aug 1992.

[132] M. Moszynski, M. Kapusta, D. Wolski, M. Szawlowski, and W. Klamra, "Energy resolution of scintillation detectors readout with large area avalanche photodiodes and photomultipliers," *IEEE Transactions on Nuclear Science,* vol. 45, pp. 472-477, Jun 1998.

[133] H. Rothfuss, M. Casey, M. Conti, N. Doshi, L. Eriksson, and M. Schmand, "Monte Carlo simulation study of LSO crystals," *IEEE Transactions on Nuclear Science,* vol. 51, pp. 770-774, Jun 2004.

[134] M. Moszynski, M. Kapusta, J. Zalipska, M. Balcerzyk, D. Wolski, M. Szawlowski, and W. Klamra, "Low energy gamma-rays scintillation detection with large area avalanche photodiodes," *IEEE Transactions on Nuclear Science,* vol. 46, pp. 880-885, Aug 1999.

[135] M. L. Purschke, A. Kandasamy, P. Connor, J.-F. Pratte, D. J. Schlyer, S. P. Stoll, P. Vaska, A. Villanueva, C. L. Woody, S. S. Junnarkar, S. Krishnamoorthy, and S. Shokouhi, "PDAQ - A fast data acquisition system for the RatCAP Tomograph," *Nuclear Science Symposium Conference Record, 2004 IEEE,* vol. 3, pp. 1486-1488, 2004.

[136] "ROOT; Available at http://root.cern.ch/drupal/."

[137] R. Brun and F. Rademakers, "ROOT - An object oriented data analysis framework," *Nuclear Instruments & Methods in Physics Research Section a-Accelerators Spectrometers Detectors and Associated Equipment,* vol. 389, pp. 81-86, Apr 11 1997.

[138] V. Radeka, "Low-Noise Techniques in Detectors," *Annual Review of Nuclear and Particle Science,* vol. 38, pp. 217-277, 1988.

[139] E. Gatti, P. F. Manfredi, M. Sampietro, and V. Speziali, "Suboptimal filtering of l/f-noise in detector charge measurements," *Nuclear Instruments & Methods in Physics Research Section a-Accelerators Spectrometers Detectors and Associated Equipment,* vol. A297, pp. 467-478, 1990.

[140] J. F. Pratte, G. De Geronimo, S. Junnarkar, P. O'Connor, B. Yu, S. Robert, V. Radeka, C. Woody, S. Stoll, P. Vaska, A. Kandasamy, R. Lecomte, and R. Fontaine, "Front-end electronics for the RatCAP mobile animal PET scanner," *IEEE Transactions on Nuclear Science,* vol. 51, pp. 1318-1323, Aug 2004.

[141] H. W. Ott, *Electromagnetic Compatibility Engineering*. Hoboken, Nj: John Wiley & Sons, Inc., Publication, 2009.

[142] P. P. Webb, R. J. McIntyre, and J. Conradi, "Properties of Avalanche Photodiodes," *R.C.A. Review,* vol. 35, pp. 234-278, 1974.

[143] "Band Gap - Semiconductors."

[144] S. Kishimoto, H. Adachi, and M. Ito, "A cooled avalanche photodiode detector for X-ray magnetic diffraction experiments," *Nuclear Instruments & Methods in Physics Research Section a-Accelerators Spectrometers Detectors and Associated Equipment,* vol. 467-468, pp. 1171-1174, 2001.

[145] S. S. James, Y. Yang, Y. B. Wu, R. Farrell, P. A. Dokhale, K. Shah, and S. R. Cherry, "Experimental characterization and system simulations of depth of interaction PET detectors using 0.5 mm and 0.7 mm LSO arrays," *Physics in Medicine and Biology,* vol. 54, pp. 4605-4619, 2009.

[146] P. Berard, M. Bergeron, C. M. Pepin, J. Cadorette, M. A. Tetrault, V. Viscogliosi, R. Fontaine, H. Dautet, M. Davies, P. Deschamps, and R. Lecomte, "Development of a 64-channel APD detector module with individual pixel readout for submillimetre spatial resolution in PET," *Nuclear Instruments & Methods in Physics Research Section a-Accelerators Spectrometers Detectors and Associated Equipment,* vol. 610, pp. 20-23, 2009.

[147] C. M. Pepin, M. Begeron, J. Cadorette, J.-F. Beaudoin, X. Jacques-Bedard, M. Couture, H. Dautet, and R. Lecomte, "New UV-Enhanced, Ultra-Low Noise Silicon Avalanche Photodiode for Radiation Detection and Medical Imaging," in *IEEE Nuclear Science Symposium and Medical Imaging Conference*, Knoxville, TN, 2010.

[148] "Hamamatsu - MPPC; Available at http://sales.hamamatsu.com/en/products/solid-state-division/si-photodiode-series/mppc/part-s10362-11-025c.php."

[149] J. Allison, K. Amako, J. Apostolakis, H. Araujo, P. A. Dubois, M. Asai, G. Barrand, R. Capra, S. Chauvie, R. Chytracek, G. A. P. Cirrone, G. Cooperman, G. Cosmo, G. Cuttone, G. G. Daquino, M. Donszelmann, M. Dressel, G. Folger, F. Foppiano, J. Generowicz, V. Grichine, S. Guatelli, P. Gumplinger, A. Heikkinen, I. Hrivnacova, A. Howard, S. Incerti, V. Ivanchenko, T. Johnson, F. Jones, T. Koi, R. Kokoulin, M. Kossov, H. Kurashige, V. Lara, S. Larsson, F. Lei, O. Link, F. Longo, M. Maire, A. Mantero, B. Mascialino, I. McLaren, P. M. Lorenzo, K. Minamimoto, K. Murakami, P. Nieminen, L. Pandola, S. Parlati, L. Peralta, J. Perl, A. Pfeiffer, M. G. Pia, A. Ribon, P. Rodrigues, G. Russo, S. Sadilov, G. Santin, T. Sasaki, D. Smith, N. Starkov, S. Tanaka, E. Tcherniaev, B. Tome, A. Trindade, P. Truscott, L. Urban, M. Verderi, A. Walkden, J. P. Wellisch, D. C. Williams, D. Wright, and H. Yoshida, "Geant4 developments and applications," *IEEE Transactions on Nuclear Science,* vol. 53, pp. 270-278, 2006.

[150] S. Jan, C. Comtat, R. Trebossen, and A. Syrota, "Monte Carlo simulation of the MicroPET Focus for small animal.," in *J. Nucl. Med.*, 2004, p. 420P.

[151] S. Jan, C. Comtat, D. Strul, G. Santin, and R. Trebossen, "Monte Carlo simulation for the ECAT EXACT HR plus system using GATE," *IEEE Transactions on Nuclear Science,* vol. 52, pp. 627-633, Jun 2005.

[152] M. Kapusta, M. Moszynski, M. Balcerzyk, J. Braziewicz, D. Wolski, J. Pawelke, and W. Klamra, "Comparison of the scintillation properties of LSO:Ce manufactured by different laboratories and of LGSO:Ce," *IEEE Transactions on Nuclear Science,* vol. 47, pp. 1341-1345, 2000.

[153] K. e. a. Nakamura, "The Review of Particle Physics," *Journal of Physics G: Nuclear and Particle Physics,* vol. 37, p. 075201, 2010.

[154] J. Křepelka, "Maximally flat antireflection coatings/Jemná Mechanika A Optika (Published by Academy of Sciences of the Czech Republic)," *Jemná Mechanika A Optika,* vol. 3-5, pp. 53-56, 1992.

[155] P. Vaska, P. Vanier, S. Junnarkar, S. Krishnamoorthy, J. F. Pratte, and S. Stoll, "A compact scintillator-based coded aperture imager for localizing illicit nuclear materials," in *IEEE Nuclear Science Symposium*, Honolulu, Hawaii, 2007, pp. 1195-1197.

[156] "Hamamatsu APD - S8664-55; Available at http://sales.hamamatsu.com/en/products/solid-state-division/si-photodiode-series/si-apd/part-s8664-55.php."

[157] V. Sum, A. R. Berdoz, C. A. Davis, S. A. Page, W. D. Ramsay, W. T. H. Oers, R. A. Schumacher, V. J. Zeps, D. R. Gill, T. Iijima, K. Okada, and F. Takeutchi, "A Time-of-flight array for 1 to 2 GeV/c particles," *Nuclear Instruments & Methods in Physics Research Section a-Accelerators Spectrometers Detectors and Associated Equipment,* vol. A326, pp. 489-495, 1993.

[158] "eV Products; Available at http://www.evmicroelectronics.com/index.html."

[159] P. Bruyndonckx, S. Leonard, S. Tavernier, C. Lemaitre, O. Devroede, Y. B. Wu, and M. Krieguer, "Neural network-based position estimators for PET detectors using monolithic LSO blocks," *IEEE Transactions on Nuclear Science,* vol. 51, pp. 2520-2525, Oct 2004.

[160] P. Bruyndonckx, C. Lemaitre, D. R. Schaart, M. C. Maas, D. J. van der Laan, M. Krieguer, O. Devroede, and S. Tavernier, "Towards a

continuous crystal APD-based PET detector design," *Nuclear Instruments & Methods in Physics Research Section a-Accelerators Spectrometers Detectors and Associated Equipment,* vol. A 571, pp. 182-186, 2007.

[161] D. R. Schaart, H. T. Van Dam, S. Seifert, R. Vinke, P. Dendooven, H. Lohner, and F. J. Beekman, "A novel, SiPM-array-based, monolithic scintillator detector for PET," *Physics in Medicine and Biology,* vol. 54, pp. 3501-3512, 2009.

[162] P. Vaska, S. Krishnamoorthy, S. P. Stoll, C. L. Woody, P. Connor, M. L. Purschke, S. Boose, D. J. Schlyer, and A. Villanueva, "An improved Anger detector approach for PET with high resolution and sensitivity," *IEEE Nuclear Science Symposium Conference Record, 2004,* vol. 6, pp. 3463 - 3466, 16-22 Oct. 2004 2004.

[163] S. Krishnamoorthy, P. Vaska, S. P. Stoll, M. L. Purschke, J.-F. Pratte, C. L. Woody, D. J. Schlyer, and P. Connor, " A prototype Anger-type detector for PET using LSO and large-area APDs," *IEEE Nuclear Science Symposium Conference Record, 2005,* vol. 5, pp. 2845-248, 23-29 Oct. 2005 2005.

[164] S. Krishnamoorthy, S. Stoll, M. Purschke, J. F. Pratte, C. Woody, B. Yu, P. O'Connor, D. Schlyer, and P. Vaska, "Design and Performance of a Light-Sharing Detector for 3D Gamma-Ray Imaging," in *IEEE Nuclear Science Symposium and Medical Imaging Conference* Dresden, Germany, 2008.

[165] S. Krishnamoorthy, S. Stoll, M. Purschke, C. L. Woody, D. Schlyer, and P. Vaska, " A Fully 3-D Maximum Likelihood Event Positioning Scheme with a Measured System Response in Continuous Scintillator Gamma-Ray Detectors," in *IEEE Nuclear Science and Medical Imaging Conference* Knoxville, TN, 2010.

[166] J. H. Joung, R. S. Miyaoka, S. Kohlmyer, and T. K. Lewellen, "Implementation of ML based positioning algorithms for scintillation cameras," *IEEE Transactions on Nuclear Science,* vol. 47, pp. 1104-1111, Jun 2000.

[167] J. Joung, R. S. Miyaoka, S. G. Kohlmyer, and T. K. Lewellen, "Investigation of bias-free positioning estimators for the scintillation

cameras," *IEEE Transactions on Nuclear Science,* vol. 48, pp. 715-719, Jun 2001.

[168] T. Ling, T. H. Burnett, T. K. Lewellen, and R. S. Miyaoka, "Parametric positioning of a continuous crystal PET detector with depth of interaction decoding," *Physics in Medicine and Biology,* vol. 7, pp. 1843-1863, 2008.

[169] R. S. Miyaoka, X. Li, C. Lockhart, and T. K. Lewellen, "Comparison of Detector Intrinsic Spatial resolution characteristics for sensor on the entrance surface and conventional readout designs," *IEEE Transactions on Nuclear Science,* vol. 57, pp. 990-997, 2010.

[170] M. Kaul, S. Surti, R. Wiener, and J. S. Karp, "Thick continuous crystal design for PET," in *IEEE Nuclear Science Symposium*, Dresden, Germany, 2008, pp. 4574-4579.

[171] J. M. Benlloch, V. Carrilero, A. J. Gonzalez, J. Catret, C. W. Lerche, D. Abellan, F. Garcia de Quiros, M. Gimenez, J. Modla, F. Sanchez, N. Pavon, A. Ros, J. D. Martinez, and A. Sebastia, "Scanner calibration of a small animal PET camera based on continuous LSO crystals and flat panel PSPMTs," *Nuclear Instruments & Methods in Physics Research Section a-Accelerators Spectrometers Detectors and Associated Equipment,* vol. A571, pp. 26-29, 2007.

[172] C. W. Lerche, A. Ros, J. M. Monzo, R. J. Aliaga, N. Ferrando, J. D. Martinez, V. Herrero, R. Esteve, R. Gadea, R. J. Colom, J. Toledo, F. Mateo, A. Sebastia, F. Sanchez, and J. M. Benlloch, "Maximum likelihood positioning for gamma-ray imaging detectors with depth of interaction measurement," in *Proceedings of the 8th International Conference on Position Sensitive Detectors*. vol. 604 Glasgow, Scotland, 2009, pp. 359-362.

[173] G. Llosa, J. Barrio, C. Lacasta, M. G. Bisogni, A. D. Guerra, S. Marcatili, B. Barrillon, S. Bondil-Blin, C. D. Taille, and C. Piemonte, "Characterization of a PET detector head based on continuous LYSO crystals and monolithic, 64-pixel silicon photomultiplier matrices," *Physics in Medicine and Biology,* vol. 55, pp. 7299-7315, 2010.

[174] S. R. Eliason, *Maximum Likelihood Estimation: Logic and Practice*, 1 ed.: Sage Publications, Inc.,, 1993.

[175] S. Haykin, *Neural networks: A comprehensive foundation*, 2 ed.: Prentice Hall, 1998.

[176] J. V. Tu, "Advantage and Disdvantages of using artificial neural networks versus logistic regression for predicting medical outcomes," *J Clinical Epidemiology,* vol. 49, pp. 1225-1231, 1996.

[177] P. Bruyndonckx, C. Lemaitre, D. J. van der Laan, M. C. Maas, D. R. Schaart, W. Yongang, Z. Li, M. Krieguer, and S. Tavernier, "Evaluation of machine learning algorithms for localizations of photons in undivided scintillator blocks for PET detectors," *IEEE Transactions on Nuclear Science,* vol. 55, pp. 918-924, 2008.

[178] W. Yongang, D. Junwei, Z. Zhonghui, Y. Yang, Z. Lijun, and P. Bruyndonckx, "FPGA Based Electronics for PET Detector Modules With Neural Network Position Estimators," *IEEE Transactions on Nuclear Science,* vol. 58, pp. 34-42, 2010.

[179] R. M. Gray and A. Macovski, "Maximum a Posteriori Estimation of Position in Scintillation Cameras," *IEEE Transactions on Nuclear Science,* vol. 23, pp. 849-852, 1976.

[180] T. D. Milster, L. A. Selberg, H. H. Barrett, A. L. Landesman, and H. Seacat, "Digital position estimation for the modular scintillation camera," *IEEE Transactions on Nuclear Science,* vol. 32, pp. 748-752, 1985.

[181] N. H. Clinthorne, W. L. Rogers, L. Shao, and K. F. Koral, "A Hybrid Maximum likelihood Position Computer for Scintillation Cameras," *IEEE Transactions on Nuclear Science,* vol. 34, pp. 97-101, 1987.

[182] W. L. Rogers, N. H. Clinthorne, L. Shao, and K. F. Koral, "Experimental evaluation of a modular scintillation camera for SPECT," *IEEE Transactions on Nuclear Science,* vol. 36, pp. 1122-11126, 1989.

[183] X. Liu, N. H. Clinthorne, L. Shao, K. F. Koral, and W. L. Rogers, "Recursive Calculation of the 2-Dimensional Maximum-Likelihood Position Estimate for a Scintillation Camera," *IEEE Transactions on Nuclear Science,* vol. 37, pp. 713-717, Apr 1990.

[184] T. Ling, K. Lee, and R. S. Miyaoka, "Performance comparisons of continuous miniature crystal element (cMiCE) detectors," *IEEE Transactions on Nuclear Science,* vol. 53, pp. 2513-2518, 2006.

[185] D. Gagnon, N. Pouliot, L. Laperriere, M. Therrien, and P. Olivier, "Maximum-Likelihood Positioning in the Scintillation Camera Using Depth of Interaction," *IEEE Transactions on Medical Imaging,* vol. 12, pp. 101-107, Mar 1993.

[186] T. Tomitani, Y. Futami, Y. Iseki, S. Kouda, T. Nishio, T. Murakami, A. Kitagawa, M. Kanazawa, E. Urakabe, M. Shinbo, and T. Kanai, "Depth encoding of point-of-interaction in thick scintillation cameras," in *IEEE Nuclear Science Symposium and Medical Imaging Conference*, 1999, pp. 1182-1186.

[187] S. K. Moore, W. C. J. Hunter, L. Furenlid, and H. H. Barrett, "Maximum-likelihood estimation of 3D event position in monolithic scintil- lation crystals: Experimental results," in *IEEE Nuclear Science Symposium and Medical Imaging Conference*, Honolulu, Hawaii, 2007, pp. 3691-3694.

[188] W. C. J. Hunter, H. H. Barrett, and L. Furenlid, "Calibration method for ML estimation of 3D interaction position in a thick gamma-ray camera," *IEEE Transactions on Nuclear Science,* vol. 56, pp. 189-196, 2009.

[189] S. Krishnamoorthy, S. Stoll, M. Purschke, C. L. Woody, P. O'Connor, D. Schlyer, and P. Vaska, " Investigation of 3D Event Positioning in a PET Detector with Continuous Scintillator and APDs," in *IEEE Nuclear Science Symposium and Medical Imaging Conference* Orlando, FL, 2009.

[190] G. F. Knoll, *Radiation Detection and Measurement*, 3 ed. vol. WIley, 2000.

[191] D. L. Alexoff, P. Vaska, D. Marsteller, T. Gerasimov, J. Li, J. Logan, J. Fowler, N. B. Taintor, P. K. Thanos, and N. D. Volkow, "Reproducibility of 11C-Raclopride binding in the rat brain measured with the MicroPET R4: Effects of scatter correction and tracer specific activity," *Journal of Nuclear Medicine,* vol. 44, pp. 815-822, 2003.

[192] Q. Cao, S. Liu, G. Niu, K. Chen, Y. Yan, Z. Liu, and X. Chen, "Phage display peptide probes for imaging early response to bevacizumab treatment," *Amino Acids,* 2010.

[193] S. Stoll, S. Krishnamoorthy, M. Purschke, C. Woody, D. Schlyer, and P. Vaska, "Exploring the Limits of PET Resolution with a Monolithic Scintillator Detector," in *IEEE Nuclear Science Symposium and Medical Imaging Conference*, Knoxville, TN, 2010, p. (in press).